EXPERIMENTAL SYSTEMS FOR EX-VIVO AND IN-VITRO STUDIES OF BLAST-INDUCED TRAUMATIC BRAIN INJURY

By

Suhas Vidhate

A DISSERTATION

Submitted to
Michigan State University
in partial fulfillment of the requirements
for the degree of

Mechanical Engineering — Doctor of Philosophy

2021

ABSTRACT

EXPERIMENTAL SYSTEMS FOR EX-VIVO AND IN-VITRO STUDIES OF BLAST-INDUCED TRAUMATIC BRAIN INJURY

By

Suhas Vidhate

Blast-induced traumatic brain injury (bTBI) has been widely accepted as a "signature" wound affecting military service members in modern conflicts. When a blast-wave generated by an improvised explosive device explosion propagates through the human head, it is hypothesized to cause direct mechanical damage to the brain tissue leading to vascular injury, cerebral edema as well as less detectable but persistent deficits. However, the exact mechanisms and pathophysiology of bTBI still remain poorly understood. One of the main reasons for such poor understanding is the technical challenge of reproducing the typical time-varying loading cycles induced on brain tissue after a blast event under controlled laboratory conditions. Blast events have a sub-millisecond onset of high pressure followed by complex dynamics resulting from the interaction between the blast wave and the intricate anatomical structure of the human head. This interaction gives rise to time-varying intracranial pressure profiles, dynamic shear loads, and cavitation events, which are hypothesized to cause mechanical insults to the brain tissue.

To tackle these experimental challenges, we have developed four experimental devices that can reproduce the dominant intracranial effects induced by blast loading onto the brain. These experimental devices are: (1) Multi-material Hopkinson bar (MMHB) actuator, (2) Generator of broadband pressure cycles, (3) Rig for controlled-cavitation events, and (4) Generator of dynamic shear cycles. This dissertation details the design and development of the aforementioned experimental systems along with the preliminary ex-vivo and in-vitro

experiments performed to test their applicability.

The designed apparatuses are comparably inexpensive, compact, easily portable, and highly controllable, making them well suited for biomedical applications. These devices can be used to conduct *ex-vivo* and *in-vitro* experiments involving animal brain tissue specimens, cell cultures, and organoids to explore their pathophysiological response to the blast-like loadings observed during a bTBI event.

Dedicated to my beloved au	nt Aruna and my wife Rasika support, and sacrifices	a for their unconditional love,

ACKNOWLEDGMENTS

My academic journey to PhD at Michigan State University (MSU) has been possible only due to the strong support and guidance from many special people at different stages of my life. I want to take this opportunity to express my sincere gratitude to them all.

First and foremost, I want to thank my advisor Prof. Ricardo Mejía-Alvarez for his continuous guidance and support throughout my PhD tenure. Dr. Mejía-Alvarez always encouraged my ideas and gave me the opportunity to work autonomously. He was the first to applaud me for accomplishments, provided constructive criticism when required, and steered me in the right direction during setbacks. His immense knowledge and experience helped bring my ideas into reality and personally motivated me greatly.

I am also deeply grateful to my dissertation committee members Dr. Adam M. Willis (Maj. USAF), Prof. Thomas J. Pence, and Prof. Ranjan Mukherjee for their invaluable supervision and assistance. Their inputs and suggestions always persuaded me to explore beyond the obvious and bring ingenuity to my work.

I want to thank my research collaborators Dr. Joseph Beatty and Dr. Charles Lee Cox from the Department of Physiology at MSU; Dr. Michael March, Dr. Patrick Sleiman, and Dr. Hakon Hakonarson from the Center for Applied Genomics at the Children's Hospital of Philadelphia (CHOP); Prof. Zane Lybrand from the Department of Biology at Texas Woman's University; and Nikolas Merlock from the University of Texas at San Antonio for their association in conducting the multi-disciplinary research. Their collaborations facilitated me to demonstrate the applicability of my doctoral research.

Within MSU, I express my gratitude to Dr. Craig Gunn for all the technical writing guidance and Mechanical Engineering Department Staff for their organizational support.

And I want to thank MSU, U.S. Air Force Research Laboratory (award numbers FA8650-18-2-6880 and FA865-17-2-6836), and the Qatar National Research Fund (a member of the Qatar Foundation, NPRP grant No. 8-2424-1-477) for sponsoring my research.

I have had the special support and encouragement from my colleagues Joseph Kerwin, Atacan Yücesoy, Ankit Gautam, Tushar Kailu, Faezeh Masoomi, Clément Roy, and Paul Sandherr through several technical contributions and wonderful collaborations. I am grateful for the cherished time we spent together in laboratory and socially. I also want to thank my friends Saikat Mondal, Deepak Kumar, Gaurav Chauda, and Dr. Saranraj Karuppuswami for their companionship which turned my PhD journey into a joyful ride.

I particularly want to thank my schoolteachers Mr. Vivek Supare and Mr. Surendranath Reddy for cultivating my special interest in Mathematics and Physics. I also want to thank my professors at the Indian Institute of Technology Bombay, Dr. Salil S. Kulkarni, Dr. Milind Atrey, and Dr. V. Kartik, for giving me the early research exposure and inspiring me to pursue doctoral studies.

Finally, a special thanks to my family. I want to remember my late father Mr. Jeevan Vidhate and my late mother Mrs. Anita Vidhate for all the love and values they deeply enrooted into me. I also want to remember my late grandparents Dr. Laxman Vidhate and Mrs. Kanta Vidhate for their cheers and blessings. I want to thank my uncles Mr. Vasudeo Vidhate and Mr. Gajanan Vidhate, and all of my family whom I owe a great deal. I would not have been here without their support and sacrifices. I want to appreciate my friends Visat Patel and Shubham Yadav for the motivating conversations about business, technology, and research which always kept me enthusiastic about my work. Lastly, I want to thank my dear wife Rasika for her patience, support, and companionship, which helped me to complete this journey with ease.

TABLE OF CONTENTS

LIST (OF TA	BLES	X
LIST (OF FIC	GURES	X
Chapte	er 1	Introduction	1
1.1	Introd	uction and Motivation	1
1.2	Litera	ture Review	7
	1.2.1	Experimental Techniques for Impulsive Pressure Generation	8
	1.2.2	Experimental Techniques for Generating Cavitation	Ĝ
	1.2.3	Experimental Techniques for Dynamic Shear Loadings	10
1.3	Aims	and Outline	11
	1.3.1	Devices for Complex Pressure Loadings	11
	1.3.2	Device to Generate Cavitation	12
	1.3.3	Device for Dynamic Shear Cycles	12
Chapte	er 2	Multi-Material Hopkinson Bar Actuator	13
2.1	Introd	uction	13
2.2	Metho	ds	16
	2.2.1	Stress Wave Propagation in Multi-Material Elastic Bars	17
	2.2.2	Multi-material Hopkinson bar (MMHB) Actuator	20
	2.2.3	Theoretical Background and Numerical Modeling	21
		2.2.3.1 One-dimensional Wave Propagation in Solids	21
		2.2.3.2 Method of Characteristics for Modeling One-dimensional Wave	
		Propagation in a Multi-Material Bar	24
	2.2.4	Optimization Methodology	29
		2.2.4.1 Design Parameters	29
		2.2.4.2 Optimization Algorithm	31
		2.2.4.3 Objective Functions	32
2.3	Result	s	34
	2.3.1	Case Study-I: Single Frequency Sine Wave	34
	2.3.2	Case Study-II: Single-frequency decaying sine wave	36
	2.3.3	Case Study-III: Sum of two sinusoidal waves	38
	2.3.4	Case Study-IV: Sum of three sinusoidal waves	36
	2.3.5	Case Study-V: Sum of three decaying sinusoidal waves	42
2.4	Discus	sion	44
CI.	0		4.5
Chapte		· ·	47
3.1			47
3.2	Design		48
	3.2.1 $3.2.2$	Working Principle	48
	0.4.4	Device Paddication	4:

	3.2.2.1 Design Iteration I
	3.2.2.2 Design Iteration II
	3.2.3 Instrumentation
	3.2.4 Numerical Model
3.3	Control
	3.3.1 System Identification
	3.3.2 Feedforward Control
3.4	Results
	3.4.1 Single Pulse Waveform
	3.4.2 Friedlander Waveform
	3.4.3 Multi-modal Waveform
3.5	Conclusion and Discussion
0.0	Conclusion and Discussion
Chapte	er 4 Bench-top Rig for Controlled-Cavitation Experiments 7
4.1	Introduction
4.2	Design
4.2	4.2.1 Working Principle
	4.2.2 Device Fabrication
4.0	
4.3	Results and Discussion
4.4	Conclusion
Chapte	· · · · · · · · · · · · · · · · · · ·
5.1	Introduction
5.2	Design Iteration I
	5.2.1 Working Principle
	5.2.2 Device Fabrication
	5.2.3 Instrumentation
	5.2.4 Performance Characterization
	5.2.5 Control
	5.2.5.1 System Identification
	5.2.5.2 Feedforward Control
	5.2.6 Limitations
5.3	Design Iteration II
	5.3.1 Working Principle
	5.3.2 Device Fabrication
	5.3.3 Instrumentation and Control
5.4	Results and Discussion
5.5	Conclusion
5.5	
Chapte	er 6 Preliminary Ex-vivo and In-vitro Experiments
Спары 6.1	Ex-vivo Experiments
0.1	6.1.1 Ex-vivo Experiments involving Time-varying Pressure Cycles
	6.1.1.2 Results

	6.1.2	Ex-vivo Experiments involving Dynamic Shear Loadings 12	3
		6.1.2.1 Experimental Procedure	3
		6.1.2.2 Results	6
6.2	In-vitr	vo Experiments	0
	6.2.1	In-vitro Experiments involving HeLa cell cultures	0
		6.2.1.1 Experimental Procedure	0
		6.2.1.2 Results	1
	6.2.2	In-vitro Experiments involving Cerebral Organoids	4
		6.2.2.1 Introduction	4
		6.2.2.2 Experimental Procedure	8
		6.2.2.3 Results	0
Chapte	er 7	Future Directions	3
7.1		e Directions for the MMHB Actuator	
7.2		e Directions for the Pressure Apparatus	
7.3		e Directions for the Cavitation Rig	
7.4		e Directions for the Shear Apparatus	
BIBLI	OGR A	PHY	8

LIST OF TABLES

Table 2.1:	Material library for multi-material bar components. The material properties for Material ID 1-5 were taken from [1], and Material ID 6-12 were obtained from the ANSYS material library [2]	30
Table 2.2:	Design variables for MMHB actuator	30
Table 2.3:	RMSE values and the optimized actuator design parameters for the MMHB optimization case studies	44
Table 3.1:	Material properties for the numerical model of the pressure apparatus $$. $$	56
Table 3.2:	Input parameters of the sine-sweep system identification experiments conducted for the pressure apparatus	60
Table 3.3:	Input excitation pulses constructed for generating pressure pulses	66
Table 3.4:	Sinusoidal components of multi-modal target pressure profile	71
Table 5.1:	Input parameters of the sine-sweep system identification experiments conducted for the shear apparatus (Design iteration I) $\dots \dots \dots$.	97
Table 6.1:	Loading protocols for $in\text{-}vitro$ experiments involving HeLa cell cultures	132

LIST OF FIGURES

Figure 1.1:	Illustration showing a blast wave generated from an explosion and the resulting injuries from the blast exposure (adapted from [3])	2
Figure 1.2:	A Friedlander waveform having a peak pressure of 450 kPa and a positive phase duration of 10 ms	3
Figure 1.3:	Interaction between a blast wave and the human head (axial-view shown). The reflection and the transmission of the incident wave and the resulting skull deformation are also illustrated (adapted from [4])	3
Figure 1.4:	(a) The time-domain and (b) the frequency-domain representation of the intracranial pressure profile at the contrecoup region (shown in figure 1.3) resulting from a blast exposure $[5,6]$	4
Figure 1.5:	Illustration of skull flexure resulting from blast wave-skull interaction (adapted from [7])	6
Figure 1.6:	Experimental setup of a split Hopkinson pressure bar (Picture Credits: REL Inc.)	8
Figure 1.7:	Experimental setup of a shock-tube (Picture Credits: Center for Injury Biomechanics, Materials, and Medicine at New Jersey Institute of Technology)	9
Figure 2.1:	(a) Schematic of the three bar configurations used to illustrate the effect of impedance mismatch. (b) Incident stress pulse (σ_L) specified as the boundary condition at the left end $x=0.$	18
Figure 2.2:	The stress profiles (σ_R) at the fixed far end of (a) single material bar, (b) two-material bar, and (c) three-material bar depicted in figure 2.1a	19
Figure 2.3:	Schematic of the MMHB actuator	20
Figure 2.4:	A spring-dashpot representation of the standard-linear-solid (SLS) material model	22
Figure 2.5:	Stress wave propagation through the interface between materials A and B	22

	Characteristics solution for (a) Left boundary point, (b) Interior point, and (c) Right boundary point of the MMHB actuator. The subscript of the spatial element (x) indicates the location of grid points: 1 and n denote the left and right boundary, respectively, and i denote an internal	Figure 2.6:
25	point	
32	Flowchart of the optimization algorithm	Figure 2.7:
35	(a) Time domain and (b) frequency domain comparison between the target pressure profile and the output pressure profile generated by the optimized MMHB actuator for case study-I	Figure 2.8:
37	(a) Time domain and (b) frequency domain comparison between the target pressure profile and the output pressure profile generated by the optimized MMHB actuator for case study-II	Figure 2.9:
39	2: The set of optimization solutions obtained for the case study-III. These solutions are plotted in the objective space where the axes denote the optimization objective functions	Figure 2.10:
40	: (a) Time domain and (b) frequency domain comparison between the target pressure profile and the output pressure profile generated by the optimized MMHB actuator for case study-III	Figure 2.11:
41	2: (a) Time domain and (b) frequency domain comparison between the target pressure profile and the output pressure profile generated by the optimized MMHB actuator for case study-IV	Figure 2.12:
43	8: (a) Time domain and (b) frequency domain comparison between the target pressure profile and the output pressure profile generated by the optimized MMHB actuator for case study-V	Figure 2.13:
48	A piston-cylinder assembly (l_0 : initial length of the water volume inside the cylinder, u_p : displacement of the piston)	Figure 3.1:
50	(a) Cross-sectional schematic view and (b) Fabricated design of the pressure apparatus (Design iteration I)	Figure 3.2:
51	The complete assembly of the pressure apparatus (Design iteration I) $$	Figure 3.3:
53	(a) Cross-sectional schematic view and (b) Fabricated design of the pressure apparatus (Design iteration II)	Figure 3.4:

Figure 3.5:	(a) Pressure apparatus fixture consisting of aluminum plates and steel threaded rods along with the supporting V-block and (b) the complete assembly of the pressure apparatus (Design iteration II)	54
Figure 3.6:	One-dimensional domain for the numerical model simulating the pressure chamber with white dots showing the locations of the nodes used for extracting pressure profiles	55
Figure 3.7:	Comparison between the actuator displacement profile (left y-axis) specified as the input boundary condition to the numerical model and the output pressure profiles (right y-axis) obtained from the numerical simulation	58
Figure 3.8:	A chirp signal	60
Figure 3.9:	(a) Chirp voltage profile given as an input to the pressure apparatus for a system identification experiment (b) Output pressure profile generated as a response to the chirp excitation	61
Figure 3.10:	(a) Frequency-domain representation of the chirp input profile (b) Frequency-domain representation of the output pressure profile	62
Figure 3.11:	(a) Gain curves and (b) phase difference curves for the pressure apparatus determined from system identification experiments	64
Figure 3.12:	(a) Sinusoidal excitation pulses given as inputs to the apparatus. (b) Output pressure pulses generated by the apparatus for corresponding input pulses	67
Figure 3.13:	Comparison between the pressure pulse generated by our apparatus and the pressure profile obtained from SHPB experiment [8]	68
Figure 3.14:	A Friedlander waveform with 450 kPa maximum pressure and 10 ms positive phase duration	69
Figure 3.15:	Comparison between a Friedlander like input excitation waveform given to the apparatus (left y-axis) and the output pressure profiles (right y-axis) generated by the apparatus	70
Figure 3.16:	Multi-modal target pressure profile constructed for an output tracking problem	71
Figure 3.17:	Control input profile determined by the feedforward controller	72

Figure 3.18:	Comparison between the target pressure profile and the experimental pressure profiles obtained using the feedforward controller	73
Figure 4.1:	A piston-cylinder assembly filled with water (l_0 : initial length of the water volume inside the cylinder, u_p : displacement of the piston)	78
Figure 4.2:	Experimental setup of the cavitation apparatus	79
Figure 4.3:	Comparison between the target piston displacement profile and the measured piston displacement profile for the cavitation experiment (left y-axis). The force applied by the motor to achieve the target piston displacement is also shown (right y-axis)	81
Figure 4.4:	Displacement of the piston (left y-axis) and the resulting pressure profile generated inside the chamber (right y-axis). Some of the key instances of the cavitation event are highlighted on the pressure profile. The corresponding high-speed images of the pressure chamber are shown in figure 4.5	83
Figure 4.5:	High-speed images of the pressure chamber showing the expansion and collapse of the cavitation bubbles. The pressure inside the chamber at the corresponding instances is highlighted on the pressure profile shown in figure 4.4.	84
Figure 5.1:	Schematic of the shear apparatus (Design iteration I)	89
Figure 5.2:	Fabricated setup of the shear apparatus (Design iteration I) $\dots \dots$	90
Figure 5.3:	A PAA gelatin specimen	91
Figure 5.4:	Current profile given as an excitation input to the voice-coil actuator	92
Figure 5.5:	High-speed images showing the shear deformation of PAA gelatin specimen	93
Figure 5.6:	Processed images of the gelatin specimen overlaid with displacement field vectors at time (A) $t=0\mathrm{ms}$, (B) $t=5\mathrm{ms}$, (C) $t=10\mathrm{ms}$, (D) $t=15\mathrm{ms}$, (E) $t=20\mathrm{ms}$, and (F) $t=25\mathrm{ms}$	94
Figure 5.7:	Measured top plate displacement for the first two loading cycles	95
Figure 5.8:	Comparison of the shear strain profiles computed using our in-house developed PIV script, the PIVLab toolbox, and the measured top plate displacement profile	96
Figure 5.9:	Shear strain-rate profile for the first two loading cycles	96

Figure 5.10:	(a) Chirp voltage profile given as an input to the shear apparatus for a system identification experiment. (b) Output displacement profile generated as a response to the chirp excitation	98
Figure 5.11:	(a) Gain curves and (b) phase difference curves for the shear apparatus (Design iteration I) determined from system identification experiments .	100
Figure 5.12:	Multi-modal target displacement profile constructed for an output tracking problem	101
Figure 5.13:	Control input profile determined by the feedforward controller	101
Figure 5.14:	Comparison between the target displacement profile and the experimental displacement profiles obtained using the feedforward controller	102
Figure 5.15:	(a) Front-view and (b) top-view of the fabricated setup of the shear apparatus (Design iteration II)	105
Figure 5.16:	Comparison between the target displacement profiles and the experimental displacement profiles generated by the voice-coil actuator for a loading frequency of (a) 10 Hz, (b) 50 Hz, and (c) 100 Hz	108
Figure 5.17:	Sinusoidal shear strain profiles generated by the shear apparatus (Design iteration II) for a loading frequency of (a) $10\mathrm{Hz}$, (b) $50\mathrm{Hz}$, and (c) $100\mathrm{Hz}$	109
Figure 5.18:	Shear strain (left y-axis) and shear stress (right y-axis) profiles for PAA gelatin shear tests at (a) 20 Hz and (b) 50 Hz loading frequency	111
Figure 5.19:	Variation of the complex shear modulus of PAA gelatin with loading frequency	112
Figure 5.20:	Variation of the loss factor of PAA gelatin with loading frequency	114
Figure 5.21:	Variation of the storage and loss modulus of PAA gelatin with loading frequency	115
Figure 6.1:	Mouse coronal brain slices in aCSF	119
Figure 6.2:	Pressure chamber (Design iteration I) containing the mouse brain slices in an aCSF environment	120
Figure 6.3:	Pressure apparatus (Design iteration I) with the mouse brain slices placed inside the chamber	121
Figure 6.4:	Pressure loading profile exerted onto the mouse brain slices	121

Figure 6.5:	Electrophysiological recordings of the mouse brain slices	122
Figure 6.6:	The shear strain profiles (loading frequency: 50 Hz; shear strain amplitudes: 10% and 20%) exerted onto the brain tissue specimens (the first 10 out of the total 50 loading cycles are shown)	124
Figure 6.7:	High-speed images of the brain tissue specimen under dynamic shear loads: (a) undeformed state (0% shear strain) and (b) deformed state (20% shear strain)	125
Figure 6.8:	Change in electrophysiological resting membrane potential of neurons resulting from dynamic shear loadings of various strain amplitudes	127
Figure 6.9:	Change in electrophysiological input resistance of neurons resulting from dynamic shear loadings of various strain amplitudes	128
Figure 6.10:	Change in electrophysiological time constant of neurons resulting from dynamic shear loadings of various strain amplitudes	128
Figure 6.11:	Frequency of neuronal action potential firing versus current injected curves (F-I curves) for three dynamic shear loading conditions	129
Figure 6.12:	Pressure chamber (Design iteration I) containing a glass coverslip plated with HeLa cells	131
Figure 6.13:	LDH as say results for $\it in\mbox{-} vitro$ experiments involving HeLa cell cultures .	132
Figure 6.14:	"Dead-Green" staining results for <i>in-vitro</i> experiments involving HeLa cell cultures	133
Figure 6.15:	Cerebral organoids reproduce human cortical organization. (A) Timeline for stem cell protocol to grow cerebral organoid. (B) Compared to the human cortex, cerebral organoids contain most of the same layered organization and cells present. (C) Characterization of cortical structure from deep and upper-layer neurons in developing cortical spheroid (dotted line). (D) Image of the ventricular zone (VZ), astrocytes, and oligodendrocytes that form a support niche	136
Figure 6.16:	Neurophysiology of the cerebral organoids. (a) Cerebral organoid displaying a complex network of neurons. (b) Multielectrode array (MEA) measures 12 channels from each organoid. (c) Neural activity is measured from the MEA. The bottom image is a magnified time scale of the voltage signal recorded in the top image. (d) The raw signals can be filtered, and network oscillations are measured to determine the synchrony of activity recorded in cerebral organoids.	137

Figure 6.17:	Blasting cerebral organoids. (a) Timeline of blast experiment (b) Image of 3 cerebral organoids inside of pressure chamber. (c) The pressure waveform recorded inside the chamber during the exposure (Amplitude = 250 kPa, Frequency = 3 kHz, and duration = 8 ms). (d) 24 well plate being loaded with organoids after being blasted. (e) Empty MEA well showing the layout of 12 electrodes. (f) MEA well filled with media and cerebral organoid on electrodes.	139
Figure 6.18:	Blast acutely stimulates cerebral organoids. (a) Raster plot of spike events recorded from MEA in no blast control organoids. (b) Raster plot of spike events recorded from blast group at 1 hr post-blast. (c) Quantification of spike amplitudes in 1 hr and 24 hr post-blast organoids. (d) Quantification of spike number in cerebral organoids	141
Figure 6.19:	Blast acutely increases network synchrony. (A) Two channels with raw signal filtered using a 5 Hz Morlet Wavelet from control organoids. (B) The phase angle difference plotted for each time unit between two channels (black), and the average angle and phase synchronization plotted (green bar) from control organoids. (C) Filtered channels from blast organoids. (D) Plot of phase angle difference (black) and average phase synchronization (green) plotted from blast organoids. (E) Quantification of phase synchronization between the control and blast organoids at 1 hr post-blast. (n=3 organoids per group; p-values less than 0.05 is considered statistically significant)	142

Chapter 1

Introduction

1.1 Introduction and Motivation

Blast-induced traumatic brain injury (bTBI) is one of the major health issues affecting soldiers on the battlefield. It has been a leading cause of mortality and disability sustained by armed forces and law enforcement personnel. The statistics of U.S. military casualties in the operations held in Iraq and Afghanistan reported 253,300 traumatic brain injury cases between 2000 and 2012 [9]. Consequently, this issue has caused a financial burden of billions of dollars to the health care system [10].

As stated in [11–13], traumatic brain injuries associated with blast exposure follow four distinct categories: primary injuries are caused by the interaction of the blast wave directly with the brain tissue leading to mechanical damage; secondary injuries result from projectile (shrapnel) penetration into the head; tertiary injuries are caused by blunt impacts to the head as a result of being propelled away by the explosion; and quaternary injuries include other forms of injury such as polytrauma, thermal, and chemical burns [14,15]. The four injury categories and their causes are illustrated in figure 1.1. Out of all these injuries, primary bTBI is the least understood and thus have been the main focus of this dissertation.

The blast-wave generated from an improvised explosive device (IED) explosion typically follows the characteristics of a Friedlander waveform [16,17]. A Friedlander waveform consists

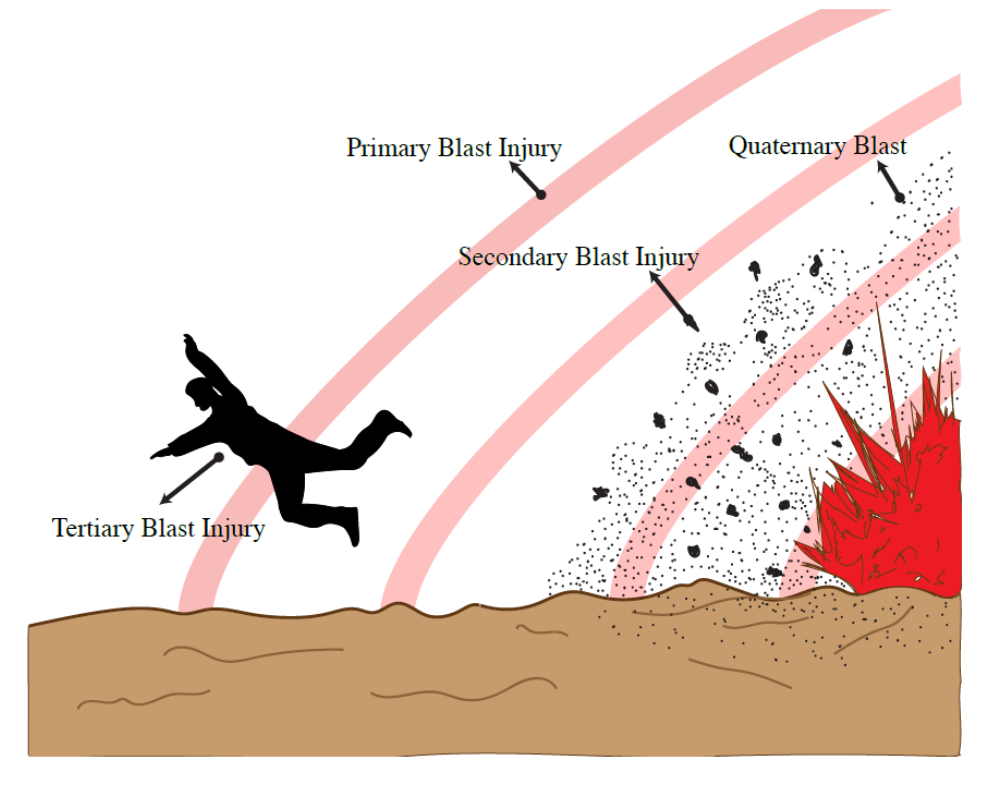


Figure 1.1: Illustration showing a blast wave generated from an explosion and the resulting injuries from the blast exposure (adapted from [3])

of an instantaneous rise in pressure followed by an exponential decay and, lastly, a negative pressure phase [16]. The time duration for which the pressure is above the atmospheric pressure is known as the positive phase duration of the waveform. As an illustration, a Friedlander waveform having a peak pressure of 450 kPa and a positive phase duration of 10 ms is shown in figure 1.2.

When a human is exposed to a blast wave generated from an IED explosion, the blast wave interacts with the skull and the intricate anatomical structure inside the head. One such interaction is illustrated in figure 1.3, where reflection and the transmission of the head-on incident blast wave through the human head (axial-view) is shown. This interaction alters the blast wave's Friedlander wave nature and gives rise to complex and time-varying intracranial pressure (ICP) profiles. The comprehensive numerical studies [5,6] have simulated a

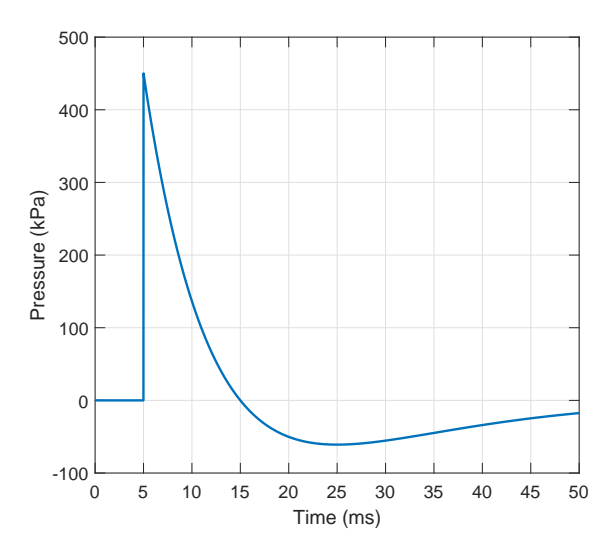


Figure 1.2: A Friedlander waveform having a peak pressure of $450\,\mathrm{kPa}$ and a positive phase duration of $10\,\mathrm{ms}$

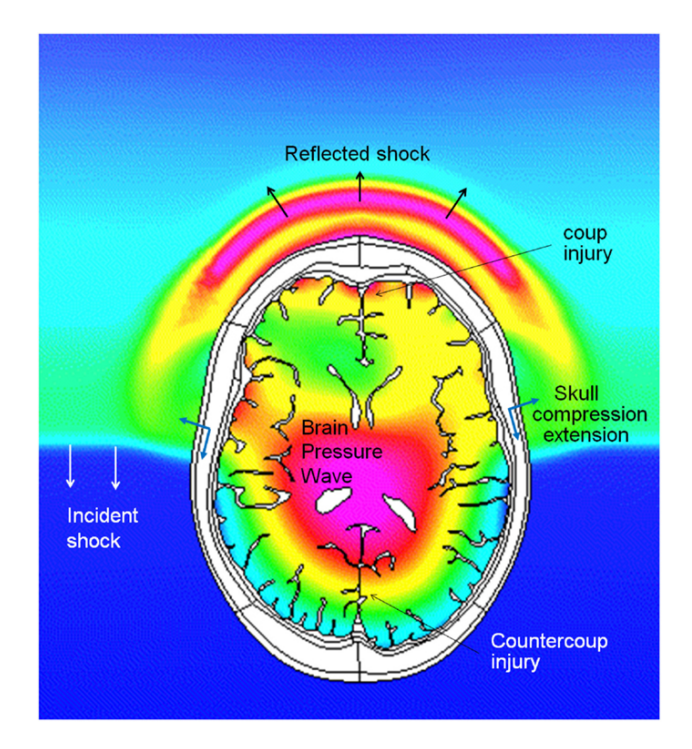


Figure 1.3: Interaction between a blast wave and the human head (axial-view shown). The reflection and the transmission of the incident wave and the resulting skull deformation are also illustrated (adapted from [4]).

blast wave generated by a detonation of 2.3 kg of C4 at a stand-off distance of 2.3 m, and analyzed the mechanical loads experienced by brain tissue due to the blast exposure. These

studies reported that the ICP profiles are complex, highly dynamic, and exhibit spatial variation. One such ICP profile experienced by the brain's rear region (contrecoup region) with respect to the incident head-on blast wave is shown in figure 1.4a. The frequency-domain representation of the same ICP profile is shown in figure 1.4b. This ICP profile has a wide

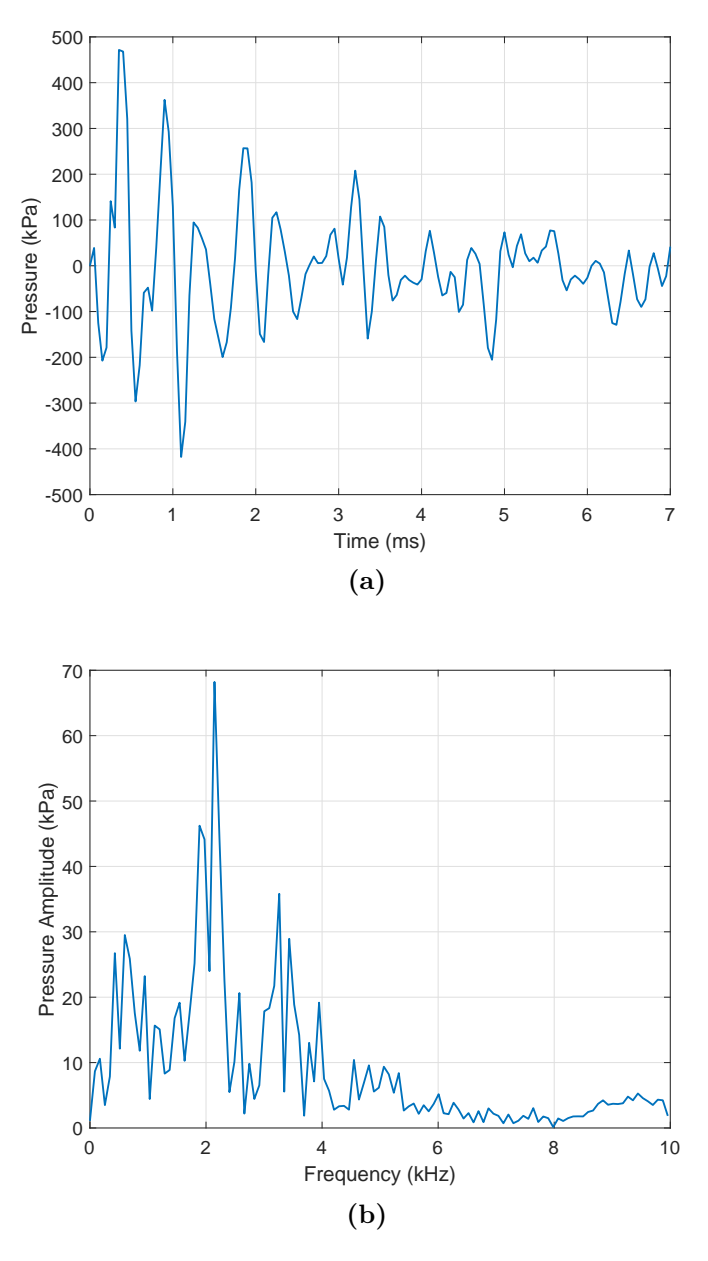


Figure 1.4: (a) The time-domain and (b) the frequency-domain representation of the intracranial pressure profile at the contrecoup region (shown in figure 1.3) resulting from a blast exposure [5,6]

spectral distribution, which contributes to its complex and highly-dynamic nature. It can be observed that most of the power is carried by the frequencies in the $0-5\,\mathrm{kHz}$ range, which has significantly higher amplitudes compared to the frequencies in the $5-10\,\mathrm{kHz}$ range.

The multi-material structure of the head offers interfaces with impedance mismatch for the transmission of the incident blast wave. Because of the impedance mismatch at each material interface, a part of the incident stress wave reflects, and a part of it is transmitted. This transmission and reflection repeat at every intermediate interface and result in a complex ICP profile because of the wave superpositions [7,13]. A blast wave also causes the skull to deform dynamically (shown in figure 1.3), creating localized regions of high and low pressure and large pressure gradients that sweep through the brain [18]. This unsteady deformation of the skull also contributes to the complexity of the ICP profiles [7,18,19].

The blast wave interaction with the skull and the intricate anatomical structure inside the head also results in traveling shear waves. The unsteady deformation of the skull resulting from reflection and transmission of the incident blast wave at the air-skull interface excites the skull's multi-modal response. This skull flexure phenomenon is illustrated in figure 1.5. The skull flexure resulting from a blast exposure additionally contributes to traveling shear waves inside the brain soft tissue [18]. As with the case of longitudinal stress waves, the propagation of shear waves is significantly altered by the impedance mismatch at material interfaces, which results in energy dissipation at the interfacial zones and causes focal mechanical damage [13]. Moreover, the transmission and attenuation of shear waves through the human brain highly depend on the frequency of the propagating shear waves [20].

The negative ICP resulting from the multiple transmissions-reflections of the incident blast wave, skull flexure, or the relative motion between the brain and the skull can cause cavitation in the cerebrospinal fluid (CSF) [7, 13, 21]. Cavitation phenomenon is observed

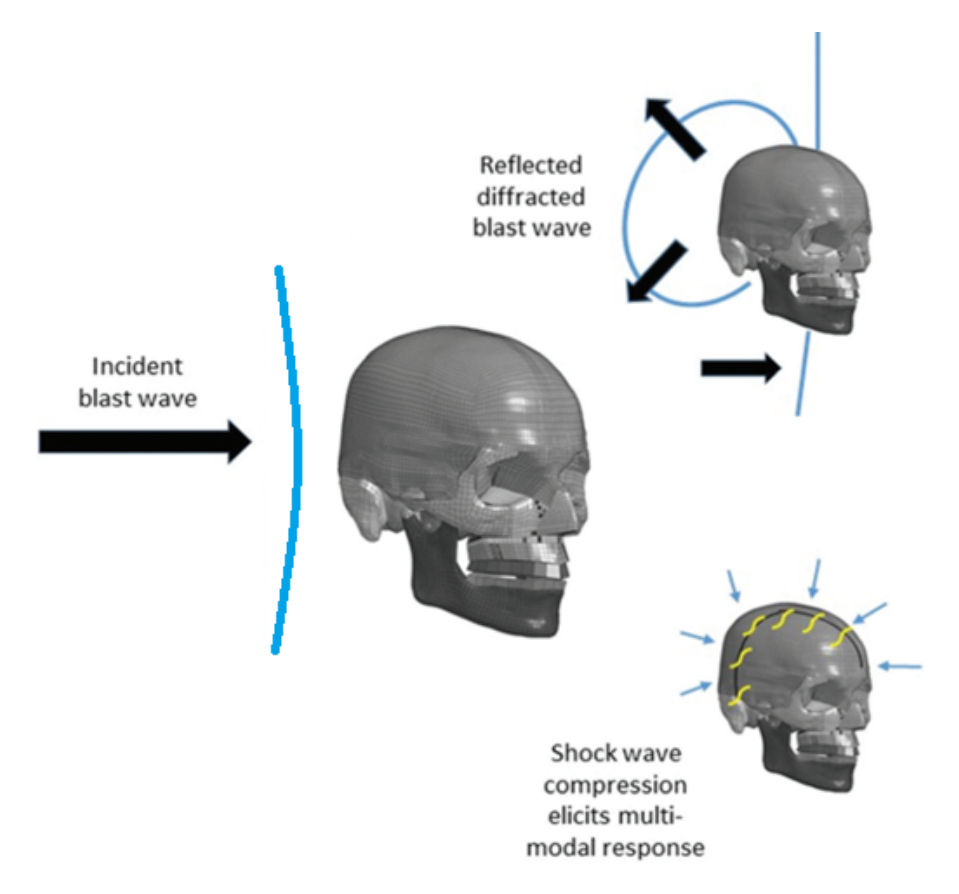


Figure 1.5: Illustration of skull flexure resulting from blast wave-skull interaction (adapted from [7])

when a liquid is subjected to a tensile or negative pressure higher than a threshold, i.e., the liquid's vapor pressure at that temperature [22]. Cavitation encompasses the formation, growth, and collapse of the bubbles caused by the rapid changes in pressure [23]. The collapse of the CSF cavitation bubbles generates high-pressure shock-waves and impinging jets that can be damaging to the surrounding brain tissue [24–27].

Primary blast injuries are hypothesized to be linked with diffuse axonal injury (DAI), vascular tears, intracranial hemorrhage, and focal cortical contusion [28]. The mechanical damage resulting from the negative phase of ICP profiles is often associated with the CSF cavitation [26,29,30]. The local shearing of the brain tissue resulting from pressure waves and shear strain loads at the material interfaces is observed to be consistent with brain injuries

such as DAI near material interfaces [18,28]. Though brain soft-tissue damage resulting from shear [29,31], cavitation [26,29,30], traumatic cell deaths, and disrupted cell structures [8,32] have been identified as possible injury mechanisms involved in bTBI, the exact mechanisms associated with primary blast exposure and their neuropathological consequences still remain ambiguous.

One of the major contributing factors for such ambiguity is the difficulty in replicating the mechanical loads observed during a blast exposure to induce mechanical insults within brain tissue specimens or cell cultures. These mechanical loads include the complex ICP profiles, the dynamic shear loadings induced by traveling shear waves, and the high-pressure shock-waves resulting from the collapse of the CSF cavitation bubbles. To fully understand the underlined pathological effects of these mechanical insults on brain tissue specimens or cell cultures, there is a need for experimental devices that can generate such complex loading cycles under controlled laboratory conditions.

1.2 Literature Review

Although several damage mechanisms associated with bTBI have been reported in the literature [33], this dissertation mainly focuses on three dominant damage mechanisms: (1) impulsive, multi-frequency, and fast-varying pressure cycles, (2) cavitation and,(3) dynamic shear loadings. This section discusses the experimental techniques that have been previously employed to generate above mentioned mechanical loadings.

1.2.1 Experimental Techniques for Impulsive Pressure Generation

Previously, researchers have implemented experimental techniques such as split-Hopkinson pressure bars (SHPB) [8,32,34,35], shock-tubes [36–42], and blast-tubes [43–46] to generate pressure profiles mimicking a blast loading. In the SHPB technique, a traveling stress wave is generated in the incident bar from a striker impact. This wave is then used to compress water and generate impulsive pressures in the piston-cylinder assembly placed at the end of the bar. Shock-tubes use a sudden release of compressed gases to generate impulsive pressures. Furthermore, blast-tubes use confined explosive detonations to generate impulsive pressures. These experimental setups generate pressure profiles that have a single overpressure pulse either sustained or similar to a Friedlander waveform. Other researchers have used microdetonics to generate blast loading [47,48]. Representative experimental setups for an SHPB and a shock-tube are shown in figures 1.6 and 1.7.

All of the above-mentioned techniques have limited control over the pressure profiles that they can generate, are not easily tunable to replicate the ICP dynamics, and are, in general, very expensive, requiring significant technical expertise and large laboratory spaces.



Figure 1.6: Experimental setup of a split Hopkinson pressure bar (Picture Credits: REL Inc.)



Figure 1.7: Experimental setup of a shock-tube (Picture Credits: Center for Injury Biomechanics, Materials, and Medicine at New Jersey Institute of Technology)

1.2.2 Experimental Techniques for Generating Cavitation

There are several experimental techniques reported in the literature employed to generate cavitation events. Some of the key techniques are a modified SHPB [25, 26, 30, 32, 49, 50], shock-tube [36, 37], drop tower [51, 52], ultrasound [53, 54], laser [27, 55], and a laser-ultrasound combination [56]. The modified SHPB setups use the reflected stress-pulse to generate negative pressures and induce cavitation. The shock-tubes and drop towers deliver acceleration-induced or inertial cavitation. The impact from a shock-wave or a drop weight creates a relative motion between the liquid and its surrounding solid boundary, which generates a negative pressure region at the boundary and induces cavitation. The SHPB, shock-tube, and drop tower setups are relatively complex and require rigorous technical training for safe operation. Also, they are extremely bulky and thus, lack portability. The ultrasound technique uses focused ultrahigh-frequency (typically greater than 1 MHz) acoustic waves to apply periodic compression-tension cycles. When the acoustic wave amplitude is sufficiently high, it generates cavitation bubbles during the negative phase. These bubbles partially collapse during the subsequent positive phase of the acoustic wave.

laser-based setups use a focused laser beam pulses to generate cavitation bubbles. The ultrasound and the laser techniques generate focused cavitation events with extremely short timescales (order of few microseconds). The timescales and the frequency range of cavitation events generated by laser and ultrasound techniques significantly differ from the cavitation associated with bTBI, which typically lasts for several milliseconds.

1.2.3 Experimental Techniques for Dynamic Shear Loadings

To induce dynamic shear loading at high strain-rates, researchers have implemented a modified SHPB that includes a parallel plate fixture to shear the specimen [57,58]. However, the shear strain magnitudes generated using the modified SHPB technique are usually very high and result in specimen tearing. This high strain deformation does not replicate the low shear strains observed during a primary bTBI event. The shear deformation linked to bTBI has low strain amplitudes but high strain-rates [10]. Moreover, the SHPB technique cannot generate oscillatory shear deformation associated with traveling shear waves. Rotational rheometers are generally used to induce oscillatory shear deformation into a specimen and can be used to generate shear cycles of low strain amplitudes [59]. However, they are optimized for material characterization tasks and cannot be tuned to generate user-specified shear loading profiles. Additionally, rheometers lack the ability to generate shear deformations at high oscillating frequencies and strain-rates and are, in general, very expensive. Researchers have also developed their own custom shear instruments that use linear actuators and a parallel plate assembly to load soft tissue-like gelatin specimens [60–63]. These reported instruments could generate either the shear strain amplitudes or loading frequencies typically associated with a bTBI event, but not both simultaneously.

1.3 Aims and Outline

An ideal solution to the experimental challenges involved in reproducing mechanical loads of a blast event in a controlled manner would be the following: create completely controllable, portable, reproducible, and inexpensive methods to generate arbitrarily complex pressure cycles, dynamic shear loadings, and cavitation events onto living tissue and cell cultures. Building apparatuses that could be easily shared between laboratories would also accelerate bTBI research. Our research demonstrates the design and development of such experimental devices that can generate tunable, reproducible, and complicated loading cycles.

1.3.1 Devices for Complex Pressure Loadings

In this dissertation, Chapter 2 discusses the concept of a Multi-Material Hopkinson bar (MMHB) actuator to generate complicated stress-wave patterns. The MMHB actuator replaces the incident bar of a conventional split-Hopkinson pressure bar apparatus with a multi-material incident bar to transform the incident stress pulse into a complex loading profile. As proof of concept, we have designed the MMHB actuator for generating various sinusoidal pressure profiles with multi-frequencies and decaying characteristics.

Chapter 3 discusses the design and development of the apparatus for generating broadband pressure cycles. This apparatus uses a water-filled piston-cylinder assembly driven by a piezoelectric actuator to generate complex and fast-varying pressure profiles. The apparatus also incorporates a feedforward controller to track user-specified target pressure profiles. The experimental capabilities of this apparatus are demonstrated by generating a single pressure pulse with various pulse-widths and magnitudes, an approximate Friedlander waveform, and a multi-modal waveform.

1.3.2 Device to Generate Cavitation

Chapter 4 focuses on a bench-top rig designed for controlled-cavitation experiments. This cavitation apparatus also uses a water-filled piston-cylinder assembly, which is operated by a high-speed linear motor to generate negative pressures and induce cavitation. The capabilities of this apparatus are demonstrated by performing a cavitation experiment with water as the working liquid.

1.3.3 Device for Dynamic Shear Cycles

Chapter 5 discusses the design and development of the apparatus for generating dynamic shear cycles. This apparatus uses a voice-coil actuator and two parallel plates assembly to generate oscillatory shear loadings at various strain amplitudes and frequencies. The preliminary experiments conducted to determine the mechanical properties of polyacrylamide (PAA) gelatin specimens, as well as to test the implementation of the apparatus for loading samples of living tissue and three-dimensional cell cultures, are also discussed in this chapter.

Chapter 6 discusses the preliminary ex-vivo and in-vitro experiments conducted to explore the response of biological specimens to complex time-varying pressure and shear loadings. These experiments served a dual purpose: determining the pathophysiological response of the animal brain tissue specimens, cell cultures, and cerebral organoids to the blast-like intracranial effects and testing the implementation of our experimental devices for bTBI-related studies. Lastly, Chapter 7 summarizes the development of the aforementioned experimental systems for loading biological specimens and provides directions for future developments.

Chapter 2

Multi-Material Hopkinson Bar

Actuator

2.1 Introduction

In stress wave analysis and experimental characterization, the assumption of homogeneity and continuity is mostly inadequate for contemporary engineering practices. Specifically, there is a need to better understand the formation of complex wave profiles and the response of the continua to these wave profiles. Conventional testing systems are not fully capable of generating controlled complex stress waves with predefined spectral characteristics comparable to the application requirements.

Systems containing multiple materials and material interfaces typically exhibit complex stress waveforms when subject to impact or blast-like impulsive loads. Structures made up of layered composite materials are examples of this class of systems. The multiple transmissions and reflections that the incident wave experiences because of the layered configuration result in a complicated loading [64], and this phenomenon is utilized to design impact-resistant protective equipment such as armors and helmets [65].

The response of biological systems to exogenous dynamic loadings is another phenomenon where complex stress waveforms are observed. One such case is that of blast-induced Traumatic Brain Injury (bTBI), which is one of the major reasons for the morbidity and mortality of service-members on the battlefield [9,66]. While the nature of the incident load has a significant effect on the magnitude and pattern of injury [67], previous studies show that the multi-layered morphology of the head, skull, and intracranial contents, with different impedances for wave propagation, greatly affect the peak amplitude and the spectral characteristic of the intracranial pressure (ICP) profile [7, 18, 68]. Moreover, not only the peak stress amplitude but also the temporal frequency of the stress profile could contribute to tissue damage [68]. Due to the geometrical and material anisotropy in the brain tissues at the micron-level, central nervous system (CNS) components such as neuron and glial structures might produce different responses to the same blast exposure [69, 70]. As a result, bTBI is diffused in nature due to the heterogeneity of the skull's contents and the complexity of intracranial wave interactions. In consequence, the degree to which different spectral components participate in brain damage is still an open question. There is also a discrepancy in blast exposure data obtained from different laboratories because of the variations in the experimental techniques and protocols implemented to simulate blast [71]. This poses a challenge while comparing bTBI-related experimental studies from different research groups and encourages an experimental technique that can consistently replicate the amplitude and frequency characteristics of stress experienced in human bTBI. Such an experimental technique might replicate blast-like loading conditions that produce TBI neuropathologies seen in post-trauma.

The split-Hopkinson pressure bars (SHPB) technique has been extensively used to investigate the mechanical response of materials at high strain-rate deformation [34,72]. The details of the SHPB technique are well-known. SHPB offers a diverse arrangement of specimen, bar, and loading mechanism for various high strain-rate material characterization

studies. Additionally, the SHPB has been previously used to load biological tissues with blast-like pressure profiles [8,32]. However, the conventional SHPB is still challenging to use on specimens with low strength, stiffness, or impedance, such as biological tissues, foams, gels, and polymers [72–74]. Another limitation is that the loading profile generated using a conventional SHPB is typically a single stress wave pulse [34], despite the various available types of accelerators, e.g., electrostatic, pneumatic, explosive, and pulsed laser [75]. The impact of the striker generates a stress wave that propagates through the incident bar; part of the incident stress pulse is transmitted into the specimen and the transmission bar, while the remaining part reflects into the incident bar. The reflected pulse travels back and forth along the incident bar as it reflects consecutively on both ends of the bar. But this effect does not load the sample cyclically in a typical SHPB test, because the sample and transmission bar tend to separate from the incident bar upon the first wave interaction. Thus, a conventional SHPB is not capable of generating a complex, broadband stress wave akin to ICP profiles.

In this chapter, we report on a promising methodology to design an actuator that can generate repeatable cycles of multi-frequency stress waves at strain-rate levels typical of SH-PBs. Because the loading generated by a conventional SHPB is a single-frequency stress-wave pulse, we consider the more general concept of a Multi-Material Hopkinson Bar (MMHB) actuator. Our contention is that such a device is capable of generating loading profiles having complicated spectral characteristics as per the user specifications. In this concept, the incident bar is substituted for multiple bars of different materials arranged in series. The distribution of materials and lengths of these bars are chosen so as to obtain the characteristics of the targeted loading profile. The underlying idea behind the multi-material incident bar is to transform the single stress wave impact into a targeted complex wave by leveraging

the impedance mismatch between adjacent bars. As the incident wave propagates through the multi-material bar, each material interface produces a reflected and a transmitted wave. This process repeats multiple times at each material interface, inducing wave interactions that result in a more complex output at the end of the multi-material bar. The material and geometrical features of each bar component constituting the multi-material form the parameter design space and require a selection that is based on the targeted profile. A multi-objective optimization algorithm is employed to acquire the multi-material incident bar configuration that can best replicate the targeted wave profile in both the frequency and time domains. This design optimization is achieved by coupling the numerical modeling of the MMHB wave dynamics to the optimization algorithm.

This chapter is organized as follows. Section 2.2 discusses the working principle of the MMHB actuator along with a numerical model analyzing stress wave propagation in multimaterial bars. The optimization algorithm and the design parameters required to develop a target profile-specific actuator are also discussed here. The results from a series of case studies conducted to test the applicability of the MMHB concept are presented in section 2.3. The chapter concludes in section 2.4 with a discussion on the capabilities and limitations of the MMHB actuator.

2.2 Methods

The stress wave propagation through an interface results in a reflected and a transmitted wave due to the impedance mismatch, as detailed in section 2.2.3.1. A multi-material bar constructed by joining multiple bars of different materials naturally has interfaces with impedance mismatch, which create reflections and transmissions of the incident stress wave. The superposition and interference of these wave reflections and transmissions transform a single localized stress pulse input into a relatively complex and delocalized stress wave at the end of the bar.

2.2.1 Stress Wave Propagation in Multi-Material Elastic Bars

The principle of generating complex stress waves using a multi-material bar is demonstrated by analyzing longitudinal stress wave propagation for the three cases shown in figure 2.1a. These cases are: (1) a single material bar made from aluminum, (2) a two-material bar made from aluminum and steel, and (3) a three-material bar made from aluminum, steel, and copper.

The resulting stress history at the end of the multi-material bar is obtained by solving the governing equations given in section 2.2.3.1. These equations within each bar, along with the appropriate interface equations between constituent bars, are treated numerically with MATLAB using the method of characteristics (see section 2.2.3.2). The material properties used for the numerical modeling presented here are listed in table 2.1.

A stress profile (σ_{L}) , such that shown in figure 2.1b, is specified on the left end of the multi-bar assembly as a boundary condition to simulate an impact from a striker. This type of incident stress pulse is typically observed during an impact from a spherical striker [30]. The velocity at the right end of the multi-bar assembly (V_{R}) is specified as zero to impose the fixed-end boundary condition. As a sign convention, compressive stress is considered positive.

The stress profiles (σ_R) generated at the fixed right-end of the multi-bar assembly is extracted as output from the MATLAB script. For the case studies depicted in figure 2.1a, the corresponding computed right-end stress profiles are shown in figures 2.2a, 2.2b, and

2.2c. As the number of bar components within the multi-material bar increases, so does the number of interfaces with impedance mismatch giving rise to an increasing reflection

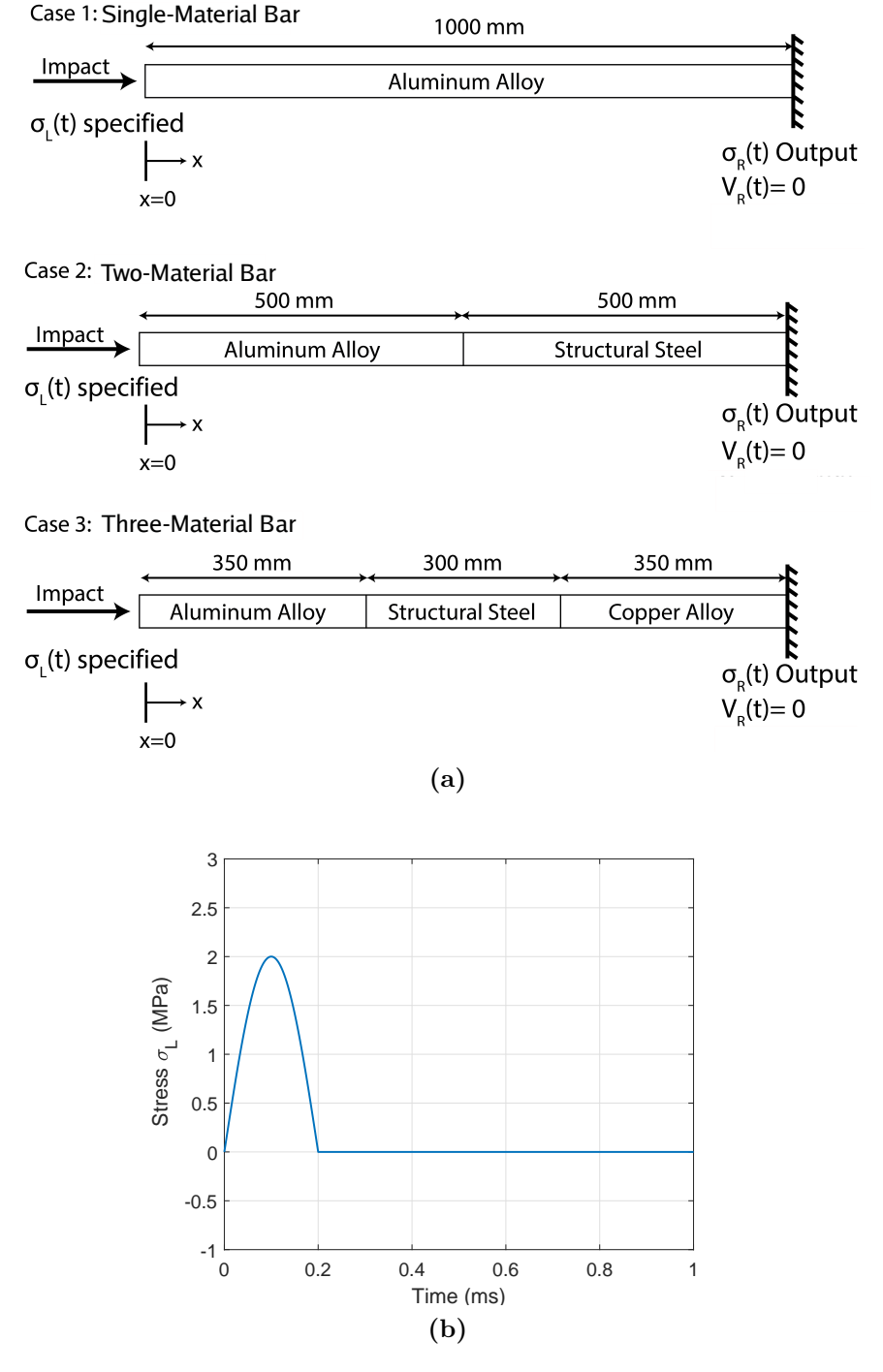


Figure 2.1: (a) Schematic of the three bar configurations used to illustrate the effect of impedance mismatch. (b) Incident stress pulse $(\sigma_{\rm L})$ specified as the boundary condition at the left end x=0.

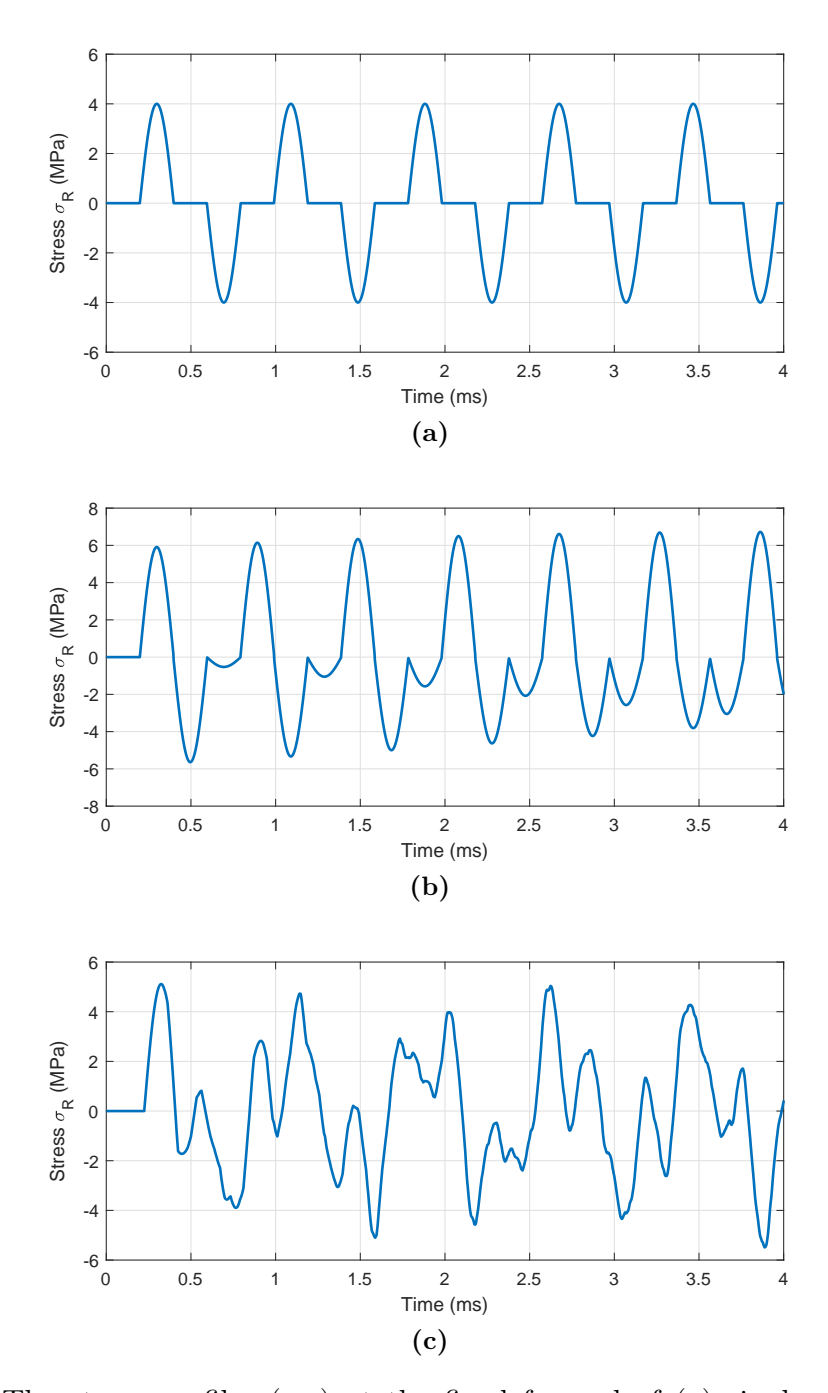


Figure 2.2: The stress profiles (σ_R) at the fixed far end of (a) single material bar, (b) two-material bar, and (c) three-material bar depicted in figure 2.1a

and transmission cascade. Accordingly, the stress profile obtained at the right end of the bar also increases in complexity (as is evident from figures 2.2a, 2.2b, and 2.2c). The case studies depicted in figure 2.1a treated the metallic bar materials as purely elastic. The more

general methodology presented here treats multi-material bars consisting of both elastic and viscoelastic materials, the latter of which allows explicitly for dissipation.

2.2.2 Multi-material Hopkinson bar (MMHB) Actuator

Motivated by the previous considerations, we seek to replicate a given complex loading cycle at the right end of the multi-material bar by optimally sequencing bars of different materials and lengths. Because our primary motivation is the study of bTBI, we focus on an experimental setup that is appropriate for applying loads on biological samples. More generally, however, the principles are general ones that can be applied for broader purposes of material characterization.

The multi-material incident bar shown in figure 2.3 acts as the piston in a piston-cylinder assembly used for unsteady compression of water. Its movement produces a highly complex pressure cycle inside the cylinder. This system is basically a pressure chamber for loading a biological specimen. Water is used as the working fluid inside the pressure chamber due to its nearly incompressible nature.

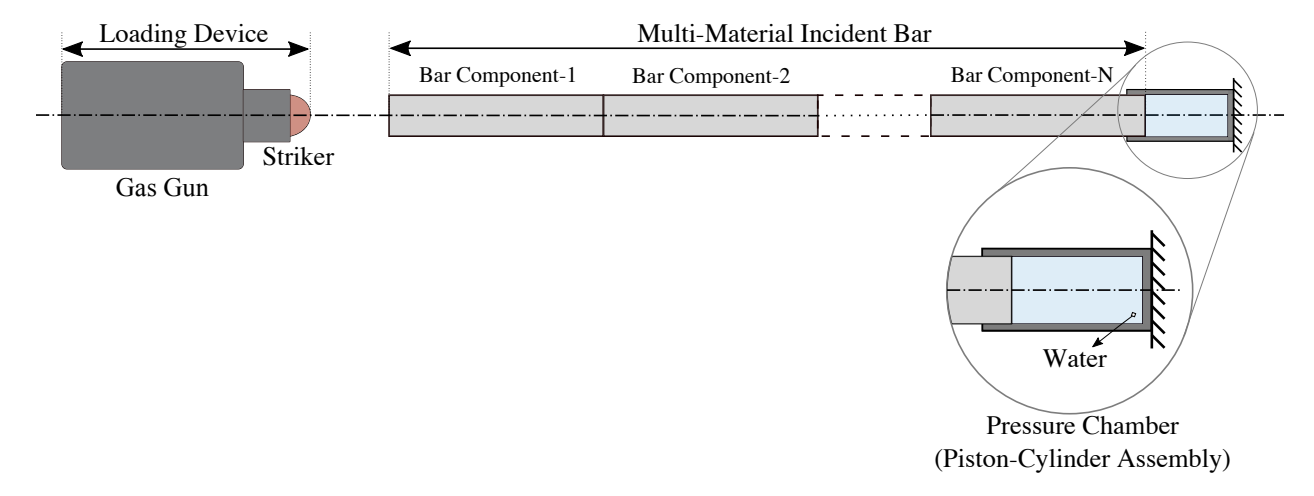


Figure 2.3: Schematic of the MMHB actuator

The actuator design problem involves several design variables such as the lengths of the various bar components, material selection for those components, and the striker impact parameters. The design is now optimized in order to generate a pressure profile similar to the user-specified target pressure profile.

2.2.3 Theoretical Background and Numerical Modeling

2.2.3.1 One-dimensional Wave Propagation in Solids

This section provides a brief review of the essential theoretical background in order to aid in the understanding of the following sections.

One-dimensional longitudinal wave propagation in a long bar is governed by the momentum balance equation

$$\rho \frac{\partial V}{\partial t} = \frac{\partial \sigma}{\partial x},\tag{2.1}$$

and the continuity equation

$$\frac{\partial V}{\partial x} = \frac{\partial \epsilon}{\partial t}.\tag{2.2}$$

The dependent variables, V, σ , and ϵ denote the velocity, stress, and strain respectively at a given location x and time t. The constant ρ denotes the density of the bar material. Additionally, the relation between the stress and the strain is defined by the constitutive model of the bar material, which is taken to be viscoelastic.

Wave propagation in a viscoelastic bar has two distinct characteristics: attenuation and dispersion [1,76]. Attenuation corresponds to the reduction in stress wave amplitude as the wave travels along the length of the bar. Dispersion is associated with the change in either the shape or the spectral character of the stress pulse as it propagates. Here, the standard-

linear-solid (SLS) model is used as the constitutive model. It is modeled as a combination of springs and a dashpot, as shown in figure 2.4.

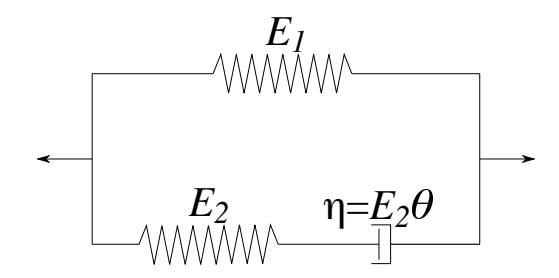


Figure 2.4: A spring-dashpot representation of the standard-linear-solid (SLS) material model

The stress-strain relationship for the SLS model is given by

$$\frac{\partial \sigma}{\partial t} + \frac{\sigma}{\theta} = (E_1 + E_2) \frac{\partial \epsilon}{\partial t} + E_1 \frac{\epsilon}{\theta}, \tag{2.3}$$

where E_1 is the long-term (fully relaxed) modulus, $E_1 + E_2$ is the short-term (instantaneous) modulus, and θ is the relaxation time constant [1,77]. The linear elastic model is the special case of the SLS model with $E_1 = E$ and $E_2 = 0$, where E is the Young's modulus of the elastic bar material.

The wave propagation phenomenon through an interface between two bars made up of materials A and B is shown in figure 2.5. When a stress wave ($\sigma_{\rm I}$) traveling through material A reaches the interface where the two bars are bonded, the difference in the material properties on either side of the interface creates an impedance mismatch for the wave propagation.

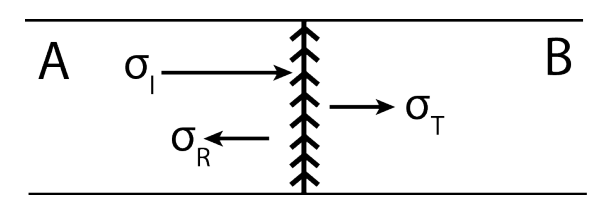


Figure 2.5: Stress wave propagation through the interface between materials A and B

Since the two bars are bonded together, it is assumed that there is no relative motion between the bars at the interface, implying continuous velocity and stress fields across the interface. Part of the incident wave is reflected (σ_R) , while the rest of the wave is transmitted into the next bar (σ_T) .

If both materials A and B are elastic then the amplitudes of the reflected (σ_R) and transmitted (σ_T) stress waves are determined as

$$\sigma_{\rm R} = \frac{Z_{\rm B} - Z_{\rm A}}{Z_{\rm B} + Z_{\rm A}} \sigma_{\rm I} \quad {\rm and} \quad \sigma_{\rm T} = \frac{2Z_{\rm B}}{Z_{\rm B} + Z_{\rm A}} \sigma_{\rm I},$$

where $Z_{\rm A}$ and $Z_{\rm B}$ denote the respective acoustic impedances of materials A and B [78–80]. This acoustic impedance is given by

$$Z = \sqrt{E \times \rho}.$$

As expected, perfect impedance match ($Z_{\rm B}=Z_{\rm A}$) gives no reflected wave and gives a transmitted wave that exactly matches the incident wave. More generally ($Z_{\rm B}\neq Z_{\rm A}$) the transmitted wave has the same compressive or tensile character as the incident wave whereas the reflected wave can change its character depending on the sign of $Z_{\rm B}-Z_{\rm A}$.

The numerical method described next in section 2.2.3.2 provides a treatment where material interfaces are always nodes in the (x,t) discretization. The procedure naturally recovers the above interface relations, if both materials are elastic. When one or both materials are truly viscoelastic then the numerical method provides an appropriate extension.

2.2.3.2 Method of Characteristics for Modeling One-dimensional Wave Propagation in a Multi-Material Bar

Since an elastic material model can be treated as a special case of the SLS model, a numerical model is developed to simulate the wave interaction in a multi-material bar made up of viscoelastic bar components. The governing equations for one-dimensional wave propagation in a viscoelastic bar are treated using the method of characteristics as described in [1].

In an (x, t) domain governed by equations (2.1), (2.2), and (2.3), there are two sets of characteristic curves

$$\frac{\mathrm{d}x}{\mathrm{d}t} = \pm \sqrt{\frac{E_1 + E_2}{\rho}} \equiv \pm C_V, \tag{2.4}$$

where C_V denotes the maximum (leading edge) signal speed in the viscoelastic material. The (+) sign in equation (2.4) corresponds to the waves propagating in the positive x-direction while the (-) sign corresponds to the waves propagating in the negative x-direction. The corresponding compatibility conditions along the characteristics are given by

$$dV = \pm \frac{1}{\rho C_V} d\sigma \pm \frac{\sigma - E_1 \epsilon}{\rho C_V \theta} dt.$$
 (2.5)

The third set of characteristics is non-propagating and along it the compatibility condition holds:

$$dx = 0$$
, and $d\epsilon = \frac{d\sigma}{E_1 + E_2} + \frac{\sigma - E_1 \epsilon}{(E_1 + E_2)\theta} dt$. (2.6)

Quantities E_1 , E_2 , ρ , θ , and C_V depends on location x as determined by the multi-material bar under consideration.

To solve the compatibility equations along the characteristics, the spatial domain for each

of the bar components is discretized to have

$$\Delta x = C_V \times \Delta t, \tag{2.7}$$

where Δx denotes the distance between two adjacent nodes, and Δt denotes the time-step. Additionally, the length of each of the bar components constituting the multi-material bar is rounded so that there is an integer number of node points for each bar component, and the interfaces occur only at the locations of the nodes.

Since the water in the piston-cylinder assembly is modeled as a linear elastic fluid, which can again be considered a special case of the SLS model, it is numerically treated in the same way as the rest of the bar components.

The compatibility equations are implemented along the characteristics to determine velocity (V), stress (σ) , and strain (ϵ) fields for a given initial and boundary conditions. The nodal points are divided into three categories: left boundary point (figure 2.6a), interior points (figure 2.6b), and right boundary point (figure 2.6c).

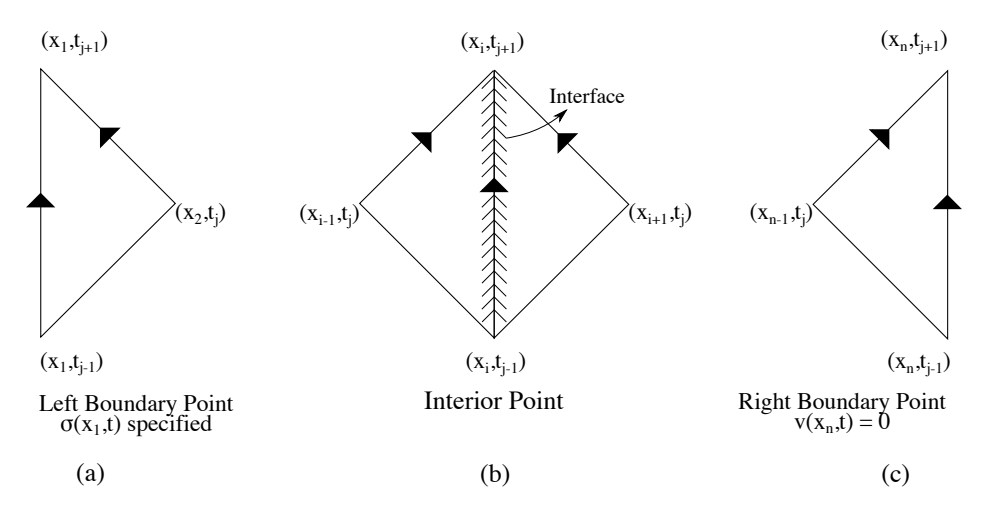


Figure 2.6: Characteristics solution for (a) Left boundary point, (b) Interior point, and (c) Right boundary point of the MMHB actuator. The subscript of the spatial element (x) indicates the location of grid points: 1 and n denote the left and right boundary, respectively, and i denote an internal point.

For the i^{th} interior node point, define $\rho^+(i)$, $E_1^+(i)$, $E_2^+(i)$, $\theta^+(i)$, and $C_V^+(i)$ to be the corresponding material properties of the material just right of the nodal point. Similarly, define $\rho^-(i)$, $E_1^-(i)$, $E_2^-(i)$, $\theta^-(i)$, and $C_V^-(i)$ to be the corresponding material properties of the material just left of the nodal point. Notice that:

$$\rho^{-}(i) = \rho^{+}(i-1),$$

$$E_{1}^{-}(i) = E_{1}^{+}(i-1),$$

$$E_{2}^{-}(i) = E_{2}^{+}(i-1),$$

$$\theta^{-}(i) = \theta^{+}(i-1),$$

$$C_{V}^{-}(i) = C_{V}^{+}(i-1).$$

For the left boundary point (i=1), only ρ^+ , E_1^+ , E_2^+ , θ^+ , and C_V^+ are defined, whereas only ρ^- , E_1^- , E_2^- , θ^- , and C_V^- are defined for the right boundary point (i=n). Because of the way material properties are assigned to the nodal points, in principle, every interior nodal point can be treated as an interface. This observation, utilized by [81] in the analysis of stress waves within an elastic multi-material domain, is central to our treatment of the more general viscoelastic case. In particular, it recovers the impedance conditions of section 2.2.3.1 for the elastic special case.

For the multi-material bar, the intermediate material interfaces between the bar components are treated as bonded interfaces implying no relative motion between the bar components. This makes the velocity and stress fields continuous across the interfaces. However, the strain is generally discontinuous across the interfaces, and we define ϵ^- and ϵ^+ as the strain just to the left and just to the right of the node, respectively.

The velocities and the stresses are determined at the interior points by applying the

compatibility conditions given in equation (2.5) along the characteristics given in equation (2.4). These left-running and right-running characteristics are shown in figure 2.6b. This gives:

$$V(x_{i},t_{j+1}) = \frac{\rho^{-}(i)C_{V}^{-}(i)V(x_{i-1},t_{j}) + \rho^{+}(i)C_{V}^{+}(i)V(x_{i+1},t_{j}) + \sigma(x_{i+1},t_{j}) - \sigma(x_{i-1},t_{j})}{\rho^{-}(i)C_{V}^{-}(i) + \rho^{+}(i)C_{V}^{+}(i)} + \frac{\Delta t}{\rho^{-}(i)C_{V}^{-}(i) + \rho^{+}(i)C_{V}^{+}(i)} \left\{ \frac{E_{1}^{-}(i+1)\epsilon^{-}(x_{i+1},t_{j}) - \sigma(x_{i+1},t_{j})}{\theta^{-}(i+1)} - \frac{E_{1}^{+}(i-1)\epsilon^{+}(x_{i-1},t_{j}) - \sigma(x_{i-1},t_{j})}{\theta^{+}(i-1)} \right\}$$

$$\sigma(x_{i},t_{j+1}) = \frac{\rho^{+}(i)C_{V}^{+}(i)V(x_{i+1},t_{j}) - \rho^{-}(i)C_{V}^{-}(i)V(x_{i-1},t_{j})}{2} - \frac{\{\rho^{+}(i)C_{V}^{+}(i) - \rho^{-}(i)C_{V}^{-}(i)\}V(x_{i},t_{j+1})}{2} + \frac{\sigma(x_{i+1},t_{j}) + \sigma(x_{i-1},t_{j})}{2} + \frac{\Delta t}{2} \left\{ \frac{E_{1}^{-}(i+1)\epsilon^{-}(x_{i+1},t_{j}) - \sigma(x_{i+1},t_{j})}{\theta^{-}(i+1)} + \frac{E_{1}^{+}(i-1)\epsilon^{+}(x_{i-1},t_{j}) - \sigma(x_{i-1},t_{j})}{\theta^{+}(i-1)} \right\}$$

$$(2.9)$$

If the interior point is not at an interface, the equations (2.8) and (2.9) reduce to the corresponding ones given in [1].

The strains at the interior points are determined by applying the compatibility conditions along the characteristics given in equation (2.6). This gives:

$$\epsilon^{+}(x_{i}, t_{j+1}) = \epsilon^{+}(x_{i}, t_{j-1}) + \frac{\sigma(x_{i}, t_{j+1}) - \sigma(x_{i}, t_{j-1})}{E_{1}^{+}(i) + E_{2}^{+}(i)} - \frac{2\Delta t}{E_{1}^{+}(i) + E_{2}^{+}(i)} \left\{ \frac{E_{1}^{+}(i)\epsilon^{+}(x_{i}, t_{j-1}) - \sigma(x_{i}, t_{j-1})}{\theta^{+}(i)} \right\}$$
(2.10)

$$\epsilon^{-}(x_{i}, t_{j+1}) = \epsilon^{-}(x_{i}, t_{j-1}) + \frac{\sigma(x_{i}, t_{j+1}) - \sigma(x_{i}, t_{j-1})}{E_{1}^{-}(i) + E_{2}^{-}(i)} - \frac{2\Delta t}{E_{1}^{-}(i) + E_{2}^{-}(i)} \left\{ \frac{E_{1}^{-}(i)\epsilon^{-}(x_{i}, t_{j-1}) - \sigma(x_{i}, t_{j-1})}{\theta^{-}(i)} \right\}$$
(2.11)

If the interior point is not at an interface, it has $\epsilon^+ = \epsilon^-$ and the equations (2.10) and (2.11)

also reduce to the corresponding equation given in [1].

At the left boundary point (i = 1), stress $\sigma(x_1, t)$ is specified as a boundary condition to simulate an impact from a striker. Velocity at the left boundary is determined by applying the compatibility equation (2.5) for the wave propagating in the negative x-direction (figure 2.6a). This gives:

$$V(x_{1}, t_{j+1}) = V(x_{2}, t_{j}) + \frac{\sigma(x_{2}, t_{j}) - \sigma(x_{1}, t_{j+1})}{\rho^{+}(1)C_{V}^{+}(1)} + \frac{\Delta t}{\rho^{+}(1)C_{V}^{+}(1)} \left\{ \frac{E_{1}^{-}(2)\epsilon^{-}(x_{2}, t_{j}) - \sigma(x_{2}, t_{j})}{\theta^{-}(2)} \right\}.$$

$$(2.12)$$

The strain calculation at the left boundary point is similar to the internal points.

$$\epsilon^{+}(x_{1}, t_{j+1}) = \epsilon^{+}(x_{1}, t_{j-1}) + \frac{\sigma(x_{1}, t_{j+1}) - \sigma(x_{1}, t_{j-1})}{E_{1}^{+}(1) + E_{2}^{+}(1)} - \frac{2\Delta t}{E_{1}^{+}(1) + E_{2}^{+}(1)} \left\{ \frac{E_{1}^{+}(1)\epsilon^{+}(x_{1}, t_{j-1}) - \sigma(x_{1}, t_{j-1})}{\theta^{+}(1)} \right\}$$
(2.13)

At the right boundary point (i = n), velocity $V(x_n, t)$ is set to zero to simulate a fixed boundary condition. Stress at the right boundary is determined by applying the compatibility equation (2.5) for the wave propagating in the positive x direction (figure 2.6c). This gives:

$$\sigma(x_n, t_{j+1}) = \sigma(x_{n-1}, t_j) + \rho^-(n)C_V^-(n)\left\{V(x_n, t_{j+1}) - V(x_{n-1}, t_j)\right\} + \Delta t \left\{\frac{E_1^+(n-1)\epsilon^+(x_{n-1}, t_j) - \sigma(x_{n-1}, t_j)}{\theta^+(n-1)}\right\}$$
(2.14)

The strain calculation at the right boundary point is also similar to the internal points.

$$\epsilon^{-}(x_{n}, t_{j+1}) = \epsilon^{-}(x_{n}, t_{j-1}) + \frac{\sigma(x_{n}, t_{j+1}) - \sigma(x_{n}, t_{j-1})}{E_{1}^{-}(n) + E_{2}^{-}(n)} - \frac{2\Delta t}{E_{1}^{-}(n) + E_{2}^{-}(n)} \left\{ \frac{E_{1}^{-}(n)\epsilon^{-}(x_{n}, t_{j-1}) - \sigma(x_{n}, t_{j-1})}{\theta^{-}(n)} \right\}.$$
(2.15)

A MATLAB script was developed to implement the aforementioned method of characteristics and numerically model the MMHB actuator. For the numerical modeling results presented in section 2.3, time-step Δt was chosen to be 1 μ s.

2.2.4 Optimization Methodology

2.2.4.1 Design Parameters

A numerical model for the MMHB actuator dynamics is based on the method of characteristics as elaborated in section 2.2.3.2. A theoretical background review for numerical modeling is presented in section 2.2.3.1. The design of the MMHB is obtained by coupling this dynamical model with an optimization algorithm in order to replicate the target stress profile. The MMHB actuator design problem involves geometric variables, such as the lengths of the bar components. The impact between the striker and the multi-material bar gives the stress boundary condition at the left end of the overall bar assembly. This incident stress pulse is specified to have a single half-wavelength sinusoidal form similar to the one shown in figure 2.1b. In practice, such an incident stress pulse is typically generated by an impact from a spherical striker. To account for various magnitudes of impacts, the incident pulse amplitude and duration are considered as design variables. The material selection for each bar component is crucial for introducing interfaces with impedance mismatch in the multi-material bar, which is the key for transforming the incident pulse into a complicated stress

wave. Thus, the material assignment for the bar components are significant design variables.

Table 2.1 gives the details of material selection options we have considered for each of the bar components in terms of the material properties used to simulate these materials. For an N-bar assembly of the MMHB actuator, there are 2N+2 design variables: N lengths, N materials, the incident pulse duration and amplitude. The magnitude ranges for these design variables are given in table 2.2. Additionally, the optimization algorithm allows the same materials assignment for two adjacent bar components. This reduces the effective number of bar components while providing additional design flexibility.

Table 2.1: Material library for multi-material bar components. The material properties for Material ID 1-5 were taken from [1], and Material ID 6-12 were obtained from the ANSYS material library [2].

Material ID	Material	E_1 (GPa)	E_2 (GPa)	$ heta(\mu ext{s})$	Density (kg/m^3)
1	Epoxy	3.43	3.43	8.57	1200
2	PMMA 1	2.94	3.07	95.4	1190
3	PMMA 2	3.14	3.98	67.4	1190
4	PMMA 3	3.78	5.24	40.5	1190
5	Polycarbonate	2.3	0.73	140	1200
6	Structural Steel	200	0	-	7850
7	Stainless Steel	193	0	-	7750
8	Magnesium Alloy	45	0	-	1800
9	Gray Cast Iron	110	0	-	7200
10	Copper Alloy	110	0	-	8300
11	Aluminum Alloy	71	0	-	2770
12	Titanium Alloy	96	0	-	4620

Table 2.2: Design variables for MMHB actuator

Design Variable (Unit)	Minimum Value	Maximum Value	Step/Resolution
Length of each bar component (mm)	50	2000	1
Material ID for each bar component	1	12	1
Incident pulse amplitude (MPa)	0.1	10	0.1
Incident pulse width (ms)	0.1	2	0.01

Water was modeled as a nearly incompressible linear elastic fluid [82]; and since it was

fully confined, its bulk modulus was used as the elastic modulus. To avoid any additional variables, the length of the water column in the cylinder was fixed to 50 mm for all the optimization problems. For the numerical model, the bulk modulus of water was taken as 2.15 GPa and the density as 998 kg/m^3 [83].

2.2.4.2 Optimization Algorithm

An optimization problem with multiple conflicting objectives has a set of Pareto optimal solutions instead of a single solution [84]. The Non-dominated Sorting Genetic Algorithm II (NSGA-II) is an evolutionary optimization algorithm that is widely used to find a set of optimal solutions for such a multi-objective optimization problem [85]. NSGA-II is a population-based optimization algorithm. First, the objective functions, lower and upper bounds for the variables, and the population size for the set of solutions are specified. Then, a random set of solutions termed as the initial population is created by the algorithm by assigning random values to the variables. Next, the fitness values are determined for all the initial solutions based on the objective functions. The algorithm further creates a children population by performing selection, crossover, and mutation operations on the initial population. Here, the selection operator gives more importance to the solutions with higher fitness values; the crossover is analogous to reproduction, and the mutation operator mimics genetic mutation. A survivor operator is then used to create a new population by selecting the fittest and diverse set of solutions from both the initial and children populations. Lastly, the initial population is replaced with the new population, and the cycle is repeated for a specified number of generations. After performing a sufficiently large number of generations, which is specified in advance, the fittest and diverse solutions from the resultant population can be considered as optimal solutions. Based on the trade-off between the optimal solutions, the user finally needs to choose the solutions for further implementation. The flow chart for the genetic algorithm is shown in figure 2.7.

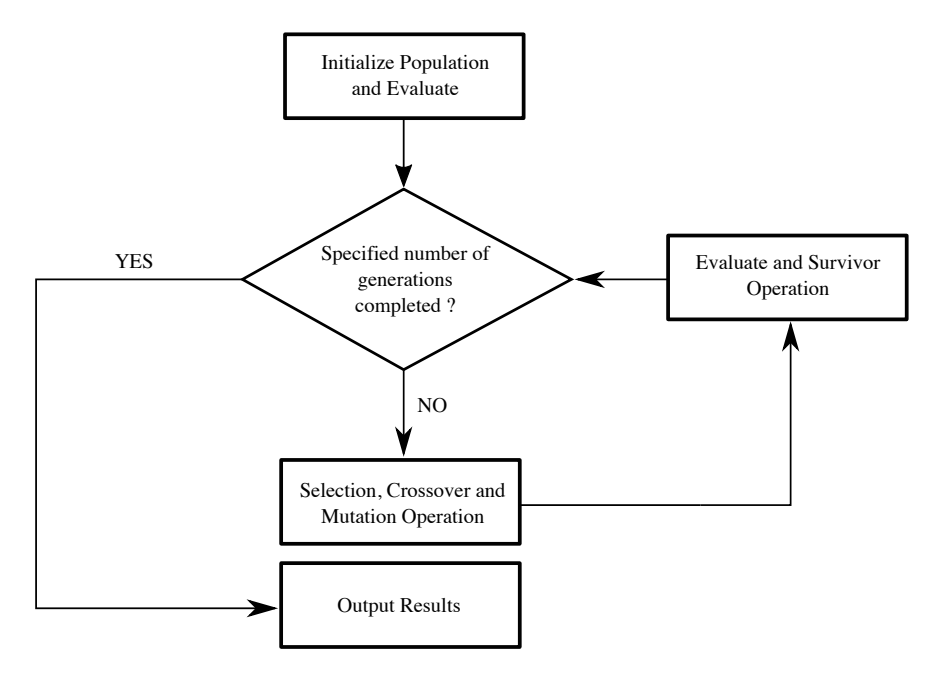


Figure 2.7: Flowchart of the optimization algorithm

2.2.4.3 Objective Functions

For every new design of the MMHB actuator, the output pressure profile inside the pressure chamber is computed from the dynamic simulation. This output pressure profile is then used to assess the performance of the actuator design based on two objective functions: (1) the error between the target pressure profile and the pressure profile generated by the actuator in the time domain, and (2) the error between these two profiles in the frequency domain.

In order to calculate both of these errors, the time-domain signal S(t) is decomposed into a sum of sinusoids using a conventional Fourier series expansion [86]

$$S(t) = \sum_{i=1}^{l} A_i \sin(\omega_i t + \phi_i), \qquad (2.16)$$

where A_i , w_i and ϕ_i are the amplitude, frequency and phase shift of the i^{th} mode. By minimizing the error between the two pressure profiles in the frequency domain, the optimization algorithm seeks to match the respective modal amplitudes of the two pressure profiles. A MATLAB script computes the Fast Fourier Transform (FFT) of the pressure profiles and calculates the root-mean-square error (RMSE) between the profiles in the separate time and frequency domain

RMSE in time domain =
$$\sqrt{\frac{\sum_{j=1}^{n} (S(t_j)^{\text{Tar}} - S(t_j)^{\text{Out}})^2}{n}}$$
 and RMSE in frequency domain = $\sqrt{\frac{\sum_{k=1}^{m} (A_k^{\text{Tar}} - A_k^{\text{Out}})^2}{m}}$. (2.17)

The superscripts Tar and Out here denote the target and output values of the shown quantity. For the RMSE calculation in the frequency domain, the frequency range was restricted to 0-10 kHz since all the dominant frequencies fell into this range.

The RMSE in the time domain accounts for the mismatch in both the amplitudes and phases of the sinusoids constituting the profiles. However, the RMSE in the frequency domain only accounts for the mismatch in the amplitudes, which emphasizes replicating the spectral characteristics rather than an exact match of the waveforms in the time domain. These objectives can be conflicting as the optimized MMHB actuator may not achieve the best match for amplitudes and the phases simultaneously. Thus, this problem is treated as a bi-objective optimization problem.

For optimizing the MMHB actuator design, numerous designs need to be simulated and evaluated for their performance. This simulation process becomes time-intensive for a large number of designs. Our custom-developed script based on the method of characteristics offers a significantly faster evaluation of performance than finite elements-based commercial

software, and it is easier to integrate with the optimization algorithm because it is also written in MATLAB. This seamless integration of the simulation and optimization scripts increases the time-efficiency of the process.

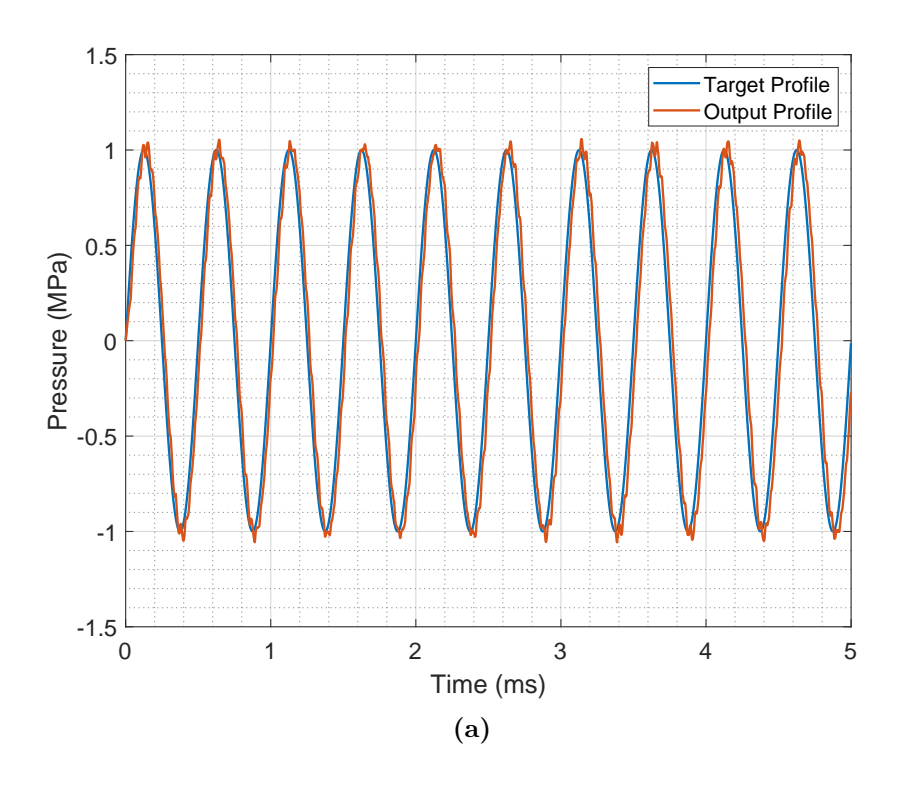
2.3 Results

The methodology to design the MMHB actuator is demonstrated by devising the actuator to generate various target pressure profiles composed of decaying and non-decaying sinusoids. Solutions to these optimization problems are discussed in this section.

2.3.1 Case Study-I: Single Frequency Sine Wave

For the first test problem, a sinusoidal wave with 2 kHz frequency and 1 MPa amplitude was chosen as the target profile. Since the target profile had a single frequency, the number of bar components was set to 1 for the optimization problem. The NSGA-II optimization algorithm was employed with a population size of 100, and the number of generations was set to 100. Thus in total, 10000 MMHB actuator designs were simulated during the optimization process. This contrasts with the 10⁸ number of possibilities in the overall design space, based on the variables and ranges detailed in table 2.2. The optimum design was chosen to be the design with the least RMSE in the frequency domain. The time and the frequency domain comparison between the target pressure profile and the pressure profile generated by the optimized MMHB actuator are shown in figures 2.8a and 2.8b. The design details for the optimized actuator are listed in table 2.3.

For this case study, even though the incident bar consists of a single material, the water effectively adds an additional interface. Thus, wave reflection, transmission, and interference



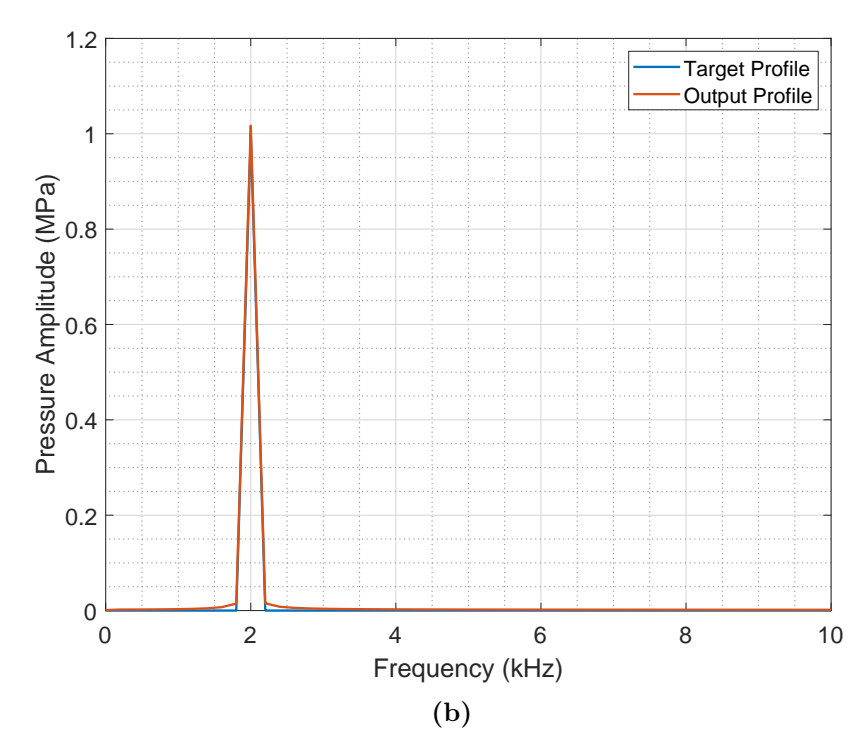


Figure 2.8: (a) Time domain and (b) frequency domain comparison between the target pressure profile and the output pressure profile generated by the optimized MMHB actuator for case study-I

remain in the system. This phenomenon makes it difficult to predict the pressure profile analytically, and so necessitates numerical simulation. However, if the assembly is simply a single-material bar without water, as shown in figure 2.1a (Case 1), the stress profile at the end of the bar can be predicted analytically (shown in figure 2.2a).

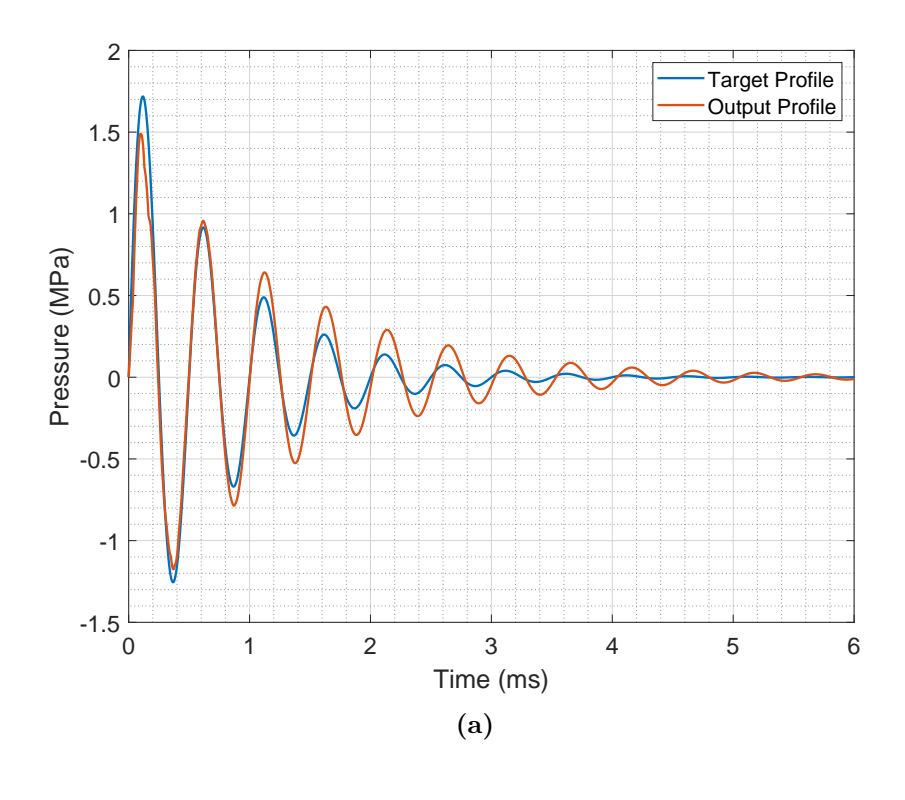
2.3.2 Case Study-II: Single-frequency decaying sine wave

For the second test problem, a decaying sinusoidal wave with 2 kHz frequency, 2 MPa amplitude, and 0.1 decay coefficient was chosen as the target profile. In particular, the target profile $S^{Tar}(t)$ was taken as

$$S^{\text{Tar}}(t) = Ae^{-2\pi\zeta ft}\sin(2\pi ft), \qquad (2.18)$$

where A denotes the amplitude, ζ is the decay coefficient, and f is the frequency. Again, the number of bar components was set to 1 for the optimization problem. The optimization routine was implemented with a population size of 100 and the number of generations was set to 200. In total, 20000 MMHB actuator designs were simulated during the optimization process. The optimum design was chosen to be the design with the least RMSE in the time domain. The time and the frequency domain comparison between the target pressure profile and the pressure profile generated by the optimized MMHB actuator are shown in figures 2.9a and 2.9b. The design details for the optimized actuator are listed in table 2.3.

The design optimization problem defined in this case study was also solved for a case where the number of bar components for the multi-material incident bar was set to 2. This exercise was conducted to test the robustness of the design optimization methodology. Notably, the optimum design obtained from the optimization routine resulted in both bars



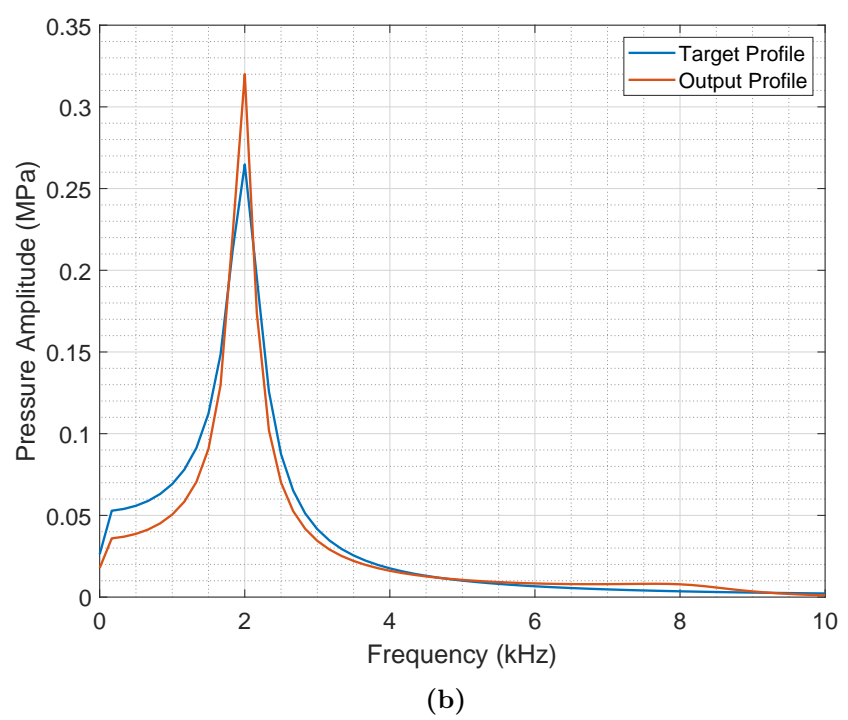


Figure 2.9: (a) Time domain and (b) frequency domain comparison between the target pressure profile and the output pressure profile generated by the optimized MMHB actuator for case study-II

being assigned the same material. Moreover, their combined length was the same as the previously obtained single-bar optimum design.

2.3.3 Case Study-III: Sum of two sinusoidal waves

For the third test problem, a sum of two sine waves with 0.5 kHz and 2 kHz frequencies, and 1 MPa and 0.5 MPa amplitudes was used as the target profile. Since the target profile contained more frequencies compared to previous target profiles, the number of bar elements was set to 2 for the optimization problem. The optimization routine was implemented with a population size of 100 and the number of generations was set to 500. Thus in total, 50000 MMHB actuator designs were simulated during the optimization process. This again contrasts with the huge number of possibilities in the overall design space. Due to the two bar components, the possibilities in the overall design space are significantly higher than the 10^8 possibilities available for the case of a single component MMHB actuator. Figure 2.10 shows the set of solutions obtained from the optimization process. The solutions are plotted in the objective space, i.e., the axes of the graphs are the objective functions. It is clear that the objective functions are conflicting, and there is a trade-off between the solutions in terms of the objective values. The time and the frequency domain comparison between the target pressure profile and the pressure profile generated by the optimized MMHB actuator designs are shown in figures 2.11a and 2.11b. The optimized designs chosen for the comparison were the design with the best match in the frequency domain, the design with the best match in the time domain, and the design with a moderate match in both the frequency and time domains. The design details for the optimized actuators are listed in table 2.3.

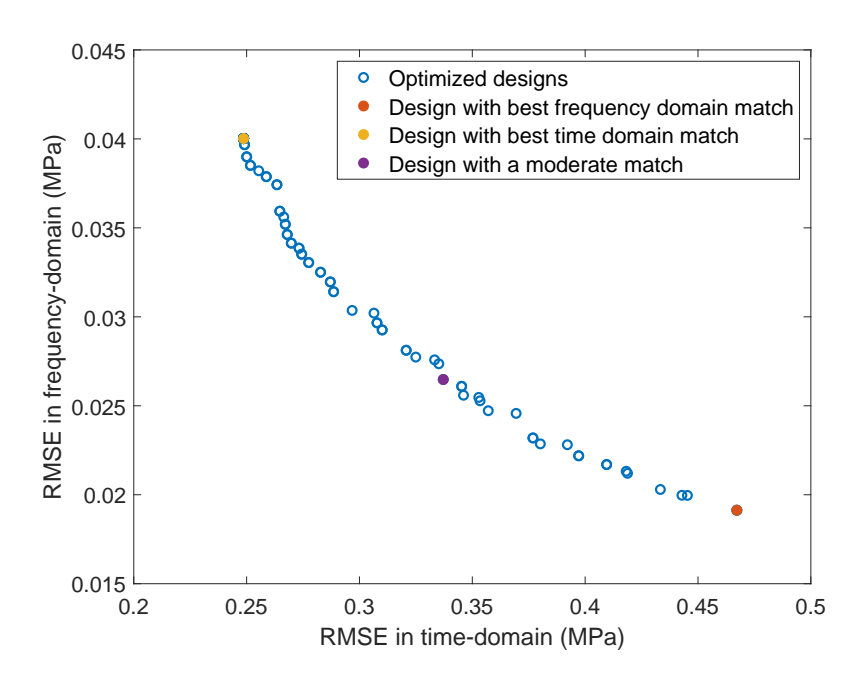
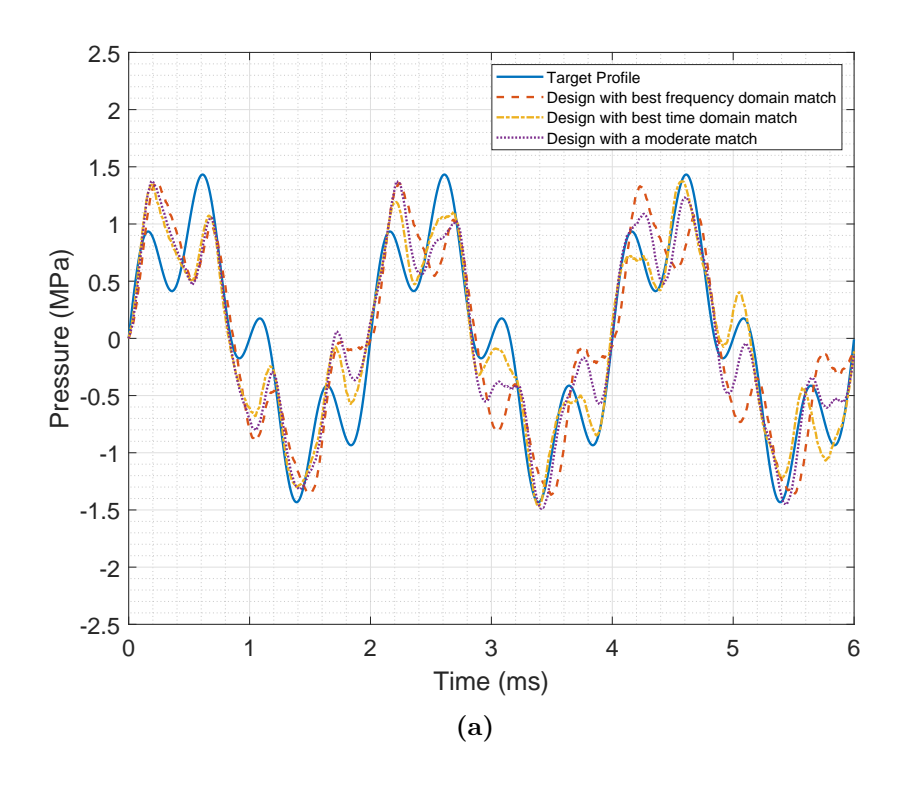


Figure 2.10: The set of optimization solutions obtained for the case study-III. These solutions are plotted in the objective space where the axes denote the optimization objective functions

2.3.4 Case Study-IV: Sum of three sinusoidal waves

For the fourth test problem, a sum of three sine waves with frequencies of 0.5 kHz, 1kHz, and 2 kHz, and amplitudes of 2 MPa, 1.5 MPa, and 1 MPa was used as the target profile. Since the target profile included a higher number of frequencies, the number of bar elements was set to 5 for the optimization problem allowing the MMHB actuator to generate more complex and dynamic pressure profiles. The optimization algorithm was employed with a population size of 100 and the number of generations was set to 1000. Thus in total, 100000 MMHB actuator designs were simulated during the optimization process. The time and the frequency domain comparison between the target pressure profile and the pressure profile generated by the optimized MMHB actuator designs are shown in figures 2.12a and 2.12b. The optimized designs chosen for the comparison were the design with the best match in the frequency domain, the design with the best match in the time domain, and the design



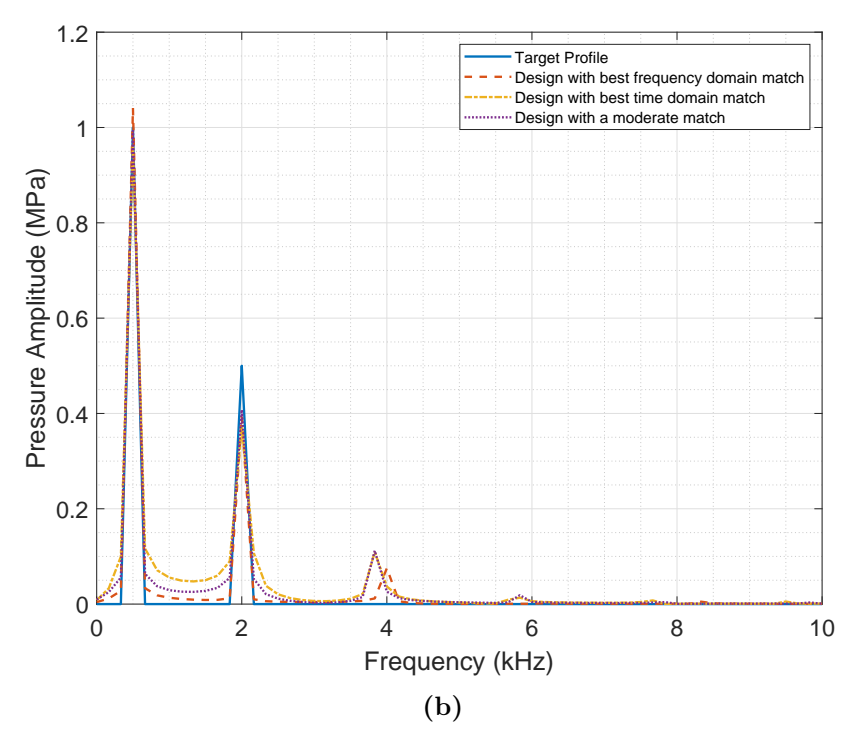
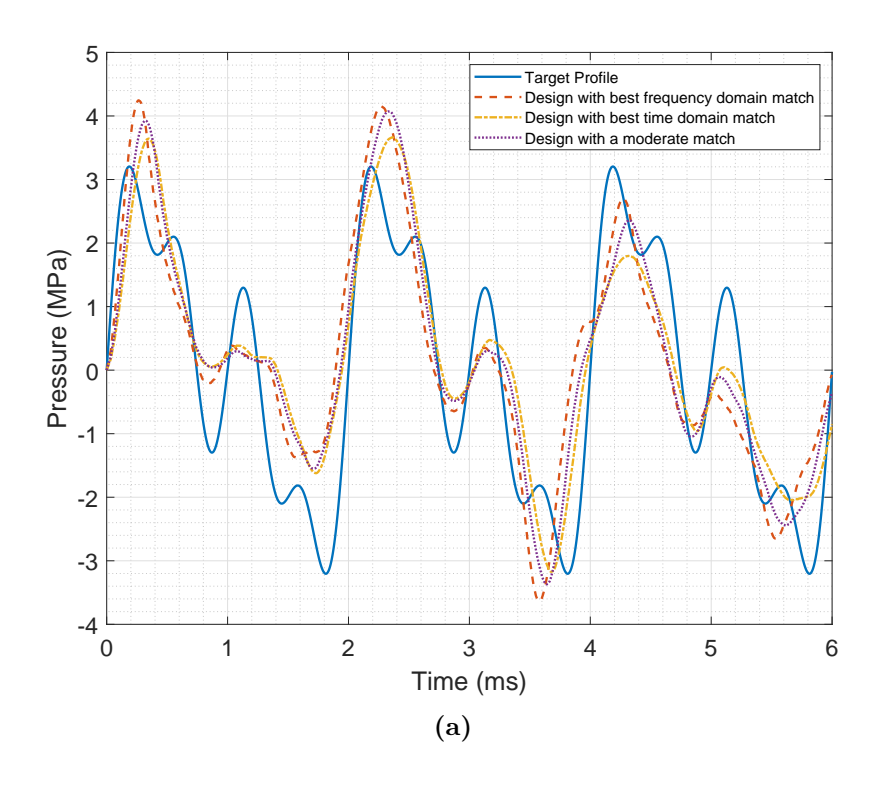


Figure 2.11: (a) Time domain and (b) frequency domain comparison between the target pressure profile and the output pressure profile generated by the optimized MMHB actuator for case study-III



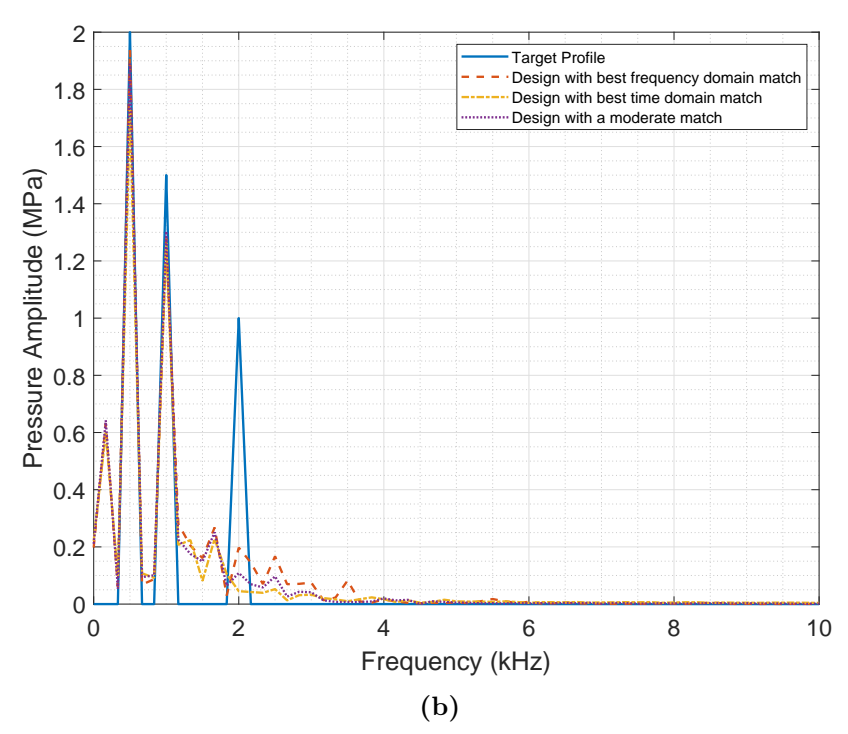


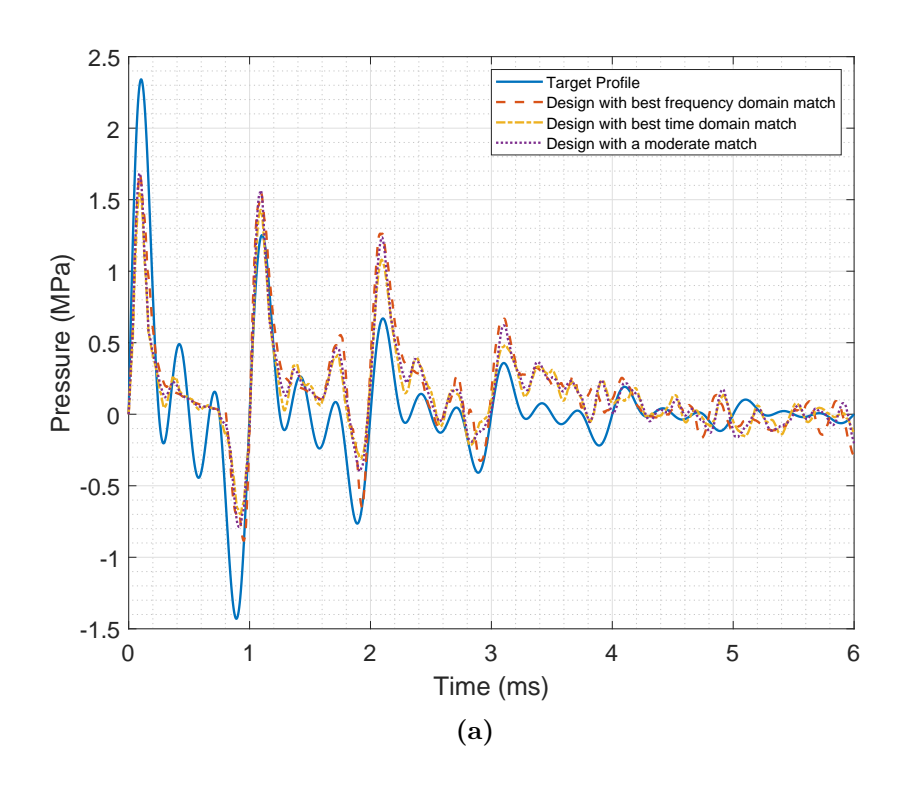
Figure 2.12: (a) Time domain and (b) frequency domain comparison between the target pressure profile and the output pressure profile generated by the optimized MMHB actuator for case study-IV

with a moderate match in both the frequency and time domains. The design details for the optimized actuators are listed in table 2.3.

For this case study, even if the number of bar components for the multi-material bar was set to 5, the optimization algorithm was allowed to assign the same materials to adjacent bars which would effectively reduce the number of bar components. That is what exactly happened here. All of the optimal designs involved two adjacent bar components with the same material specification. The resulting optimal designs were effectively 4 component bars.

2.3.5 Case Study-V: Sum of three decaying sinusoidal waves

For the fifth test problem, a sum of three decaying sinusoidal waves with frequencies of 1, 2, and 3 kHz, amplitudes of 1 MPa each, and decay coefficients 0.1, 0.05, and 0.033 was chosen as the target profile. Like the previous test problem, the number of bar components was set to 5 for the optimization problem. The optimization routine parameters were also kept the same as in the previous test problem. The time and the frequency domain comparison between the target pressure profile and the pressure profile generated by the optimized MMHB actuator designs are shown in figures 2.13a and 2.13b. The optimized designs chosen for the comparison were the design with the best match in the frequency domain, the design with the best match in the time domain, and the design with a moderate match in both the frequency and time domains. The design details for the optimized actuators are listed in table 2.3.



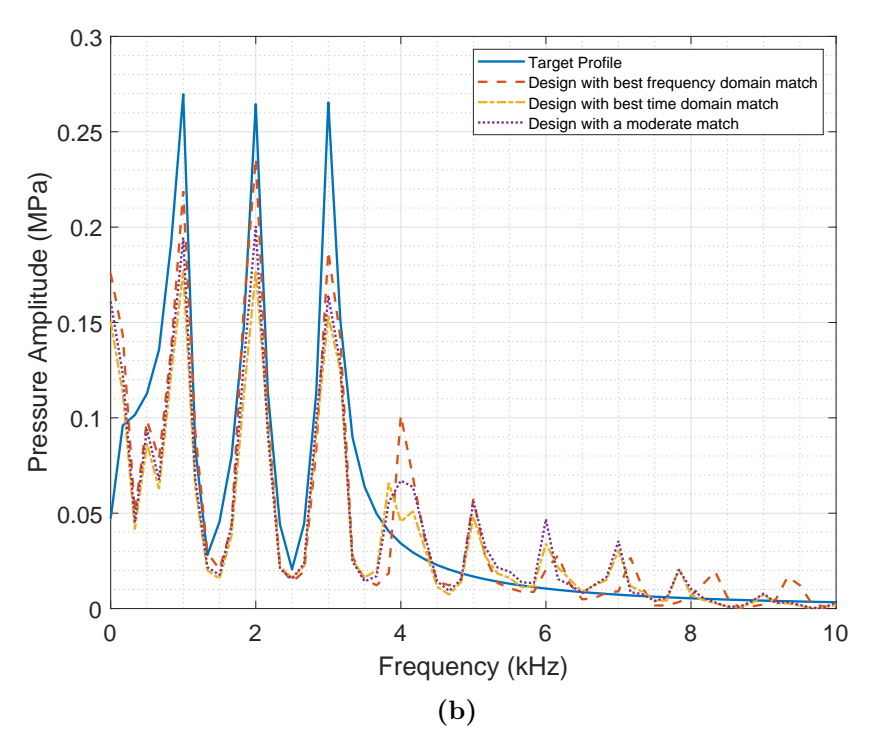


Figure 2.13: (a) Time domain and (b) frequency domain comparison between the target pressure profile and the output pressure profile generated by the optimized MMHB actuator for case study-V

Table 2.3: RMSE values and the optimized actuator design parameters for the MMHB optimization case studies

Case Study	No. of Bar Components	RMSE in Time domain (MPa)	RMSE in Frequency domain (MPa)	$\begin{array}{c} \text{Length of Bar} \\ \text{Components} \\ \text{(mm)} \end{array}$	Material IDs	Pulse Amplitude (MPa)	Pulse Width (ms)
I	1	0.169	0.0047	90	11	1.3	0.1
II	1	0.091	0.0119	158	4	1.3	0.13
III	2	0.467	0.0191	[1062, 103]	[11, 10]	2	0.24
		0.249	0.04	[1274, 50]	[11, 11]	2	0.23
		0.337	0.0265	[1192, 50]	[11, 10]	2.1	0.22
IV	5	1.137	0.1541	[1600, 1726, 1826, 1998, 1999]	[8, 11, 6, 8, 8]	5.5	0.35
		0.971	0.1647	[1434, 1995, 1819, 2000, 2000]	[8, 11, 6, 8, 8]	4.1	0.47
		1.036	0.1578	[1537, 1847, 1786, 2000, 2000]	[8, 11, 6, 8, 8]	4.6	0.43
V	5	0.281	0.0312	[637, 141, 107, 1930, 704]	[5, 10, 11, 12, 5]	7.2	0.12
		0.269	0.0345	[642, 527, 67, 1686, 704]	[5, 12, 7, 12, 5]	5.6	0.13
		0.270	0.0328	[642, 527, 64, 1681, 704]	[5, 12, 9, 12, 5]	6	0.13

2.4 Discussion

Special purpose actuators are proposed on the basis of modifying the conventional SHPB design for the purpose of generating complex loading profiles. Instead of a conventional single material incident bar, a multi-material incident bar is employed to alter the dynamic nature of the incident pulse. The design of the MMHB actuator is specifically optimized to generate a pressure profile similar to a given target pressure profile. The MMHB actuator design optimization was conducted for various target profile case studies that included a sum of decaying and non-decaying sinusoids within the target pressure profile.

For the first two case studies, the target pressure profiles contained single frequency sinusoids, and the pressure profiles generated by the optimized MMHB actuator were in good agreement with these target pressure profiles. There wasn't any significant trade-off between the optimum solutions obtained on the basis of the time domain comparison vs. a frequency domain comparison. For the third case study, the target pressure profile was a sum of two sinusoids. The pressure profile generated by the optimized actuator was able to fairly replicate the dynamics of the target pressure profile. Lastly, for the case studies IV and V, the target pressure profiles were composed of three sinusoids. The pressure profiles

generated by the optimized actuators for these test problems were not able to capture all the spectral components of the target pressure profiles. As the spectral complexity of the target pressure profile increases, the spectral characteristics of the pressure profile generated by the optimized actuator deviates from that of the target pressure profile.

Presumably, a higher number of bar elements constituting the multi-material incident bar and a wide range of material selection options will give additional flexibility to the optimization algorithm to design actuators that can replicate even more complicated loading profiles. However, as the number of rod components used to construct the multi-material incident bar increases, the total length of the actuator will increase as well as its complexity for experimental settings. This increased length of the actuator may limit its applicability because of the laboratory space or experimental constraints.

A strategy that is not considered in this study is to use a parallel combination of bars that have been each previously optimized as in the above-explored case studies. That is, a design employing several multi-material bars connected in parallel with each other could possibly replicate a multi-frequency pressure profile better than that of a single multi-material bar. While a strategy like this could have more flexibility than single multi-material bars, its implementation will bring new challenges that should be the subject of future studies.

For the numerical modeling of the MMHB actuator, water was modeled as a nearly incompressible linear-elastic fluid; and for simplicity, the cavitation phenomenon associated with water was not incorporated in the numerical modeling. The cavitation phenomenon is linked to the formation, expansion, and collapse of the bubbles when a liquid is exposed to large negative pressures [25,30,87]. Consequently, any cavitation of water in the cylinder may saturate the negative pressure part of the loading profiles. Future studies should consider a more specific equation of state for the water constituent that accounts for pressure-density

variations and cavitation phenomenon [5].

The presented actuator design can be implemented to generate a stress wave that has userdefined temporal and spectral characteristics. The actuator allows the users to investigate the response of the specimen to real world loading conditions in a lab environment. Unlike the other experimental techniques, this actuator might facilitate the repeatable production of complex stress wave seen in high-impact loadings.

The MMHB actuator suffers from some limitations that are inherent to the SHPB system. The MMHB actuator can get bulky as the number of bar components used to build the multi-material bar increases. Moreover, based on the target loading profile, the MMHB actuator's design needs to be optimized, and a new multi-material incident bar needs to be built. These design changes for every new target loading profile make the implementation of the MMHB actuator costly and time-intensive, which can significantly limit its usability. These limitations of the MMHB actuator inspired the design of the experimental apparatus presented in the next chapter.

Chapter 3

Generator of Broadband Pressure

Cycles

3.1 Introduction

This chapter introduces the apparatus created for generating broadband pressure cycles.

The principal idea presented here is implementing a piezoelectric actuator to compress water confined in piston-cylinder assembly to generate complex and fast-varying pressure profiles.

This chapter is organized as follows. Section 3.2 discusses the working principle and the fabricated design of the apparatus. A simplistic numerical model analyzing the apparatus is also discussed in this section. Section 3.3 discusses the system identification methodology used to characterize the input-output relation of the apparatus. A feedforward controller designed based on the system identification data to generate user-defined pressure profiles is also detailed in this section. The results from experiments conducted to generate various pressure profiles using the apparatus are discussed in section 3.4. Lastly, section 3.5 concludes the discussion on the experimental apparatus.

3.2 Design

3.2.1 Working Principle

Pressure is a surface loading that compresses a specimen from all directions. In this study, a piston-cylinder assembly filled with water (figure 3.1) was used as a variable-volume confinement for generating pressure loading. Water is considered a nearly incompressible fluid because of its very high bulk modulus of 2.15 GPa [83]; hence, its pressure rises sharply as a response to relatively small volume changes.

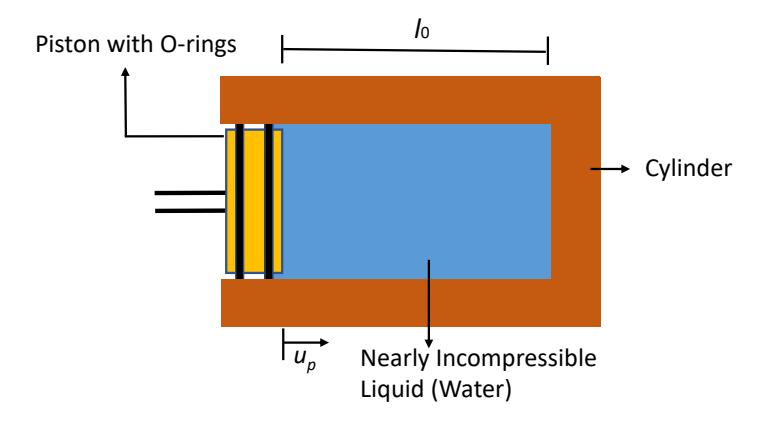


Figure 3.1: A piston-cylinder assembly (l_0 : initial length of the water volume inside the cylinder, u_p : displacement of the piston)

The change in pressure inside the cylinder, ΔP , can be estimated using the Hooke's law for volumetric loading [82,88] given by the equation,

$$\Delta P = -K \frac{\Delta V}{V_0},\tag{3.1}$$

where K is the bulk modulus for water, V_0 is the initial volume of water inside the cylinder, and ΔV denotes the change in volume of water. Assuming the cylinder walls to be perfectly rigid and the cylinder having a uniform cross-section, equation (3.1) can be further simplified to

$$\Delta P = K \frac{u_p}{l_0}. (3.2)$$

Here, l_0 and u_p denote the initial length of the water volume inside the cylinder and the displacement of the piston respectively as shown in figure 3.1. As the bulk modulus of water is extremely high, even a piston displacement of a few micrometers can generate a high pressure spike inside the cylinder, equivalent to a blast event. A piezoelectric stack actuator (Model P885.95 Physik Instrumente (PI) GmbH & Co. KG, Karlsruhe, Germany) was used to drive the piston in the piston-cylinder assembly. The piezoelectric actuator expands when a voltage signal is applied across its leads. By expanding, the actuator displaces the piston, compressing the water inside the cylinder and raising the pressure as a result. The time scale of this actuation is of the order of a few microseconds; this is fast enough to generate pressure loadings similar to those of a blast event (typically lasting for a few milliseconds). A high-frequency pressure transducer (Model 113B27 PCB Piezotronics Inc., Depew, NY, USA) measures the pressure inside the cylinder to give feedback about the actual performance of the piezoelectric actuator.

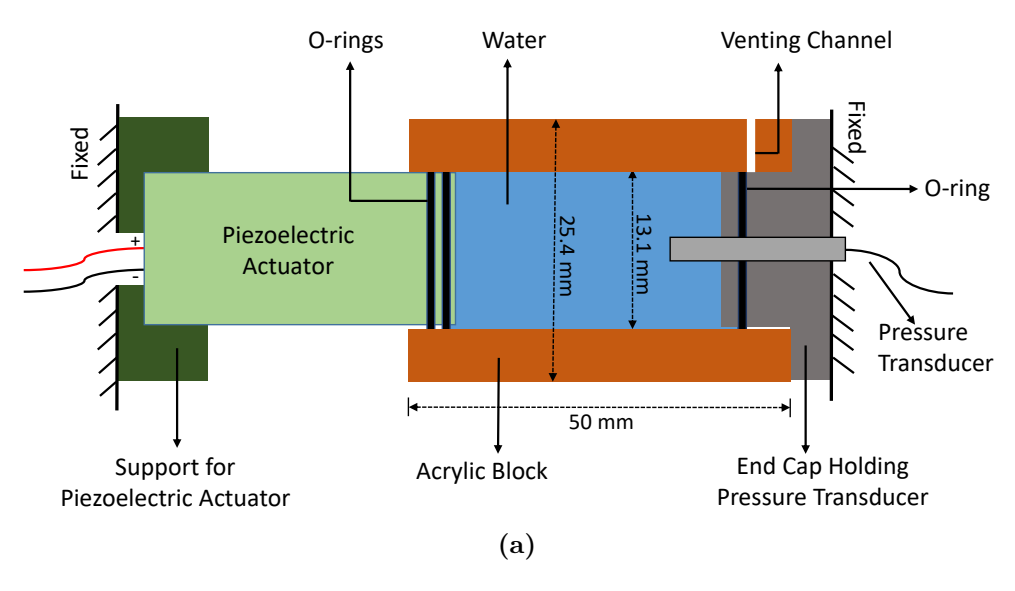
3.2.2 Device Fabrication

This section discusses the two design iterations of the pressure apparatus. The limitations observed in the first-iteration design of the pressure apparatus necessitated a design revision.

3.2.2.1 Design Iteration I

A pressure chamber was machined from an acrylic rod (square cross-section $25.4\,\mathrm{mm}$ × $25.4\,\mathrm{mm}$) by drilling a through-hole of $13.1\,\mathrm{mm}$ diameter. A custom end-cap was designed

and machined from an acrylic rod (circular cross-section with 25.4 mm diameter) to hold the pressure transducer as well as seal one end of the chamber. The other end of the chamber was sealed using a piezoelectric actuator and O-rings. A venting channel, i.e. a circular hole with 1.6 mm diameter drilled perpendicular to the pressure chamber axis, was incorporated in the pressure chamber to remove air bubbles and excess water while filling the chamber. The design of the venting channel is similar to the one implemented in [30]. The schematic and the fabricated design of the apparatus are shown in figures 3.2a and 3.2b. The assembly was held together using a fixture built from acrylic plates and steel threaded rods. This



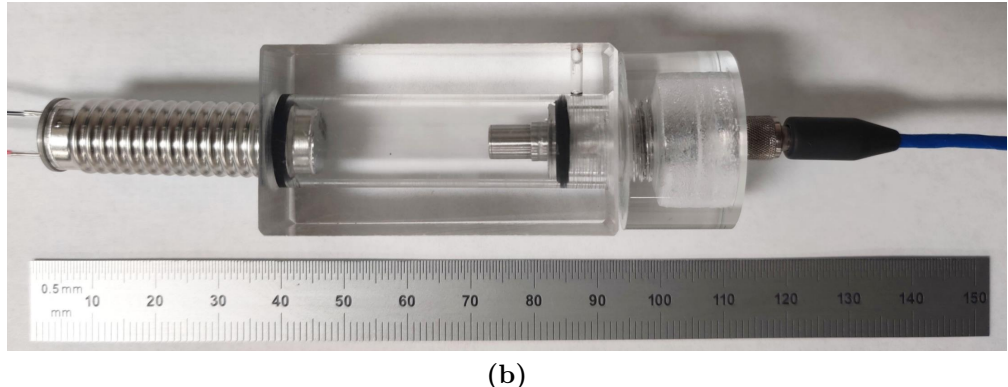


Figure 3.2: (a) Cross-sectional schematic view and (b) Fabricated design of the pressure apparatus (Design iteration I)

fixture was also used to pre-compress the assembly to remove any slack that would prevent effective compression. The complete setup of the apparatus including the fixture is shown in figure 3.3.

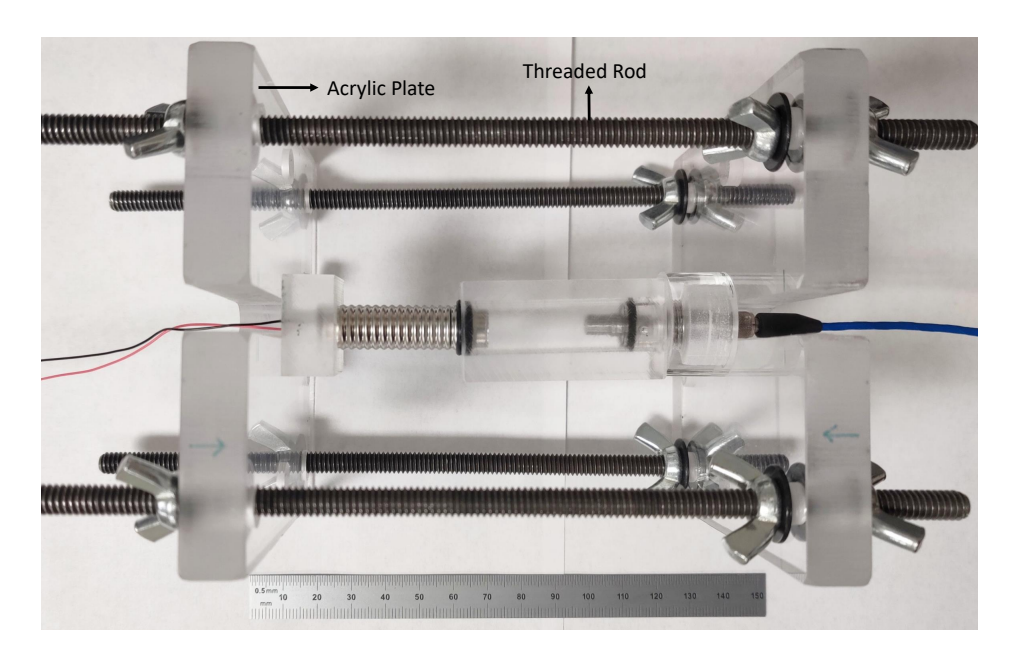


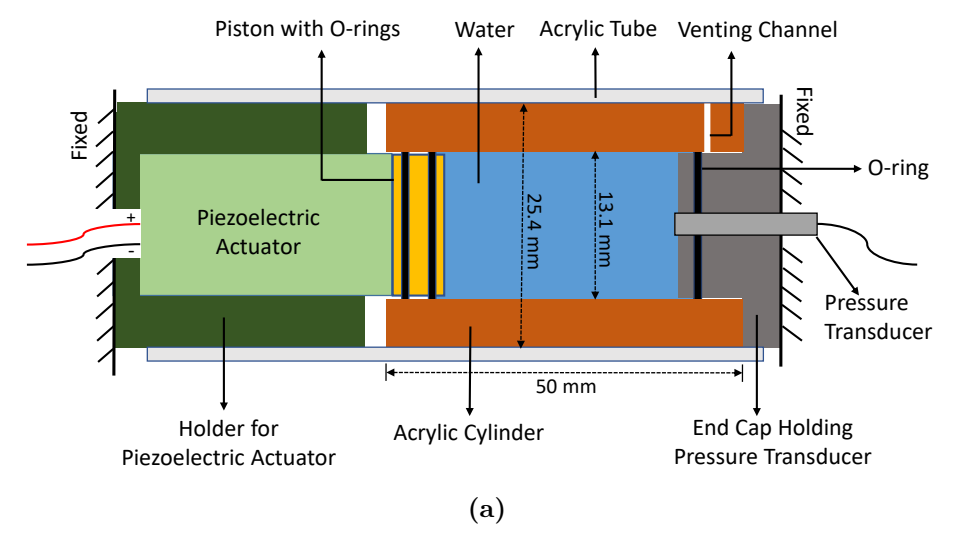
Figure 3.3: The complete assembly of the pressure apparatus (Design iteration I)

This fabricated design was used to conduct preliminary ex-vivo and in-vitro experiments involving mouse brain slices and HeLa (Henrietta Lacks) cell cultures. The details of these preliminary experiments are provided in chapter 6 (sections 6.1.1 and 6.2.1). This fabricated design was observed to have some design flaws which were limiting the performance of the apparatus. Firstly, for sealing the actuator side of the pressure chamber, O-rings were placed between the metal bellows of the piezoelectric actuator and the inner wall of the pressure chamber. Since the metal bellows were easily deformable, a good reliable seal was not achieved with this arrangement. This improper seal would result in leaks inhibiting the pressure generation. Secondly, bending of the acrylic plates was observed when the pressure chamber and actuator assembly were pre-compressed. Thus, this fixture couldn't rigidly support the assembly which directly limited the pressure generation. Lastly, the method

used for supporting the piezoelectric actuator strained the lead wires of the actuator which eventually broke the leads after a series of experiments. All of these design flaws were rectified in the second design iteration by (a) introducing a separate piston part, (b) using aluminum plates for the fixture, and (c) designing a new holder for the piezoelectric actuator.

3.2.2.2 Design Iteration II

In the new design, a cylindrical geometry was incorporated for the pressure chamber, piezoelectric actuator holder, and the end cap which held the pressure transducer. The pressure chamber was machined from an acrylic rod (circular cross-section with 25.4 mm diameter) by drilling a through-hole of 13.1 mm diameter. A new custom end-cap was designed and machined from a medical-grade SAE 316L stainless-steel rod (circular cross-section with 25.4 mm diameter) to hold the pressure transducer as well as seal one end of the chamber. The other end of the chamber was sealed using a stainless steel piston with O-rings. The same venting channel design was also incorporated. A custom stainless steel holder was machined to house the piezoelectric actuator. An acrylic tube (inner diameter 25.4 mm and outer diameter 31.75 mm) was used to align the pressure chamber and the actuator. The schematic and the fabricated design of the apparatus are shown in figures 3.4a and 3.4b. A block with a V-shaped groove to support while ensuring alignment was designed and 3Dprinted out of polylactic acid (PLA) filament. The assembly was held together using a new fixture built from aluminum plates and steel threaded rods as shown in figure 3.5a. The complete setup of the apparatus including the fixture is shown in figure 3.5b. This updated design was used for the rest of analysis discussed in this chapter and to conduct the preliminary in-vitro experiments involving cerebral organoids (discussed in chapter 6, section 6.2.2).



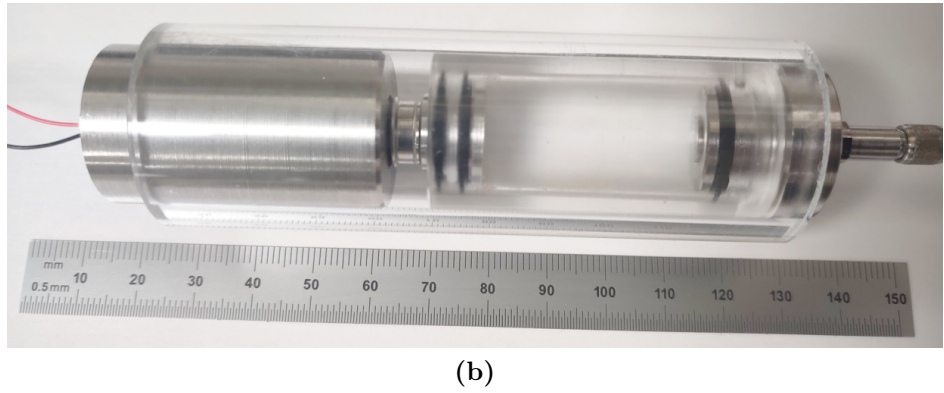
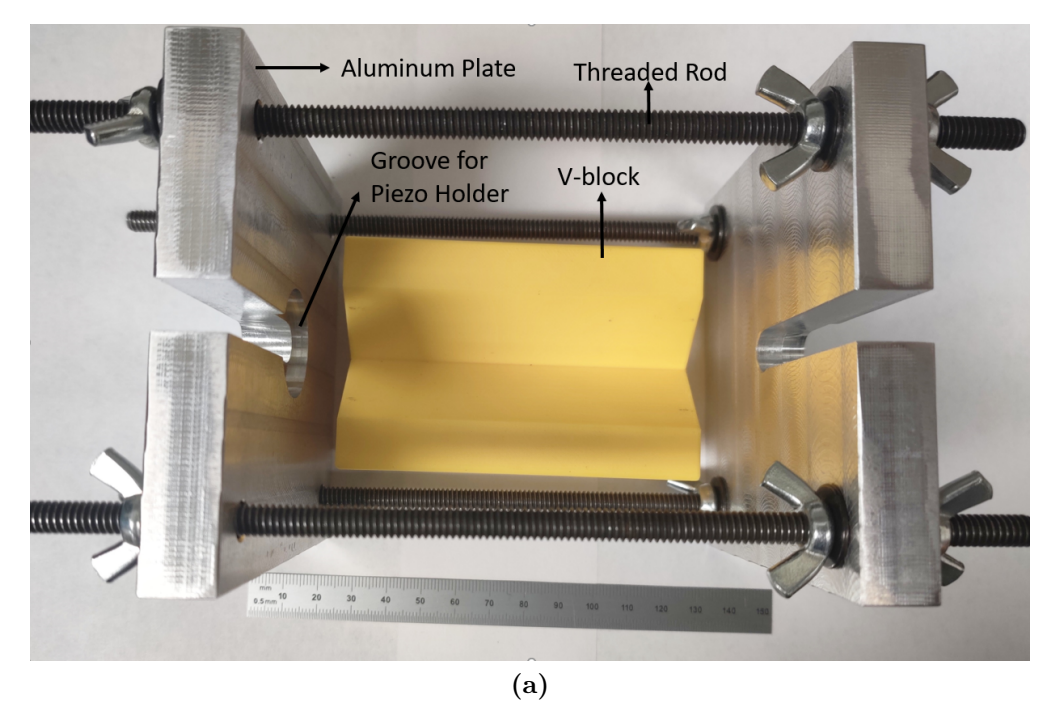


Figure 3.4: (a) Cross-sectional schematic view and (b) Fabricated design of the pressure apparatus (Design iteration II)

3.2.3 Instrumentation

The input to the apparatus was a $0-10\,\mathrm{V}$ signal. This input signal was amplified to $0-100\,\mathrm{V}$ using a power amplifier (Model E504 Physik Instrumente (PI) GmbH & Co.) and then fed to the piezoelectric actuator. The input voltage signal determined the displacement of the piston and altered the pressure in the chamber, which was measured using the pressure transducer. A signal conditioner (Model 482A21 PCB Piezotronics, Inc.) was used to amplify the pressure signal measured by the transducer, which was finally recorded using a data acquisition device (Model USB-6341 National Instruments, Austin, TX, USA). The same data



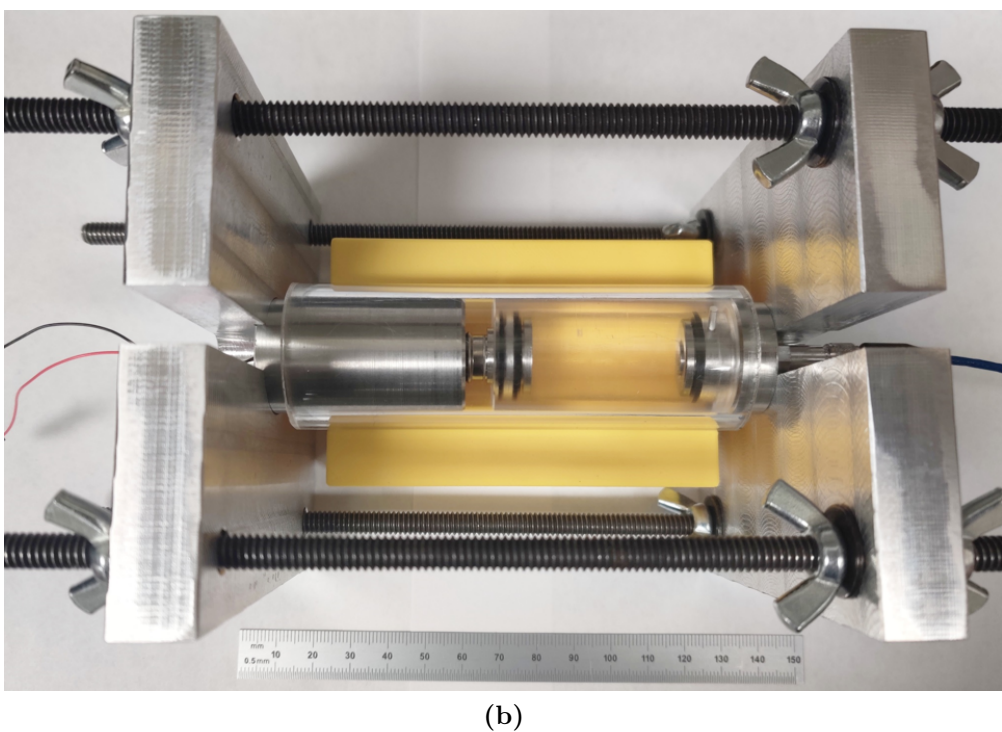


Figure 3.5: (a) Pressure apparatus fixture consisting of aluminum plates and steel threaded rods along with the supporting V-block and (b) the complete assembly of the pressure apparatus (Design iteration II)

acquisition device was also used to generate the input voltage signal. A custom LabVIEW (National Instruments) program was developed to perform and synchronize both the signal generation and the data acquisition tasks at the sampling frequency of 100 k samples per second.

3.2.4 Numerical Model

A numerical model of the apparatus was developed to further analyze the pressure generation mechanism and estimate the theoretical limit of maximum pressure that could be achieved. The pressure chamber, along with the piston and the end-cap, was modeled as a one-dimensional domain as shown in figure 3.6. This assembly was simulated by solving the one-dimensional wave propagation equation,

$$\frac{\partial^2 u}{\partial t^2} = \alpha^2 \frac{\partial^2 u}{\partial x^2},\tag{3.3}$$

which has one dependent variable u and two independent variables t and x [81]. For a longitudinal stress wave traveling through an elastic medium, u denotes the displacement at location x and time t. The constant α in equation (3.3) denotes the speed of the longitudinal

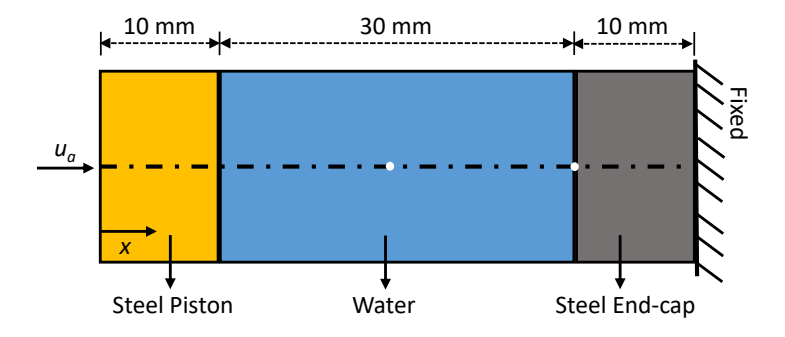


Figure 3.6: One-dimensional domain for the numerical model simulating the pressure chamber with white dots showing the locations of the nodes used for extracting pressure profiles

stress wave traveling in the elastic medium. This wave speed was determined from the elastic modulus (E) and the density (ρ) of the elastic material using the relation

$$\alpha = \sqrt{\frac{E}{\rho}}. (3.4)$$

Water was modeled as a linear elastic fluid [82]; and since it was fully confined, its bulk modulus was used as the elastic modulus. The steel parts were modeled as linear elastic solids [88]; and since they experienced uniaxial loading, Young's modulus was used as the elastic modulus for steel. The material properties (elastic moduli and densities) used for water and steel are given in table 3.1. The acoustic impedance (Z) for the wave propagation in each medium was calculated using the relation

$$Z = \alpha \times \rho. \tag{3.5}$$

Table 3.1: Material properties for the numerical model of the pressure apparatus

Material	Elastic Modulus (GPa)	Density (kg/m ³)
Water	2.15 (Bulk Modulus)	998
Steel	200 (Young's Modulus)	7850

The interfaces between water and steel were modeled as bonded interfaces sharing common nodes, implying no relative motion at the interfaces. This makes the velocity and stress fields continuous across the interfaces. The stress wave interaction at the interface was modeled using the equations:

$$\sigma_{\rm r} = \frac{Z_{\rm B} - Z_{\rm A}}{Z_{\rm B} + Z_{\rm A}} \sigma_{\rm i} \quad \text{and} \quad \sigma_{\rm t} = \frac{2Z_{\rm B}}{Z_{\rm B} + Z_{\rm A}} \sigma_{\rm i},$$
 (3.6)

where σ_i denotes the incident stress wave traveling through material A, which gets reflected from the interface as σ_r and transmits into material B as σ_t [78–80].

Displacement $u_a(t)$ was specified as a boundary condition at the left end of the piston (figure 3.6). This boundary condition physically represents the displacement provided by the piezoelectric actuator. A fixed boundary condition was specified at the right end of the end-cap (figure 3.6) to model the support by the aluminum plates and threaded rods fixture. The method of characteristics was implemented using a MATLAB (MathWorks Inc., Natick, MA, USA) script to numerically solve the one-dimensional wave propagation equation (equation (3.3)) for each of these media [81].

As a test case, a sinusoidal profile having $7 \,\mu$ m amplitude and 2000 Hz frequency was specified as a displacement boundary condition. This boundary condition mimics the displacement provided by the piezoelectric actuator at 2000 Hz operating frequency. The apparatus was simulated by numerically solving the governing equations and the pressure profiles were extracted for two locations of interest: first being the midpoint of the pressure chamber and second was the location where the pressure transducer was incorporated in the experimental setup. Figure 3.7 shows both the input displacement profile specified as the boundary condition and the pressure profiles extracted for the specified locations.

It is noticeable that the pressure profiles have the same form as the actuator displacement profile. Moreover, the two pressure profiles are almost coinciding, suggesting a minimal variation in the pressure across different locations inside the chamber. This observation supports the simplification of a hydrostatic pressure distribution inside the chamber as the piston speed ($\approx 0.05 \text{ m/s}$) is several orders of magnitude smaller than the longitudinal wave speed in water ($\approx 1500 \text{ m/s}$). Thus, the pressure generation can be directly linked to the piston displacement as stated in equation (3.2).

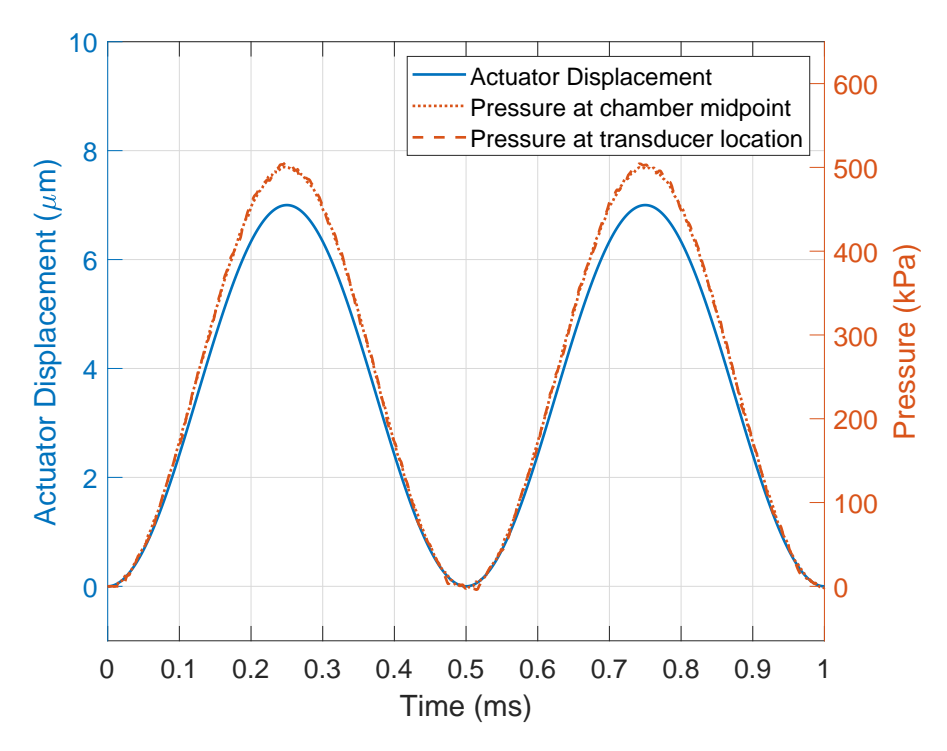


Figure 3.7: Comparison between the actuator displacement profile (left y-axis) specified as the input boundary condition to the numerical model and the output pressure profiles (right y-axis) obtained from the numerical simulation

This model of the pressure chamber is a simplistic model that doesn't account for the components with non-linear response such as deformation of the O-rings and the chamber, friction between the O-rings and the pressure chamber walls, etc. Still, it is helpful in estimating the shape and the maximum expected magnitude of the generated pressure profiles. The effect of unaccounted components in the numerical model on the performance of the apparatus was further experimentally evaluated through system identification, and a control strategy was developed to generate complex pressure profiles.

3.3 Control

To generate a user-defined, arbitrarily complex pressure loading cycle in a consistent and reproducible manner, a controller is needed for the pressure apparatus. Based on the user-specified target pressure profile, the controller needs to compute appropriate control input, i.e., an excitation voltage profile driving the piezoelectric actuator. This allows the pressure profile generated by the apparatus to closely follow the target pressure profile. In control theory, this control problem is termed as an "output tracking problem" [89]. To design such a controller for the apparatus, first, the apparatus was characterized by correlating the inputs given to the apparatus and the measured outputs. This performance characterization is known as "system identification".

3.3.1 System Identification

The pressure apparatus is a single-input single-output (SISO) system. The input to the system is an excitation voltage signal provided to the power amplifier driving the piezoelectric actuator. The output of the system is the pressure profile generated by the apparatus in response to the actuation of the piezoelectric actuator. For system identification, the response of the apparatus to various sinusoidal excitations was measured. A chirp signal, i.e., a constant amplitude sinusoid with continuously varying frequency (illustrated in figure 3.8), was given as input to the system to evaluate its frequency response. This chirp signal has a starting frequency f_o and end frequency f_T , and the instantaneous frequency f is linearly increased from f_o to f_T over the total duration of the signal (T) as given in equation

$$f(t) = f_0 + (\frac{f_T - f_0}{T}) \times t. (3.7)$$

The *chirp* function in MATLAB was used to generate this signal profile.

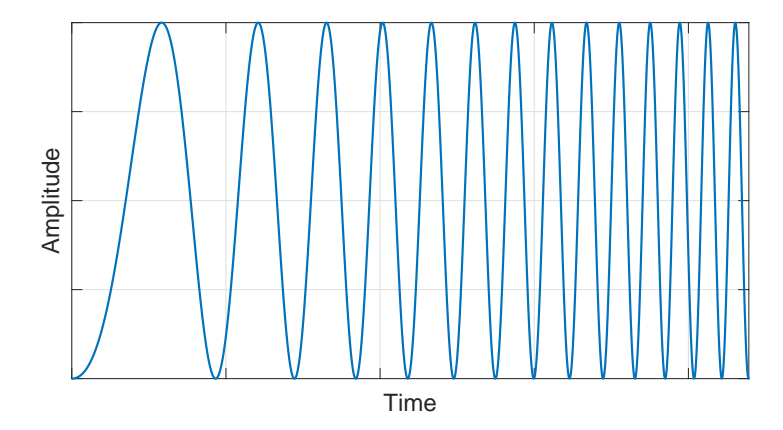


Figure 3.8: A chirp signal

To evaluate the frequency response of the system, the system was excited with chirp input signals having $f_0 = 100 \,\mathrm{Hz}$ and $f_T = 5 \,\mathrm{kHz}$ for a total duration of 100 ms. This frequency range was specifically chosen as the dominant frequencies in the ICP profiles observed in a bTBI event fall within this range [5,6]. Multiple experiments were performed to evaluate the system's response to such chirp inputs of various magnitudes. For each of the chirp signal, an offset equal to the amplitude of the sinusoids was added to make the chirp signal non-negative. The input parameters for these sine-sweep experiments are given in table 3.2.

Table 3.2: Input parameters of the sine-sweep system identification experiments conducted for the pressure apparatus

Start Frequency (Hz)	End Frequency (kHz)	Duration (ms)	Input Amplitude (V)	Number of experiments
100	5	100	2	2
100	5	100	4	2
100	5	100	6	2
100	5	100	8	2
100	5	100	10	2

As a representative result, the chirp input signal having 6 V amplitude is shown in figure 3.9a, and the corresponding output pressure profile generated by the apparatus is shown

in figure 3.9b. There was a transport delay between the input excitation and the pressure output profiles, which corresponds to the response time of the system. This transport delay was measured using the correlation-based finddelay function in MATLAB and was found to be $80\,\mu\text{s}$. This transport delay was removed from further analysis by defining a new start time for the pressure output profile. It can be observed that even though the input

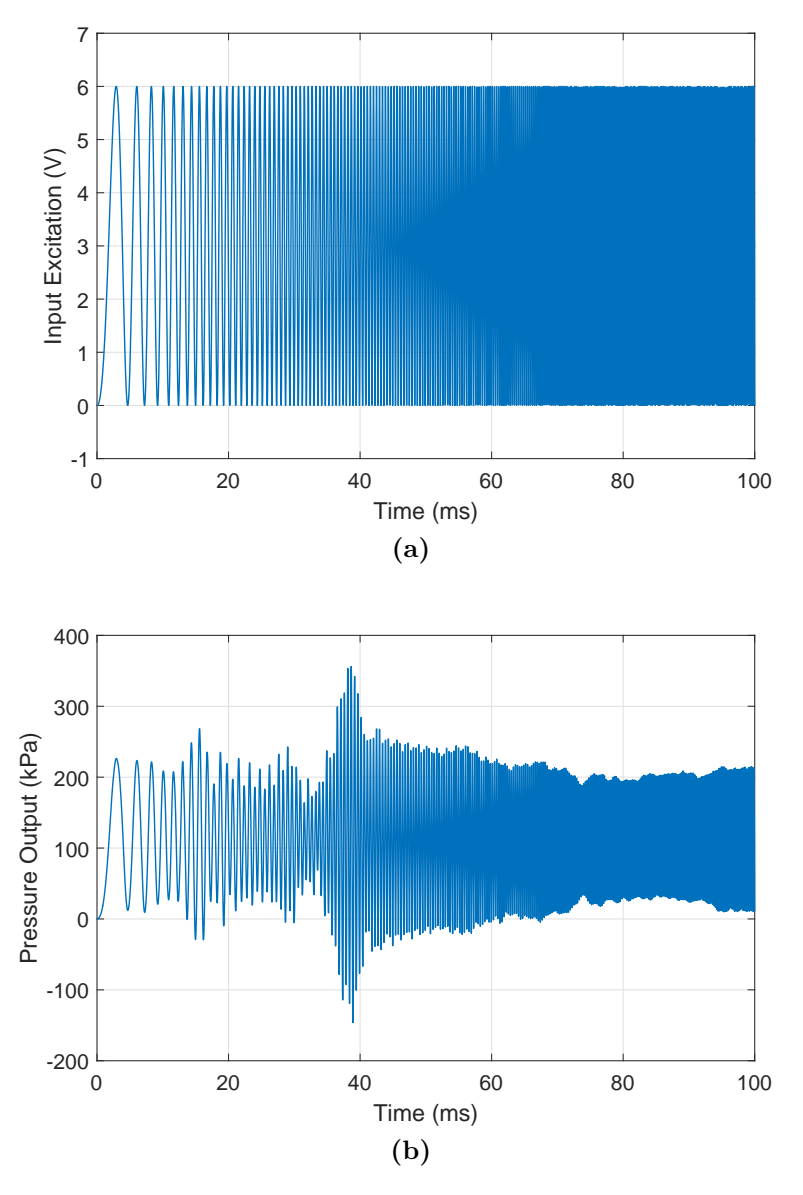


Figure 3.9: (a) Chirp voltage profile given as an input to the pressure apparatus for a system identification experiment (b) Output pressure profile generated as a response to the chirp excitation

signal had a fairly constant amplitude for all the excitation frequencies, the output pressure profile exhibits amplitude variation with input frequencies. This amplitude variation of the sinusoids constituting the input and the output profiles was quantified by analyzing the profiles in the frequency domain. The frequency-domain representation of the input and the output profiles are shown in figures 3.10a and 3.10b.

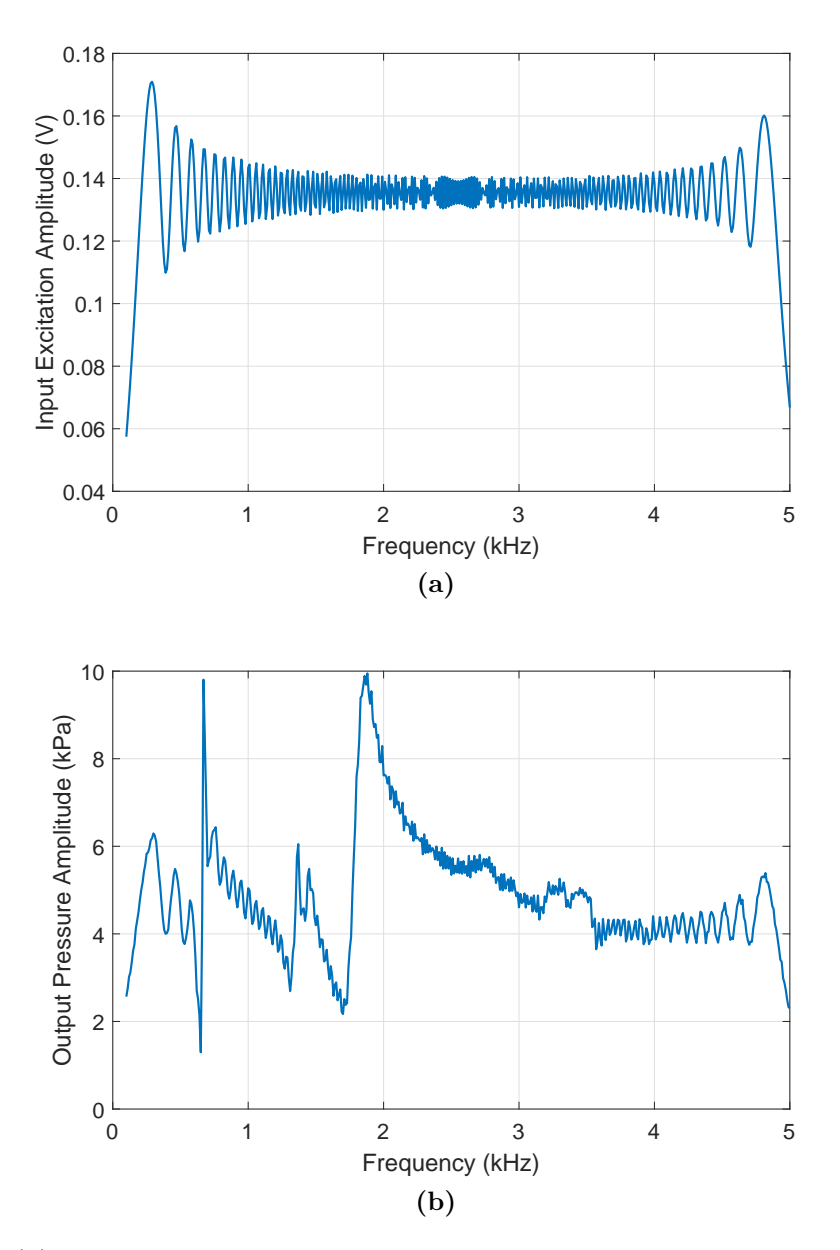
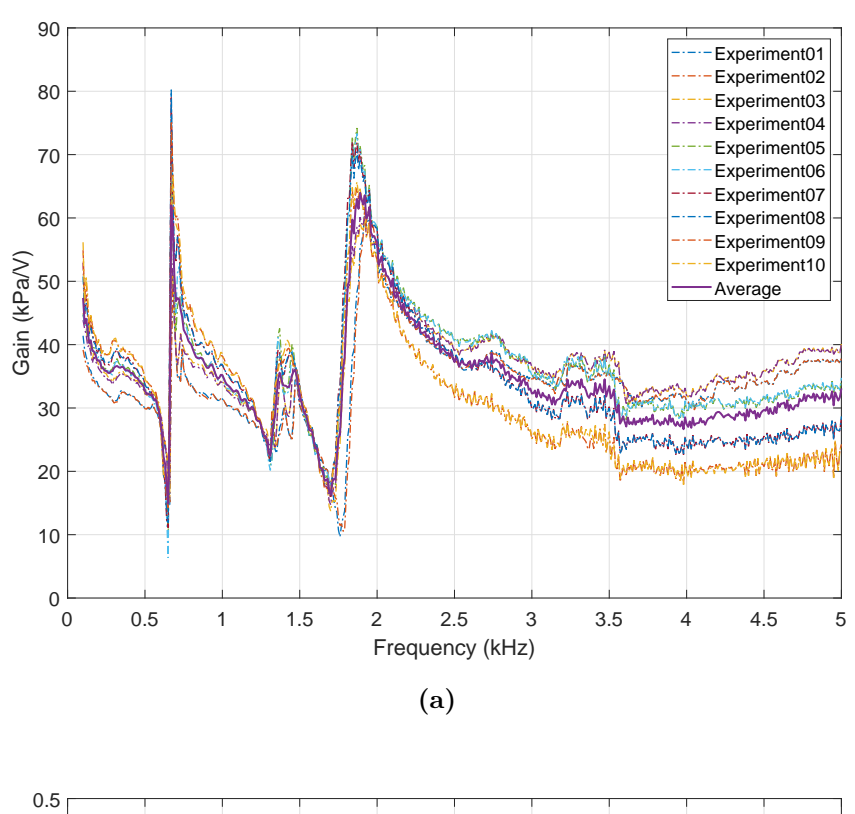


Figure 3.10: (a) Frequency-domain representation of the chirp input profile (b) Frequency-domain representation of the output pressure profile

The amplitude variation was characterized by computing the gain, i.e., the ratio of output amplitude to input amplitude for a particular frequency. The DC gain was also determined by computing the ratio between the output and input amplitudes for the zero frequency. Additionally, the phase difference between the sinusoids constituting the input and the output profiles was computed from the frequency-domain data. The gains and the phase differences for the sinusoids were determined for all the system identification experiments. These gains and the phase differences computed from the input-output data for each of the 10 experiments are shown in figure 3.11a and figure 3.11b.

The gain and the phase difference curves determined from the experimental data are consistent over all the experiments. The gain curves clearly capture the local resonances present in the system even though the exact factors causing the resonances are hard to isolate or predict analytically. The average gain and the average phase difference curve are also shown in the figures 3.11a and 3.11b. Thus, by using these average gain and the average phase difference curves, the system output can be predicted for a sinusoidal input having a frequency between 100 Hz to 5 kHz.

By knowing how the amplitudes and phases of sinusoids change from input to output and modeling the system as a linear time-invariant system [90], the response of the system can be predicted for an arbitrarily complex input profile composed of the sinusoids of these frequencies. Finally, the system identification curves, the average gain curve and the average phase difference curve, were used to design a feedforward controller for the output tracking problem.



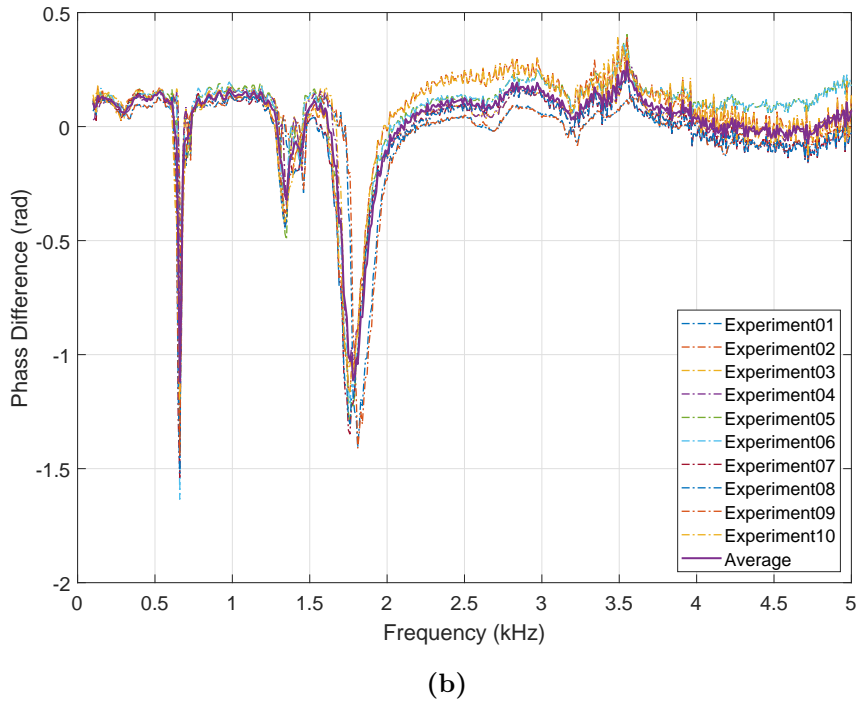


Figure 3.11: (a) Gain curves and (b) phase difference curves for the pressure apparatus determined from system identification experiments

3.3.2 Feedforward Control

For the output tracking problem, the target output profile to be tracked is provided as an input to the controller. A feedforward controller was designed to compute a control input profile such that the output generated by the system tracks the target output profile. The feedforward controller used the system identification curves, the average gain curve and the average phase difference curve, to compute the control input profile.

First, the target output profile was transformed into its frequency-domain representation to determine the amplitudes and the phases of the sinusoids of which it is composed. Then, the amplitudes of the sinusoids for the control input signal were determined by dividing the output amplitudes with corresponding gains. Also, the phases of the sinusoids for the control input signal were calculated by incorporating the phase shift from the average phase difference curve into the phases of corresponding sinusoids in the target output profile. Once the amplitudes and phases of the sinusoids were determined for the control input signal, its time-domain representation was reconstructed. This control input signal was then provided to the system and the actual experimental output profile was measured. Lastly, the target output profile and the experimental output profile were compared to evaluate the performance of the feedforward controller. The implementation and the performance of this controller were tested by tracking a multi-modal pressure profile as detailed in section ??.

3.4 Results

To assess the capabilities and the performance of the apparatus, we designed a series of experiments to generate various pressure waveforms. Initially, we test the capability of the device to generate two simple waveforms without using the feedforward control. We demonstrate the capabilities are the capabilities and the performance of the apparatus, we designed a series of experiments to generate various pressure waveforms. Initially, we test the capability of the

strate a single pulse waveform in section 3.4.1, and an approximate Friedlander waveform in section 3.4.2. Subsequently, we demonstrate the implementation of the feedforward control to generate a multi-modal waveform in section 3.4.3.

3.4.1 Single Pulse Waveform

In order to generate a single pressure pulse, a single sinusoidal voltage pulse was given as an input to the apparatus. Three such voltage excitation pulses having different pulse widths and amplitudes were constructed as detailed in table 3.3. The excitation voltage vs time graph for these pulses is shown in figure 3.12a. The corresponding pressure pulses generated as a result of these input voltage pulses are shown in figure 3.12b.

Table 3.3: Input excitation pulses constructed for generating pressure pulses

Excitation Pulse No.	Pulse Width (ms)	Pulse Amplitude (V)
1	0.50	8
2	1.75	10
3	6.00	7

It can be observed that the pressure pulses closely follow the temporal and magnitude characteristics of the input voltage pulse. Thus, by changing pulse widths and amplitudes of the input voltage pulses, pressure pulses with various pulse widths and amplitudes can be easily generated using this apparatus. Important characteristics of the pressure pulses such as maximum loading rate (kPa/ms) and total impulse, which is the area under the pressure-time curve, can also be controlled by manipulating input voltage pulse profiles. Molecular dynamics simulations suggest parameters like peak pressure, pulse duration, maximum loading rate, and total impulse have a significant effect on cell membrane deformation [91]. Thus, having an experimental apparatus that could generate various pressure loadings spanning

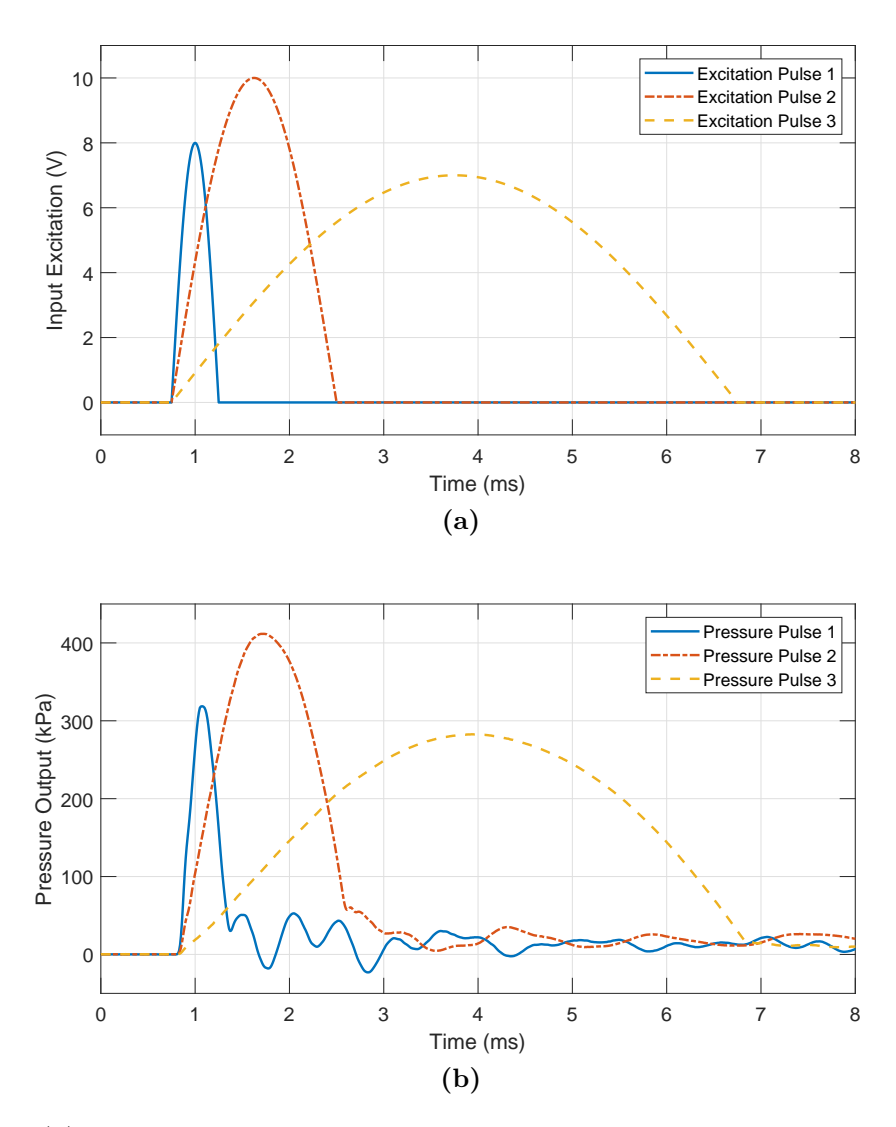


Figure 3.12: (a) Sinusoidal excitation pulses given as inputs to the apparatus. (b) Output pressure pulses generated by the apparatus for corresponding input pulses.

this parameter space facilitates to experimentally test the numerical findings.

The comparison between the pressure profile generated using a modified SHPB setup [8] and our apparatus is also shown in figure 3.13. The input excitation pulse 2 was designed in such a way that the pressure pulse generated by the apparatus has a similar pulse width and magnitude compared to the pressure waveform obtained from the SHPB experiment. Our apparatus could not only replicate the pressure generation capabilities of an SHPB setup but also exceed them in terms of generating tunable pressure profiles.

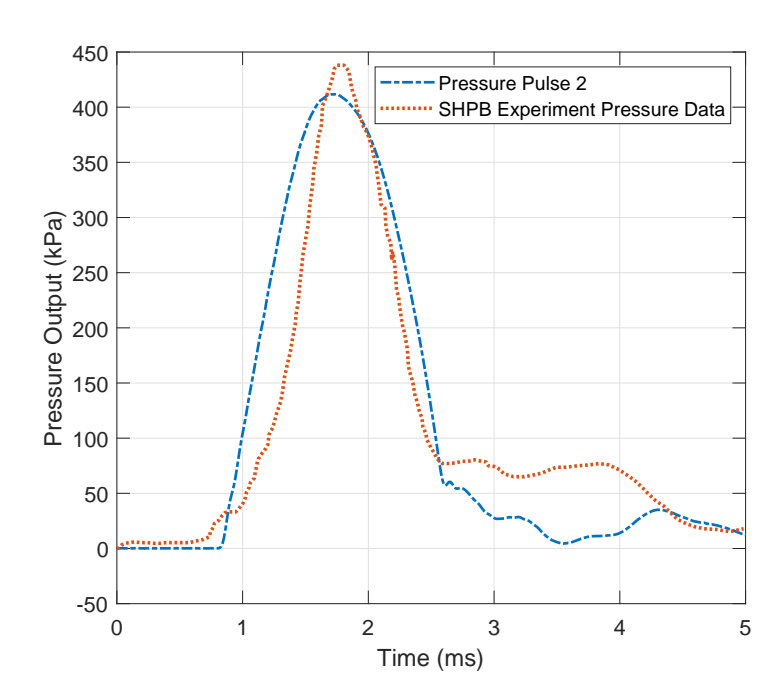


Figure 3.13: Comparison between the pressure pulse generated by our apparatus and the pressure profile obtained from SHPB experiment [8]

At the end of each excitation pulse, the input to the actuator was set to 0 V as shown in figure 3.12a. Thus, the excitation input to the actuator was stopped, allowing the actuator to discharge. The actuator and the piston were allowed to come to rest on their own. Part of the pressure profiles, since the actuation was stopped, shows this transient response of the apparatus and eventually pressure decays to zero as seen in figure 3.12b. The amplitude of this transient pressure was always found to be less than 10% percent of the pressure amplitude during the loading cycle.

3.4.2 Friedlander Waveform

A Friedlander waveform consists of an instantaneous rise in pressure followed by an exponential decay and lastly, a negative pressure phase [16]. The time duration for which the pressure is above the atmospheric pressure is known as the positive phase duration of the waveform. As an illustration, a Friedlander waveform having a maximum pressure of $450\,\mathrm{kPa}$ and positive phase duration of $10\,\mathrm{ms}$ is shown in figure 3.14. In order to generate a Friedlander waveform, the input voltage signal was constructed to have a sharp rise followed by an exponential decay. The negative phase feature of the Friedlander waveform was not incorporated in the input voltage signal because of the actuator limitation that it could only be operated within a $0-10\,\mathrm{V}$ range to generate compression, not tension. The input voltage signal starts with an instantaneous rise to the top voltage, followed by a hold time of 1 ms, and an exponential decay that lasts $10\,\mathrm{ms}$. This input excitation and the resulting output pressure profiles are shown in figure 3.15. The two pressure profiles were obtained when the same input voltage profile was fed to the actuator. These two pressure profiles replicate each other very closely, confirming the repeatability of the apparatus.

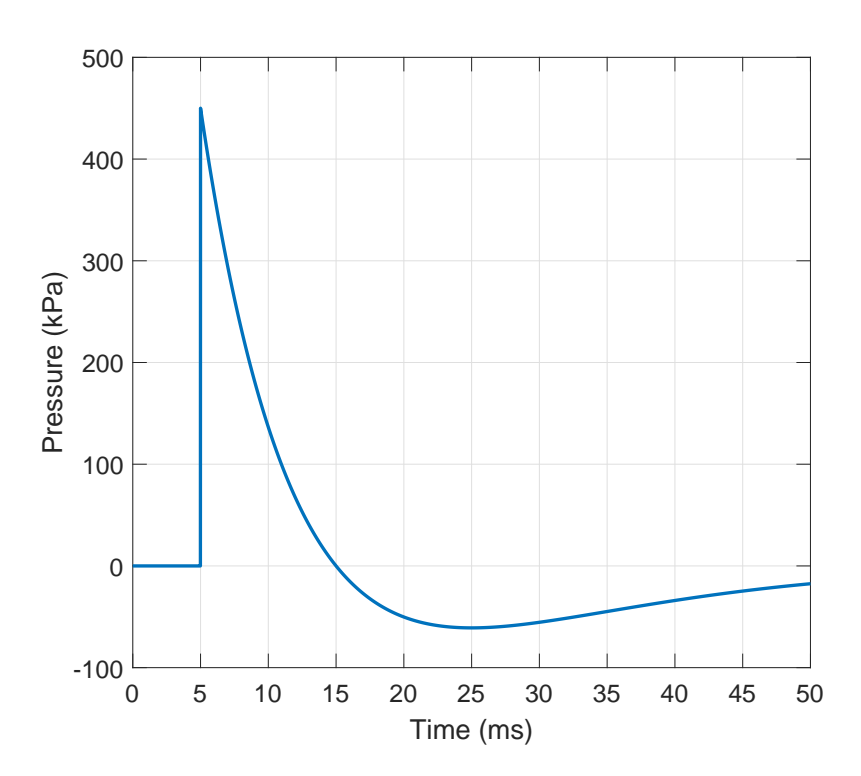


Figure 3.14: A Friedlander waveform with 450 kPa maximum pressure and 10 ms positive phase duration

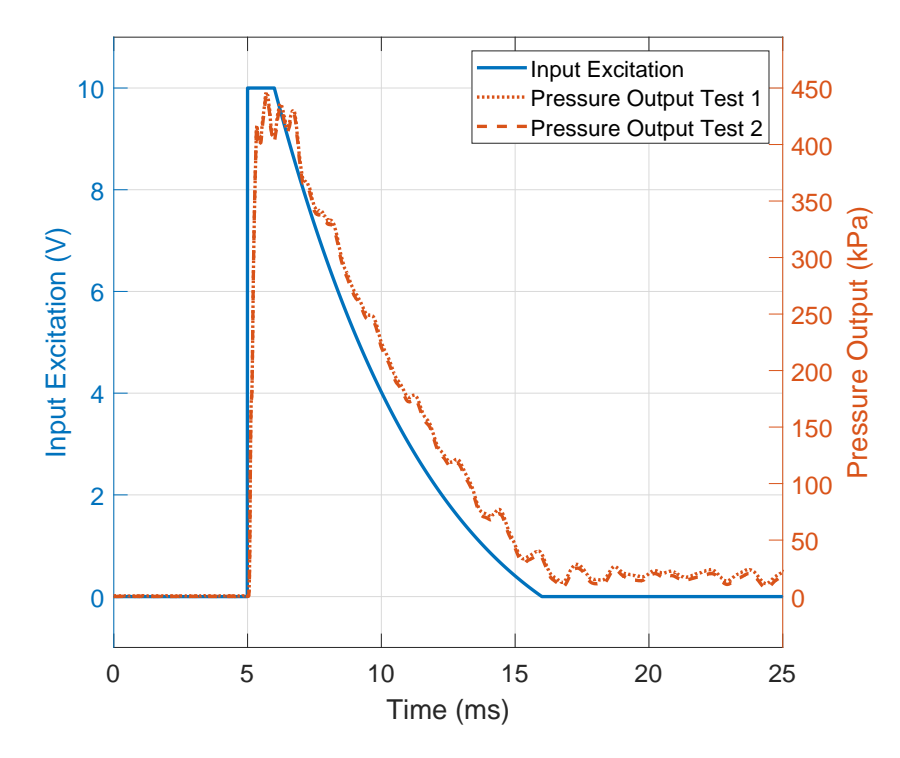


Figure 3.15: Comparison between a Friedlander like input excitation waveform given to the apparatus (left y-axis) and the output pressure profiles (right y-axis) generated by the apparatus

Even though the input excitation can have an instantaneous rise, the response time of the system is finite. The response time of the system depends primarily on the operational frequency-bandwidth of the piezoelectric actuator. If the input pulse had a sharp peak like a Friedlander wave, instead of the flat-top shown in figure 3.15, the system would not have had enough time to respond and would not have generated a pressure peak.

After this initial characterization, we determined that the maximum pressure that could be generated with the current implementation of our apparatus is 450 kPa, which is limited by the geometry of the confinement and the maximum displacement range of the piezoelectric actuator. The maximum operating frequency of this particular actuator is 5 kHz, which also imposes limits to the shortest rise time for pressure generation and high-frequency spectral components of the loading cycle.

3.4.3 Multi-modal Waveform

The implementation of the feedforward controller was demonstrated by solving the output tracking problem for a multi-modal target output profile. As a test case, a multi-modal pressure profile was constructed by adding three sine waves of frequencies 500 Hz, 1000 Hz, and 2000 Hz. The amplitudes and the phases of the sinusoids used to construct the target pressure profile are detailed in table 3.4. Also, offsets equal to the amplitudes of sinusoids were added to make the target profile non-negative. The multi-modal target pressure profile constructed for the output tracking problem is shown in figure 3.16.

Table 3.4: Sinusoidal components of multi-modal target pressure profile

Frequency (Hz)	Amplitude (kPa)	Phase (rad)	Offset (kPa)
500	75	1.5π	75
1000	75	1.5π	75
2000	75	1.5π	75

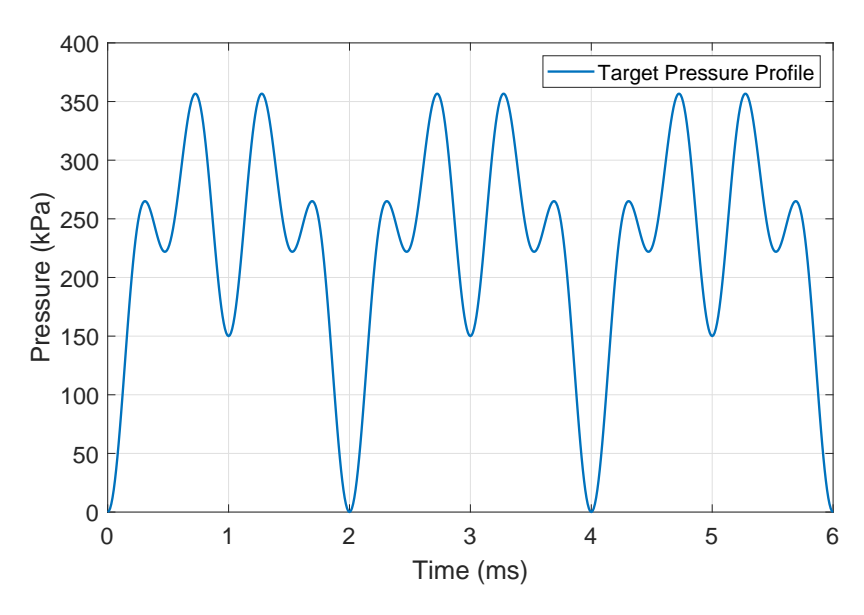


Figure 3.16: Multi-modal target pressure profile constructed for an output tracking problem

The designed feedforward controller was used to determine the control input profile. The

control input profile generated by the controller for this output tracking problem is shown in figure 3.17. It is noticeable that the control input profile exhibits the amplitude and phase modulation characteristics of the system. This control input profile was then fed to the amplifier that powered the piezoelectric actuator. The output pressure profile generated by the apparatus in response to the control input profile was recorded. This experiment was repeated twice and the measured pressure profiles for both the experiments are shown in figure 3.18 along with the target pressure profile.

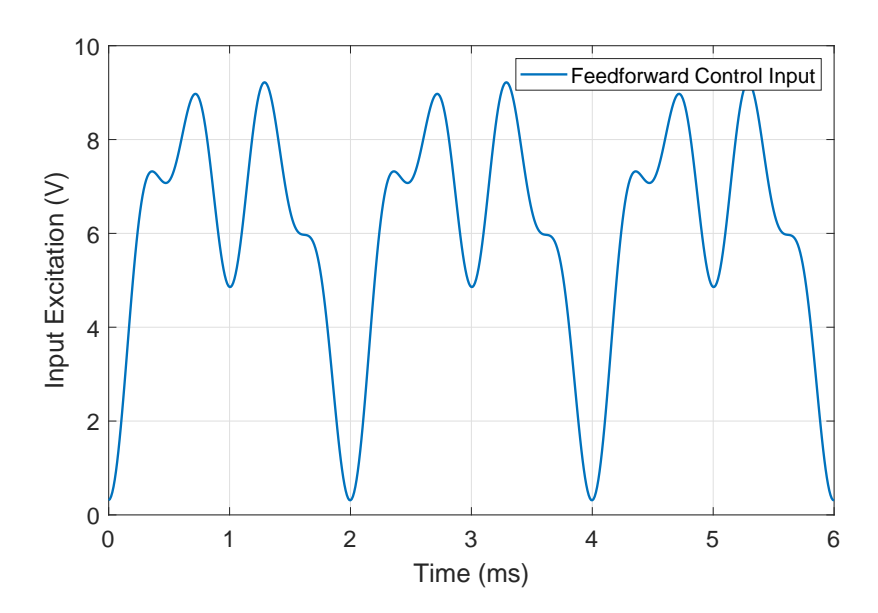


Figure 3.17: Control input profile determined by the feedforward controller

The experimental pressure profiles were found to be in close agreement with the target pressure profile. The two experimental pressure profiles were almost identical, indicating the repeatability of the experimental results. The experimental pressure profiles provided an over 96% fit to the target pressure profile based on the normalized mean squared error (NMSE) calculation. Thus, this proposed feedforward control strategy can be used to fairly track a complex pressure profile composed of the sinusoids having frequencies between 100 Hz to 5 kHz.

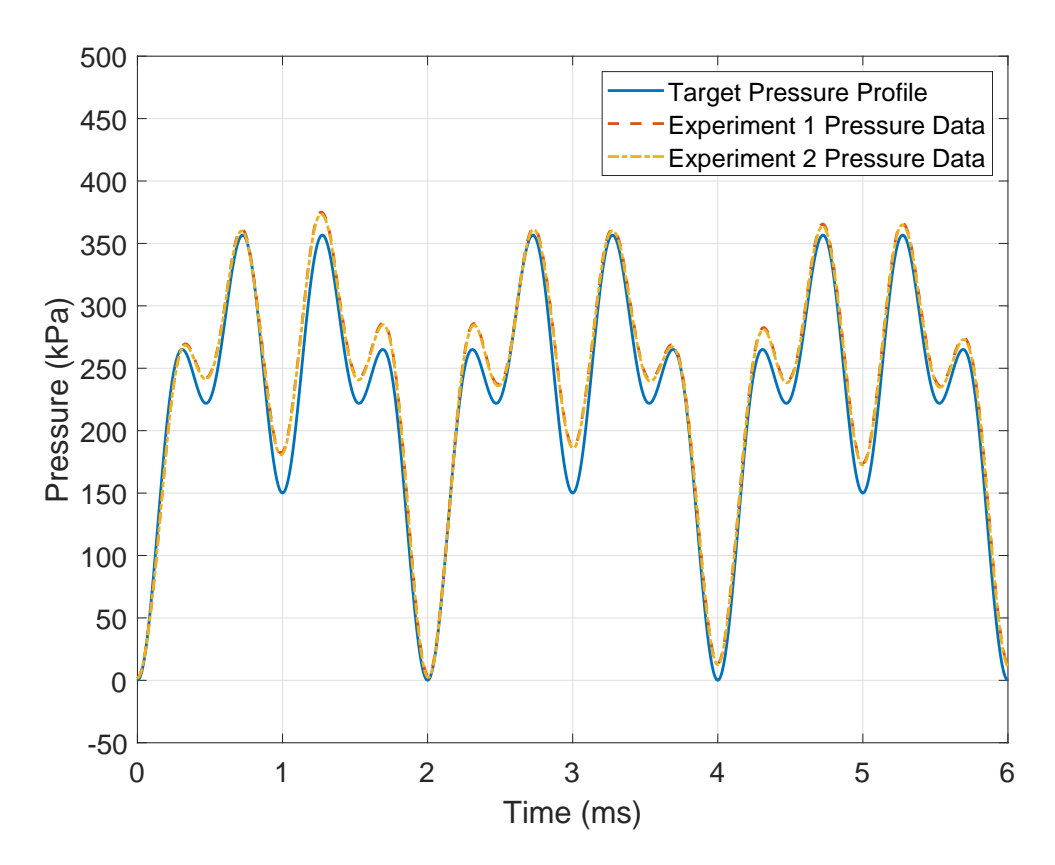


Figure 3.18: Comparison between the target pressure profile and the experimental pressure profiles obtained using the feedforward controller

3.5 Conclusion and Discussion

An experimental apparatus was designed to generate complex pressure profiles by using a piston-cylinder assembly filled with water. A piezoelectric actuator was used to displace the piston. The displacement of the piston driven by the actuator was controlled through the voltage excitation input given to the actuator. This displaced piston further compressed the water inside the cylinder that generated pressure profiles replicating the dynamics of the input voltage excitation profiles. To test the capabilities of the apparatus, the piezoelectric actuator was excited with various input voltage profiles that included single sinusoidal pulses and a Friedlander-like waveform. The pressure profiles obtained for these input excitation profiles followed the temporal and magnitude characteristics of their respective input pro-

files. Moreover, a feedforward controller was designed and implemented, which enabled the apparatus to generate complex user-defined pressure profiles.

Split-Hopkinson Pressure Bars, shock-tubes, and blast-tubes are relatively complex systems with inherent hazards such as high pressure, shock, impact, and loud noise. In consequence, their safe operation requires rigorous technical training. Also, they lack portability due to their typically large footprint ($\sim 10\,\mathrm{m}^2$ or more) and anchoring requirements (e.g., vibration isolation); and are in general not tunable in the sense that their ability to produce arbitrary loading cycles is very limited. Our apparatus overcomes all of these limitations due to its very small footprint ($\sim 4 \times 10^{-2}\,\mathrm{m}^2$), no special anchoring requirements, no inherent safety concerns, technical simplicity, and its ability to produce virtually any arbitrary loading cycle within its pressure and frequency bounds. In addition, our apparatus fits inside any fume hood due to its compactness, increasing its suitability for biomedical applications. Depending on the choice of piezoelectric actuator, an apparatus like the one presented herein is suitable for applications that require resonant frequencies in the range $5\,\mathrm{kHz} - 16\,\mathrm{kHz}$, and peak pressures of up to $450\,\mathrm{kPa}$.

Typical ex-vivo and in-vitro experiments on living tissue, organoids, or cell cultures are performed in nearly incompressible media such as artificial cerebrospinal fluid or other aqueous solutions [8,32,35,92], enabling our apparatus for studies of the effect of dynamical loading on these kinds of biological systems.

The inner diameter of the pressure chamber is based on the diameter of the piezoelectric actuator (11.2 mm). Its inner volume was optimized for the operational characteristics of the piezoelectric actuator. In principle, the inner diameter of the confinement could be increased, but it would require some additional design optimization beyond just a change in scale to offer similar operational characteristics as with the basic design. The same idea goes

for any attempt to increase the maximum pressure, or the maximum achievable frequency: the resonant frequency, stroke, and maximum force of the piezoelectric actuator define the limitations to each new design.

The current implementation of this apparatus does not include volumetric expansion of the confinement chamber, limiting its operation to positive gauge pressures. With the intention to expand our studies to the effect of cavitation [26,29,30,36,37], we have developed a rig that includes the ability to exert volumetric expansions and generate cavitation. The design of this new rig is discussed in the next chapter.

Chapter 4

Bench-top Rig for

Controlled-Cavitation Experiments

4.1 Introduction

Cavitation phenomenon is observed when a liquid is subjected to a tensile or negative pressure higher than a threshold, i.e., the liquid's vapor pressure at that temperature [22]. Cavitation encompasses the formation, growth, and collapse of the bubbles caused by the rapid changes in pressure [23]. The collapse of the cavitation bubbles generates high-pressure shock-waves that can be damaging to the components in the vicinity of the bubbles [24–26].

Impact forces experienced by the human head are hypothesized to cause cavitation in cerebrospinal fluid (CSF), which could be damaging to the surrounding brain tissue [7,13,21]. The impact forces can arise because of a sudden impact to the head during sports such as football, boxing, etc., or an automotive accident, or a blast exposure [36,37,93,94]. A person exposed to such events could sustain a traumatic brain injury (TBI).

To explore the TBI mechanisms associated with cavitation, we have developed a benchtop apparatus that can generate controlled cavitation in liquids. This apparatus can be used to expose living brain tissue or cell culture specimens to a cavitation event in a controlled laboratory setting. Evaluating the biological response of such specimens could provide insight into TBI injury mechanisms.

The presented apparatus is inexpensive, compact, portable, and highly-controllable compared to other experimental techniques used to generate cavitation. The apparatus uses a high-speed linear motor to generate negative pressures in a cylindrical cavity, a pressure transducer to measure the pressure profiles, and a control system consisting of a servo drive and data acquisition hardware to generate a user-defined characteristic for the cavitation event.

This chapter is organized as follows. Section 4.2 discusses the working principle and the fabricated design of the cavitation apparatus. The experiment conducted to produce cavitation in water, and its results are discussed in section 4.3. Lastly, section 4.4 concludes the discussion on the cavitation apparatus.

4.2 Design

4.2.1 Working Principle

In this study, a piston-cylinder assembly filled with water (shown in figure 4.1) was used as variable-volume confinement for generating negative pressure and induce cavitation. Water has a very high bulk modulus of 2.15 GPa [83]; hence, its pressure changes sharply as a response to relatively small volume changes.

The change in pressure inside the cylinder, ΔP , can be estimated using the Hooke's law for volumetric loading [82,88] given by the equation,

$$\Delta P = -K \frac{\Delta V}{V_0},\tag{4.1}$$

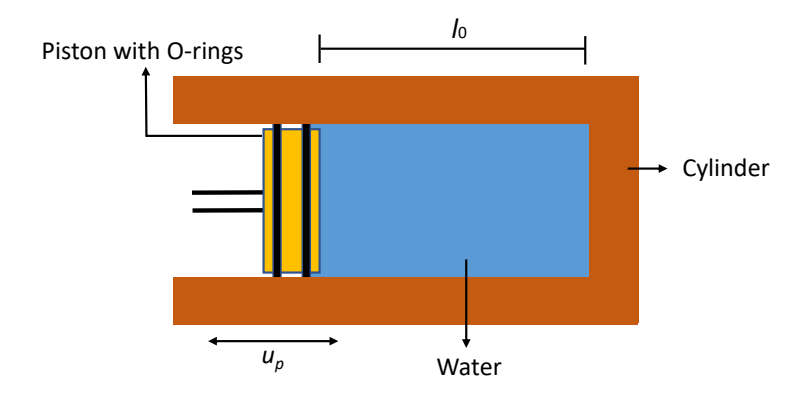


Figure 4.1: A piston-cylinder assembly filled with water (l_0 : initial length of the water volume inside the cylinder, u_p : displacement of the piston)

where K is the bulk modulus for water, V_0 is the initial volume of water inside the cylinder, and ΔV denotes the change in volume of water. Assuming the cylinder walls to be perfectly rigid and the cylinder having a uniform cross-section, equation (4.2) can be further simplified to

$$\Delta P = K \frac{u_p}{l_0}. (4.2)$$

Here, l_0 and u_p denote the initial length of the water volume inside the cylinder and the piston's displacement, respectively, as shown in figure 4.1. As a sign convention, the compressive displacement of the piston is considered positive. Since the bulk modulus of water is extremely high, even a sub-millimeter piston retraction can generate high negative pressures, enough to induce cavitation in water. Equations (4.1) and (4.2) are valid only until the negative pressure reaches the cavitation threshold pressure. Any piston retraction beyond this threshold would just result in the expansion of the bubbles without any further decrease in the pressure. Here, the piston speed ($\approx 1 \text{ m/s}$) is several orders of magnitude smaller than the longitudinal wave speed in water ($\approx 1500 \text{ m/s}$). Thus, the transient wave propagation effects can be neglected, and the pressure changes can be directly linked to the piston displacement as stated in equation (4.2). Consequently, the pressure field is uniform

throughout the cylinder, and it is measured using the pressure transducer.

A linear motor (Model PS01-37x120F-HP-C LinMot USA Inc.) is used to displace the piston of the piston-cylinder assembly as shown in figure 4.2. The linear motor is used to retract the piston from the cylinder, increasing the volume of the cylindrical cavity and decreasing the pressure as a result. The time scale of this actuation is of the order of a few milliseconds; this is fast enough to generate negative pressure loadings similar to those of a blast or a blunt TBI event [36]. A high-frequency pressure transducer (Model 113B27 PCB Piezotronics Inc.) measures the pressure inside the cylinder to give feedback about the generated negative pressure and the cavitation phenomenon.

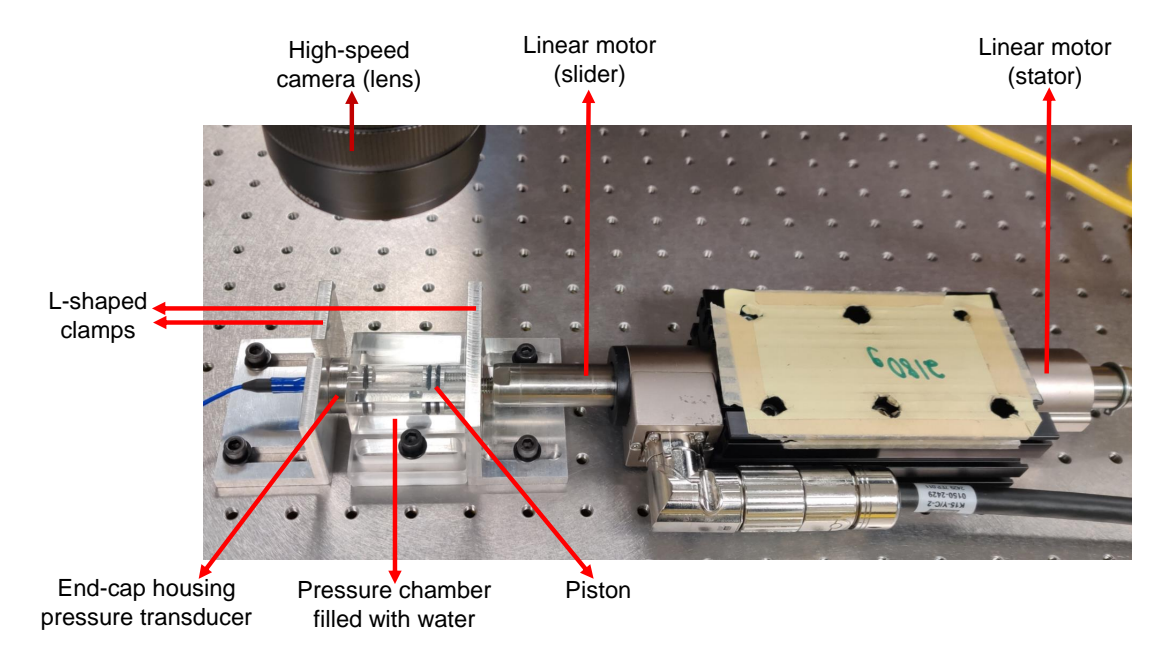


Figure 4.2: Experimental setup of the cavitation apparatus

4.2.2 Device Fabrication

The pressure chamber was machined from an acrylic block by drilling a through-hole of 13.1 mm diameter. A custom end-cap was designed and machined from a medical-grade SAE 316L stainless-steel rod (25.4 mm diameter) to hold the pressure transducer as well as

seal one end of the chamber using an O-ring. The other end of the chamber was sealed using an aluminum piston with O-rings. A venting channel, which is a 1.6 mm diameter hole drilled perpendicular to the pressure chamber axis, was incorporated in the pressure chamber to remove air bubbles and excess water while filling the chamber. The design of the venting channel is similar to the one implemented in [30]. The piston was connected to the slider of the linear motor using a threaded rod (M8×1.25 threads). The fabricated design of the apparatus is shown in figure 4.2. Two custom-machined L-shaped clamps were used to prevent the motion of the pressure chamber. The entire assembly was bolted down to an optical table.

4.2.3 Instrumentation and Control

The input to the apparatus was a displacement profile specified for the slider. A power supply unit (Model S01-72/500 LinMot USA Inc.) was used to power the linear motor along with a servo drive (Model C1250-LU-XC-0S-000 LinMot USA Inc.). The servo drive was used to control the slider's displacement using the pre-configured proportional-integral-derivative (PID) controller [95]. The gains of the PID controller were tuned for the optimal tracking of the displacement profile. The slider's motion determined the displacement of the piston and altered the pressure in the chamber, which was measured using the pressure transducer. A signal conditioner (Model 482A21 PCB Piezotronics, Inc.) was used to amplify the pressure signal measured by the transducer, which was finally recorded using a data acquisition device (Model USB-6341 National Instruments) at a sampling frequency of 100 kHz. A high-speed camera (Model Phantom V2512) was also added to the system to record the cavitation events at 75 k frames per second. Lastly, a 5 V transistor-transistor logic (TTL) trigger pulse was used to synchronize the actuation of the linear motor with the acquisition of pressure and

high-speed imaging data.

4.3 Results and Discussion

To assess the capabilities and the performance of the apparatus, an experiment was conducted to expose water to negative pressures and analyze the cavitation phenomenon. In order to generate the negative pressures in the piston-cylinder assembly, the piston was retracted as per the specified displacement profile. A sinusoidal half-wavelength pulse with an amplitude of 5 mm, and pulse-width of 10 ms was specified as a target displacement profile for the piston. The target displacement profile is shown in figure 4.3 along with the measured displacement of the piston and the force applied by the motor to generate the piston displacement.

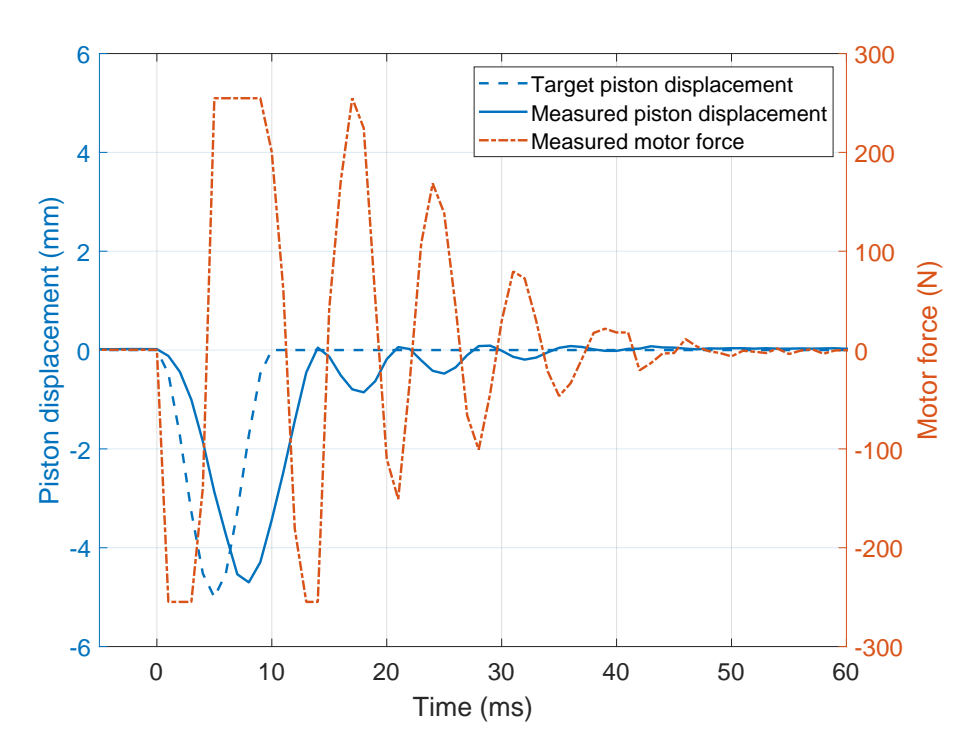


Figure 4.3: Comparison between the target piston displacement profile and the measured piston displacement profile for the cavitation experiment (left y-axis). The force applied by the motor to achieve the target piston displacement is also shown (right y-axis).

It can be observed that the motor force magnitude saturated at 255 N, which was the maximum force that the motor could generate. This force constraint downgraded the PID controller's performance and limited tracking of the target displacement profile. However, the measured displacement profile had a similar magnitude and timescale compared to the target profile. Also, additional oscillations were observed in the measured displacement profile compared to that of the target profile. The motor force saturation and the sharp pressure variations due to the cavitation phenomenon have contributed to the additional oscillations observed in the measured displacement profile.

The displacement of the piston affected the pressure inside the cylinder. This pressure was measured using the pressure transducer placed at the other end of the cylinder. The pressure profile measured by the transducer is shown in figure 4.4 along with the displacement of the piston. Some of the key instances for the cavitation event are highlighted on the pressure profile, and the corresponding snapshots of the pressure chamber are shown in figure 4.5.

It is evident from figure 4.4, as the piston was retracted, the pressure inside the cylinder rapidly decreased and saturated at -110 kPa. The effect of this negative pressure on the micro-bubbles present inside the chamber can be seen in figure 4.5 (snapshots A and B). As the piston was retracted further, there wasn't any significant change in pressure. However, the additional retraction of the piston resulted in the further expansion of the bubbles, which can be seen in figure 4.5 (snapshots C, D, and E). The bubbles reached their maximum size when the piston was at the fully retracted position. As the piston started to return, the pressure inside the chamber started to increase. This rise in the pressure resulted in the collapse of the bubbles, which can be seen in figure 4.5 (snapshots F and G). The collapse of the bubbles suddenly released all the stored energy in the form of shock-waves. The presence of the shock-waves was confirmed from both the pressure and high-speed imaging

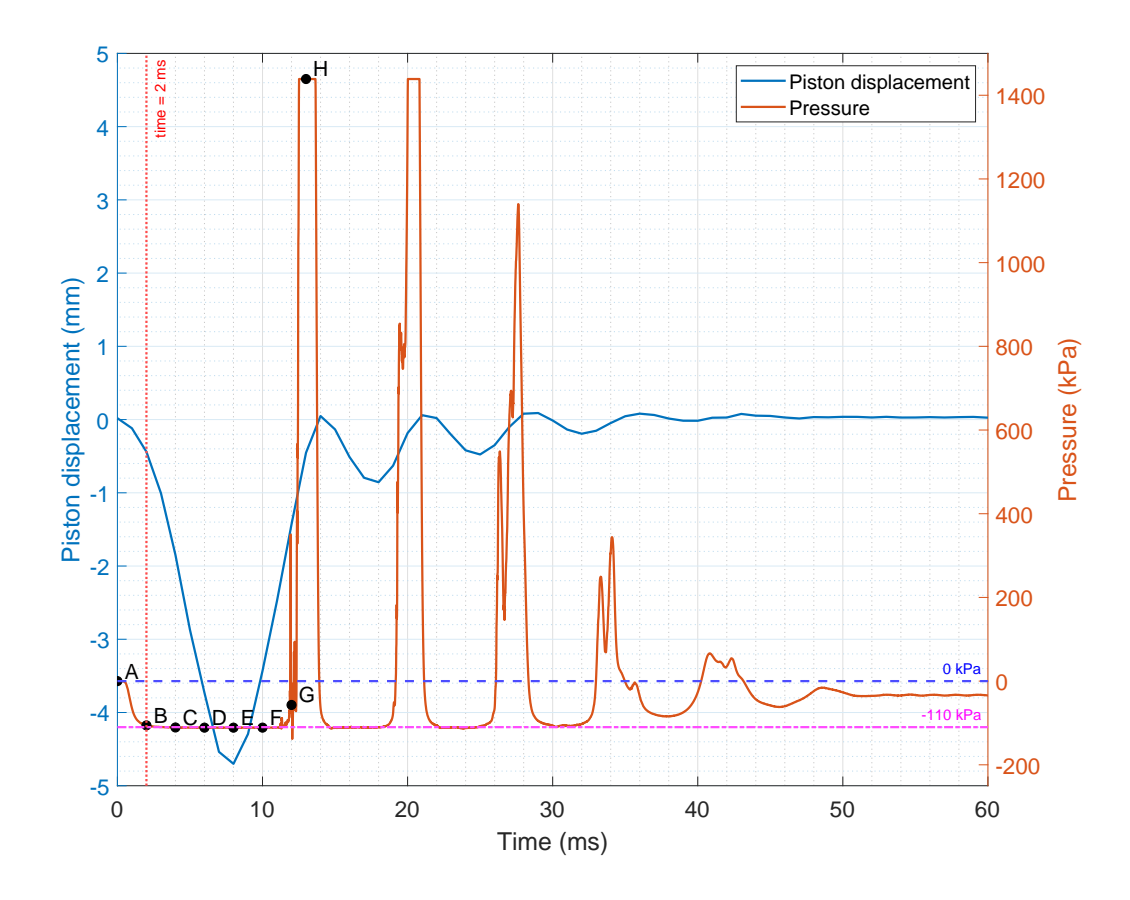


Figure 4.4: Displacement of the piston (left y-axis) and the resulting pressure profile generated inside the chamber (right y-axis). Some of the key instances of the cavitation event are highlighted on the pressure profile. The corresponding high-speed images of the pressure chamber are shown in figure 4.5.

data. The shock-waves generated from the collapse of the bubbles sharply increased the pressure inside the cylinder. This high-pressure exceeded the rated measurement range of the pressure transducer, and thus, saturation was observed in the measured pressure profile. This high-pressure cleared all the bubbles from the pressure chamber, which is evident from 4.5 (snapshot H).

When the pressure inside the chamber saturated at -110 kPa for the first time (time = 2 ms in figure 4.4), the piston was at 0.4 mm retracted position. This implied, the piston displacement of only 0.4 mm was sufficient to generate the cavitation pressure. The subsequent

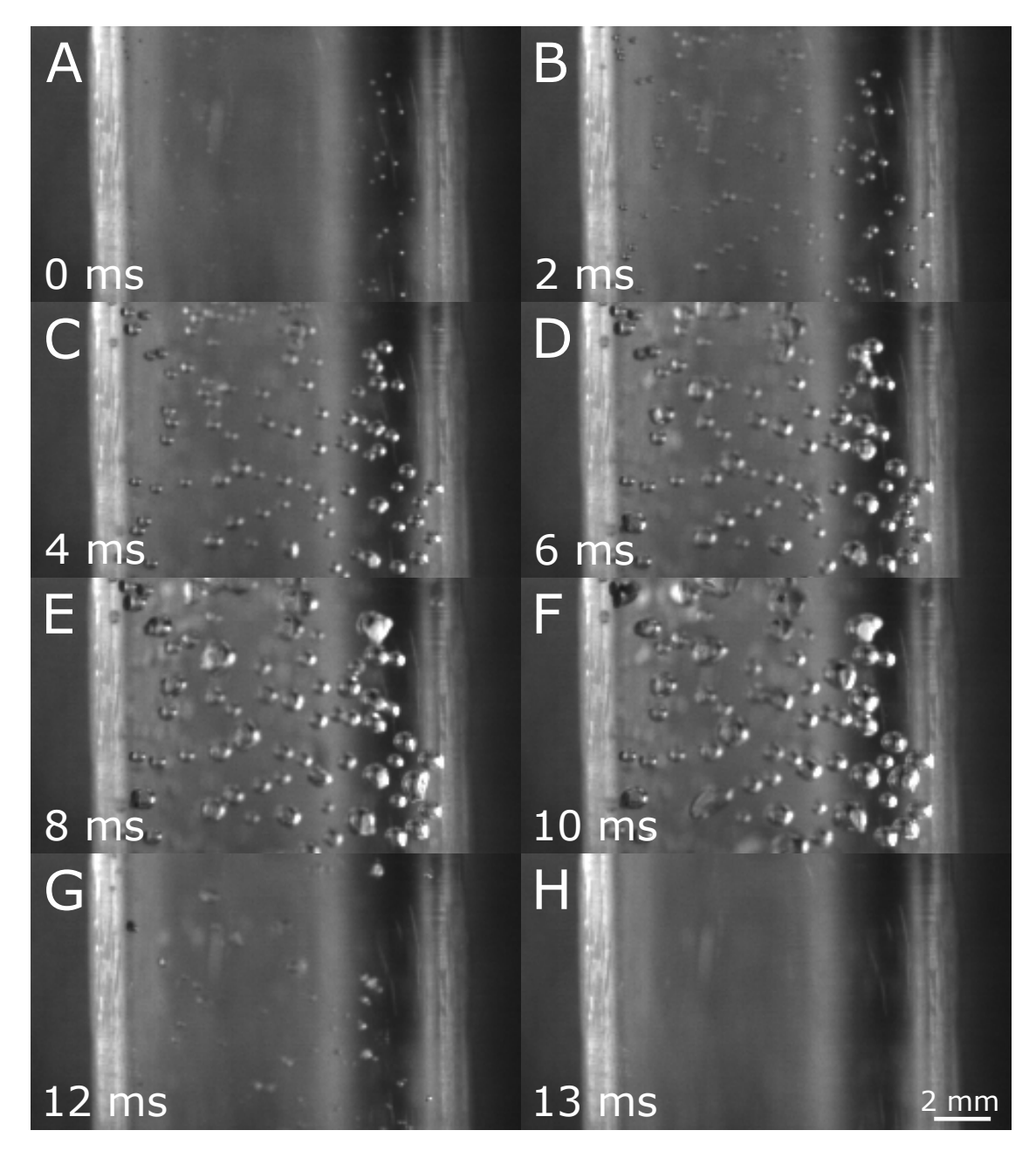


Figure 4.5: High-speed images of the pressure chamber showing the expansion and collapse of the cavitation bubbles. The pressure inside the chamber at the corresponding instances is highlighted on the pressure profile shown in figure 4.4.

oscillations observed in the piston displacement profile also crossed the 0.4 mm displacement threshold. Thus, these piston oscillations generated sufficient negative pressures, which repeated the cavitation bubble dynamics.

Few micro-bubbles were already present in the pressure chamber before the piston was

moved (can be seen in figure 4.5: snapshot A). The negative pressure loading generated by the apparatus expanded these existing micro-bubble rather than creating new cavitation bubbles in the water. Thus, if the focus is to generate new cavitation bubbles in a liquid, deliberate efforts are needed to remove all the pre-existing bubbles from the liquid. The methods that can be implemented to remove the pre-existing bubbles are detailed in [25, 26, 30].

The pressure sensor can only measure the pressure variations, and the steady-state pressure is always measured as zero pressure. This limitation of the pressure sensor does not allow us to measure the reference pressure, which is the pressure inside the chamber before any piston actuation. However, deliberate efforts were made to keep the reference pressure of the chamber close to the atmospheric pressure, i.e., the gauge pressure would be close to zero. For the cavitation event, it was observed that the negative pressure got saturated at -110 kPa. The vapor pressure for water at 25 °C is -98 kPa [96]. At the vapor pressure, the water vapor and water are in thermodynamic equilibrium [22]. Thus, during the cavitation event, it is expected to see the negative pressure saturate at the vapor pressure of water for that particular temperature. The difference in the measured saturation pressure and the vapor pressure could be because of the deviation of the reference pressure from the atmospheric pressure.

4.4 Conclusion

We have designed a bench-top apparatus that can generate negative pressures and induce cavitation in liquids. This apparatus uses a piston-cylinder assembly that would be filled with the liquid of interest. A linear motor is used to displace the piston. A PID controller is further used to control the motor and displace the piston as per the user-specified displacement profile. The retraction of the piston increases the volume of the pressure chamber cavity and generates tensile or negative pressures. As the negative pressure crosses a cavitation threshold pressure, it induces cavitation in the liquid present in the pressure chamber. This apparatus was tested by inducing cavitation in water.

Experimental techniques, such as split Hopkinson pressure bars, shock-tubes, blast-tubes, drop-towers, etc., currently used to generate negative pressures and study cavitation, are relatively complex and require rigorous technical training for safe operation. Moreover, these experimental systems are incredibly bulky and thus, lack portability. Our apparatus overcomes all of these limitations due to its very small footprint and technical simplicity. Additionally, the pressure profiles generated by our apparatus can be easily tuned based on the required characteristics of the cavitation events.

The typical pressure profiles generated by the split Hopkinson pressure bars, shock-tubes, and blast-tubes follow a Friedlander waveform, which has a large positive pressure peak followed by a negative pressure phase. It is this negative pressure phase that induces cavitation. However, the pressure profile generated by our apparatus can be controlled to exclusively include the negative pressure phase without the initial large positive pressure peak. This feature allows us to load specimens with negative pressure cycles without exposing them to initial high positive pressure, which is particularly helpful to decouple and isolate the damage mechanisms associated with cavitation. The shock-waves arising from the collapse of the cavitation bubbles also generate a high-pressure, but its magnitude and time-scale significantly differ from the initial Friedlander-like pressure peak.

Chapter 5

Generator of Dynamic Shear Cycles

5.1 Introduction

This chapter introduces the apparatus for generating dynamic shear loading cycles. The principal idea constituting this apparatus is to use a voice-coil actuator [97] and two parallel plates assembly to generate shear loadings.

This chapter is organized as follows. Section 5.2 discusses the first design iteration of the shear apparatus. This section details the working principle, fabricated design, and performance characterization of the shear apparatus. The feedforward controlled for the shear apparatus is also described in this section. The limitations of the first-iteration shear apparatus necessitated a second design iteration. The second design iteration of the shear apparatus is discussed in section 5.3. The preliminary experiments conducted to determine the mechanical properties of polyacrylamide (PAA) gelatin specimens, as well as to test the implementation of the apparatus for loading samples of living tissue and three-dimensional cell cultures, are discussed in section 5.4. Lastly, section 5.5 concludes the discussion on the shear apparatus.

5.2 Design Iteration I

5.2.1 Working Principle

The shear apparatus consists of two parallel plates with the specimen sandwiched between these plates. The top plate is connected to a voice-coil actuator (Model NCM02-05-005-4JBMCS, H2W Technologies). Thus, the movement of the top plate is set by controlling the motion of the voice-coil actuator. A laser-based displacement sensor (Model LK-H057, Keyence Corporation) is used to measure the displacement of the top plate. By measuring the displacement of the top plate, the shear strain (γ) is calculated using the equation,

$$\gamma = \frac{u_{tp}}{d} \,, \tag{5.1}$$

where u_{tp} denotes the displacement of the top plate and d denotes the specimen thickness. The bottom plate is attached to a load cell (MDB2.5, Transducer Techniques) that measures the force (F) needed to keep the plate fixed. The shear stress (τ) experienced by the specimen is determined using the equation,

$$\tau = \frac{F}{A} \,, \tag{5.2}$$

where A denotes the contact area between the specimen and the bottom plate. The schematic of the experimental apparatus is shown in figure 5.1.

The voice-coil actuator generates a displacement of few millimeters at oscillating frequencies up to $100\,\mathrm{Hz}$. Thus, by controlling the displacement of the voice-coil actuator, dynamic shear strains of variable magnitudes and frequencies can be induced to the specimen. Strain rates up to $100\,\mathrm{s}^{-1}$ can be achieved using this apparatus. The mechanical properties of the specimen can be determined by correlating shear stress and strain data obtained under

various dynamic loading conditions.

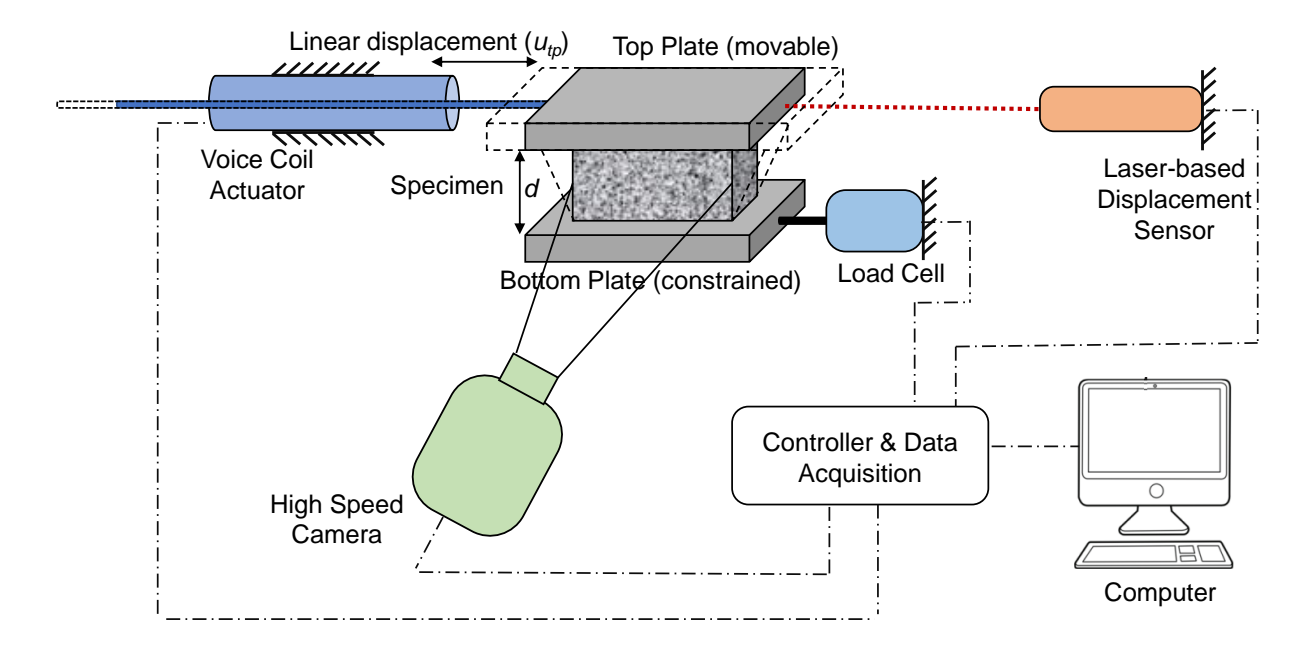


Figure 5.1: Schematic of the shear apparatus (Design iteration I)

5.2.2 Device Fabrication

Each of the parallel plates consisted of two parts: a base plate and a specimen holder plate. For the top plate, the base plate was attached to the voice-coil actuator using a set screw, and for the bottom plate, the base plate was attached to the load cell. Slots were incorporated in the base plates to house the specimen holder plates. This two-part design of the parallel plates facilitated the easy placement and removal of the specimen from the apparatus. The base plates were 3D-printed out of VeroWhite resin, and the specimen holder plates were 3D-printed out of PLA filament. A custom holder was designed and 3D-printed out of PLA to rigidly mount the voice-coil actuator to a support fixture. The support fixture was built from T-slotted aluminum rods (80/20 Inc.). The completed setup of the shear apparatus is shown in figure 5.2.

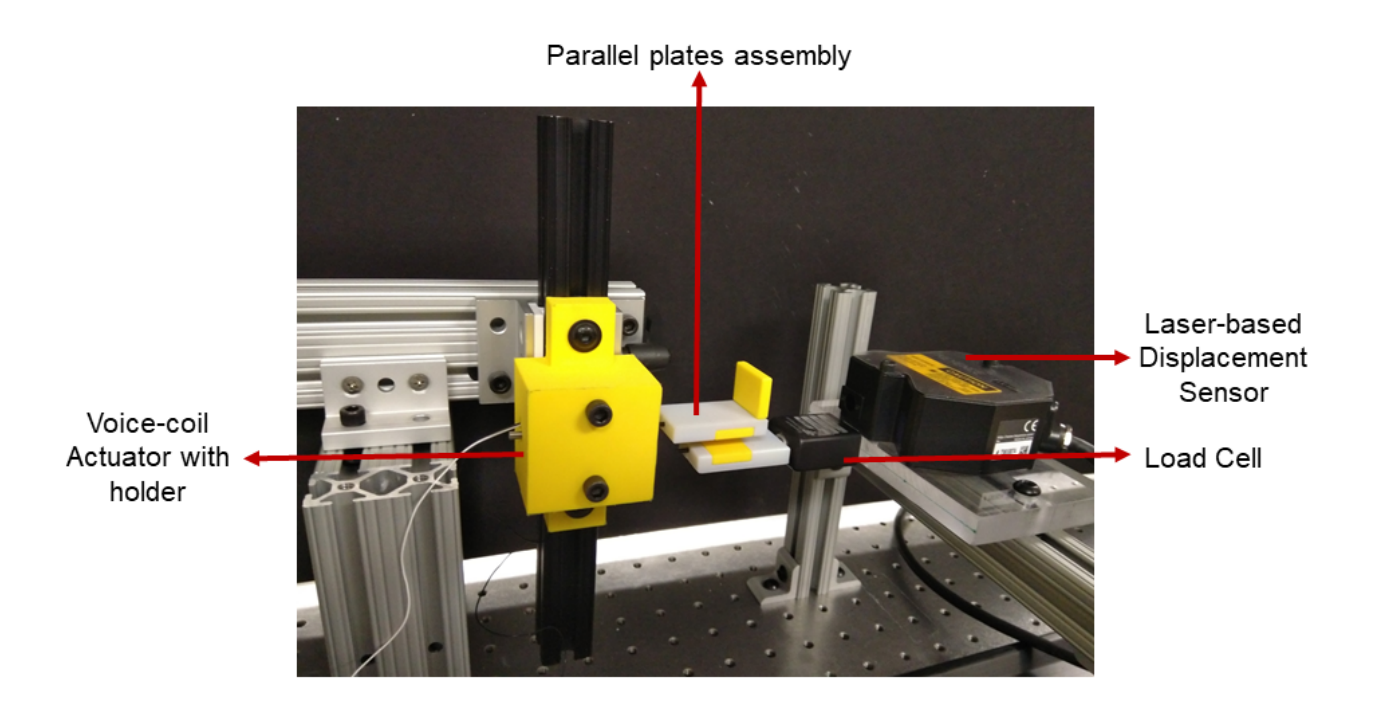


Figure 5.2: Fabricated setup of the shear apparatus (Design iteration I)

5.2.3 Instrumentation

The input to the apparatus was a -10 to 10 V voltage signal. Based on the input voltage signal, a proportional -3 to 3 A current signal was generated by a power amplifier (Model LCAM 5/15, H2W Technologies). Then it was fed to the voice-coil actuator. The input voltage signal determined the force generated by the voice-coil actuator, which moved the top plate. The top plate's displacement was measured using the laser-based displacement sensor, which was driven by a controller (Model LK-G5001P, Keyence Corporation). The load cell was used along with a signal conditioner (Model NI9237, National Instruments) to measure the shear force acting on the bottom plate. A data acquisition device (Model cDAQ9178 with NI9215 and NI9263, National Instruments) was used to generate the control input voltage signal and acquire the displacement and force measurement signals. A custom LabVIEW (National Instruments) program was developed to perform and synchronize both

the signal generation and the data acquisition tasks at the sampling frequency of 10 k samples per second. A high-speed camera (Model Phantom V2512) was also used to capture the deformation of specimens at 10 k frames per second.

5.2.4 Performance Characterization

The performance of the apparatus was characterized by loading a PAA gelatin specimen under dynamic shear cycles and calculating the shear strain field from the high-speed images. These shear strain field measurements were then compared to the shear strain calculated from the top plate displacement data.

The mechanical properties of these gelatin specimens can be tailored to mimic different regions of the brain tissue e.g., white and gray matter by varying the weight concentrations of PAA [98–100]. For these experiments, a cuboidal specimen of size $19\,\mathrm{mm} \times 19\,\mathrm{mm} \times 6.5\,\mathrm{mm}$ was molded from PAA gel having $10\,\%$ weight concentration. The PAA gel specimen is shown in figure 5.3. The main reason for using PAA gelating was its easily tunable material

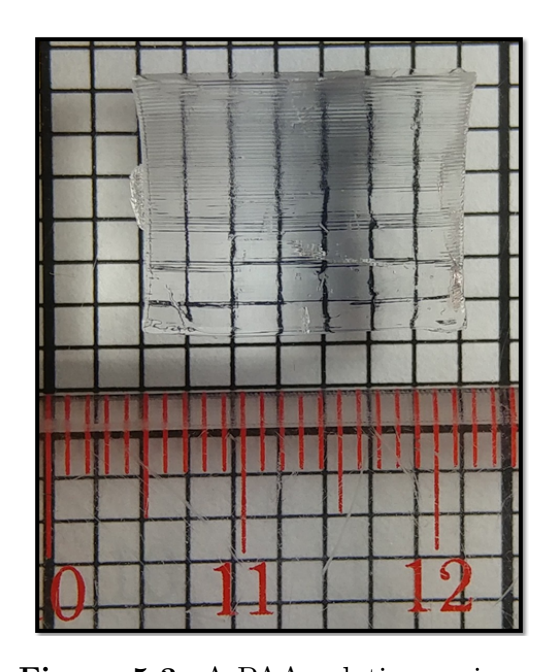


Figure 5.3: A PAA gelatin specimen

properties which could be achieved by varying concentrations of the base acrylic monomers. Moreover, the PAA gel fabrication is fast, has low energy requirements, and can be done at room temperature. The fabrication technique detailed in [101] was followed to make the PAA gelatin specimens.

A sinusoidal voltage signal of 20 Hz frequency was given as input signal to the power amplifier, which powered the voice-coil actuator with a sinusoidal current signal of amplitude 1 A and frequency 20 Hz. The actuator was powered for 10 cycles lasting over 500 ms. The current profile fed to the actuator is shown in figure 5.4.

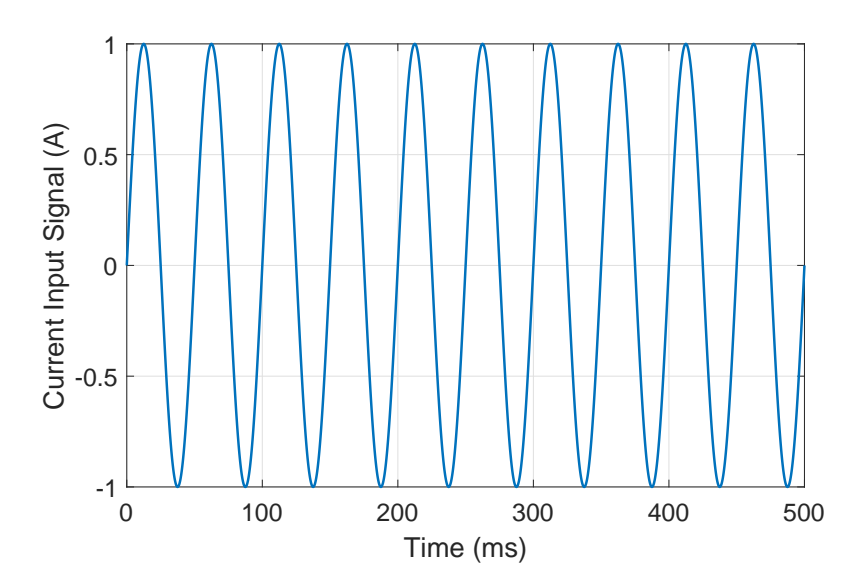


Figure 5.4: Current profile given as an excitation input to the voice-coil actuator

The PAA gelatin specimen was sandwiched between the parallel plates and glued to the specimen holder plates. Sand particles having a size less than $125\,\mu\mathrm{m}$ were attached to the surface of the gelatin specimen. Once the voice-coil was actuated, it moved the top plate, whereas the bottom plate was stationary. The PAA gelatin specimen was sheared between the plates for 10 cycles at 20 Hz frequency. The deformation of the specimen was quantified by tracking the groups of sand particles in the acquired high-speed images. The particle

image velocimetry (PIV) technique was used to track the groups of sand particles. The PIV technique tracks a group of particles by cross-correlating consecutive images and computing the displacement field [102].

The sequence of images representing the initial half of the first shearing cycle is shown in figure 5.5. The raw images ($1280 \times 800 \,\mathrm{pixels}$) acquired from the high-speed camera had a spatial resolution of 40.33 pixels/mm. These images were cropped for the region of interest ($541 \times 230 \,\mathrm{pixels}$), and were pre-processed with histogram equalization operation [103].

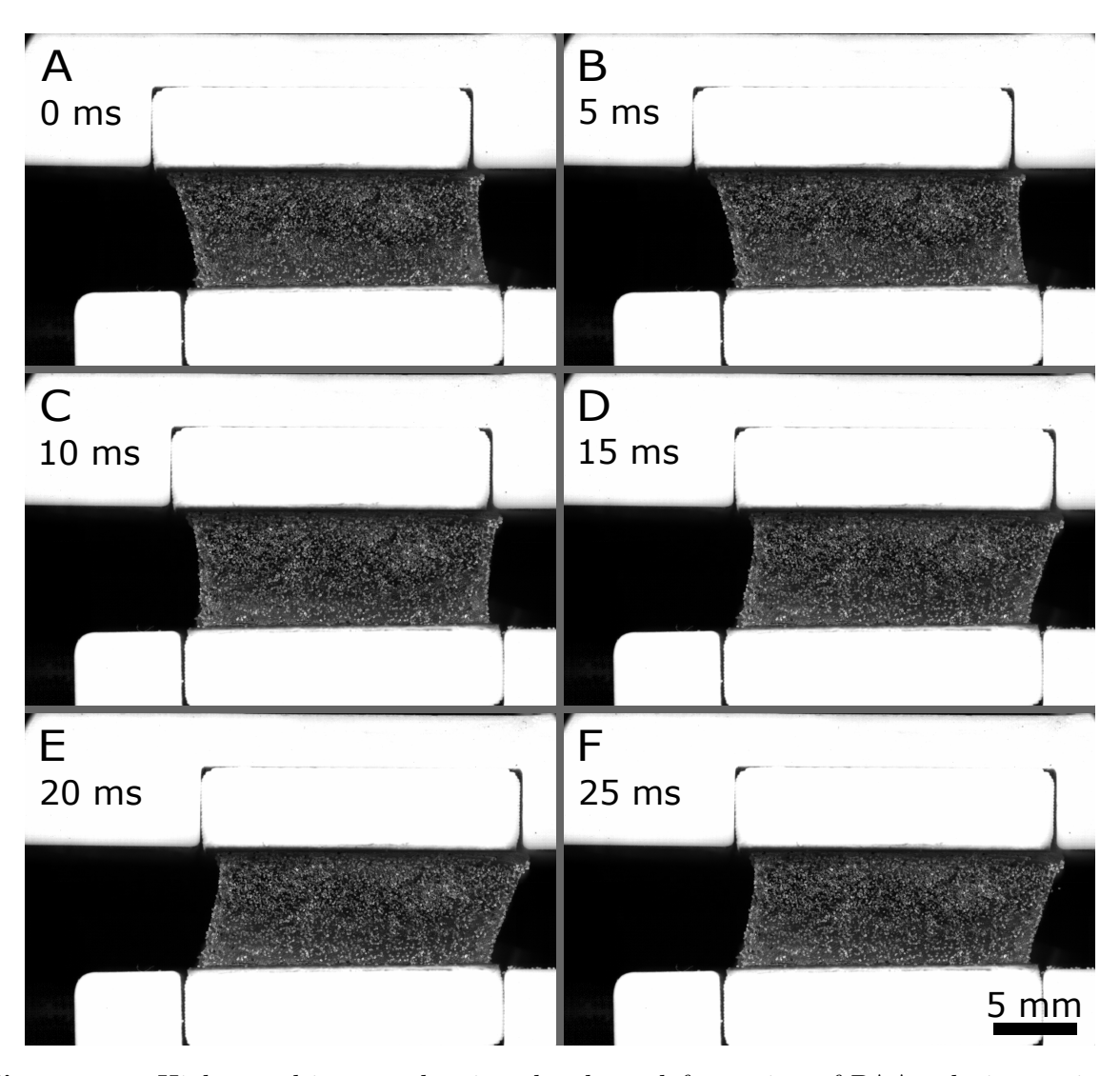


Figure 5.5: High-speed images showing the shear deformation of PAA gelatin specimen

These pre-processed images were cross-correlated using PIV to calculate the displacement field. For the PIV calculations, a window size of 32 pixels and a 50 % window overlap was used. The processed images overlaid with the displacement field vectors are shown in figure 5.6. The PIV calculations were performed using two different methods: our in-house developed PIV code and the open-source PIVLab toolbox [104]. Both of these methods produced very consistent results validating the implementation of the PIV technique.

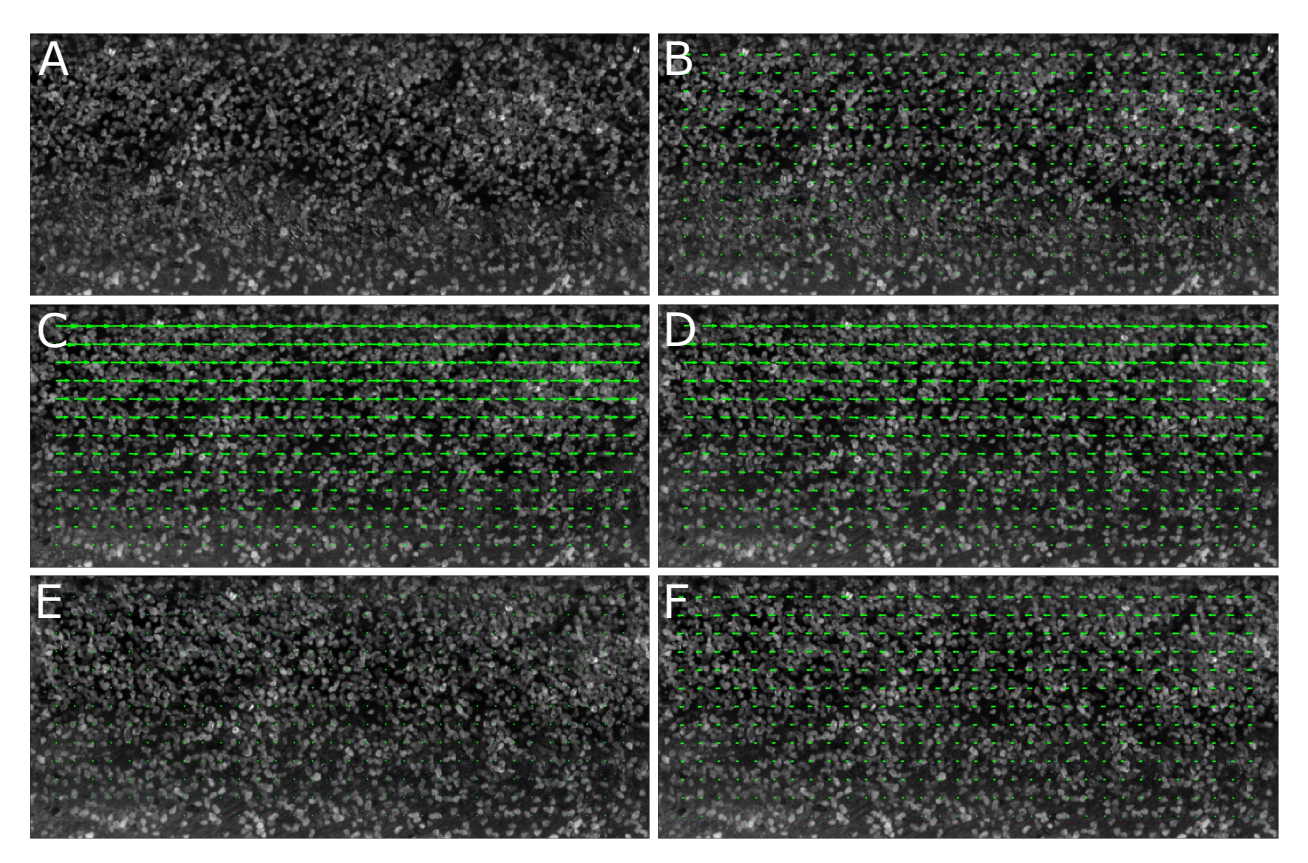


Figure 5.6: Processed images of the gelatin specimen overlaid with displacement field vectors at time (A) $t=0\,\mathrm{ms}$, (B) $t=5\,\mathrm{ms}$, (C) $t=10\,\mathrm{ms}$, (D) $t=15\,\mathrm{ms}$, (E) $t=20\,\mathrm{ms}$, and (F) $t=25\,\mathrm{ms}$

Once the displacement field between two consecutive frames was obtained using PIV, the shear strain field was computed using the equation,

$$\gamma = \frac{\partial u_1}{\partial y} + \frac{\partial u_2}{\partial x},\tag{5.3}$$

where u_1 and u_2 denote the displacement components in x and y directions [88]. This shear strain field was averaged to find the mean shear strain experienced by the specimen. Lastly, the instantaneous mean shear strain measurements were summed cumulatively to obtain the time evolution of the shear strain profile. The displacement of the top plate was also measured using the displacement sensor. The top plate displacement measured for the first two loading cycles is shown in figure 5.7. The shear strain profile was also calculated using this displacement measurement and equation (5.1). The shear strain profiles computed from all these methods for the first two loading cycles are compared in figure 5.8.

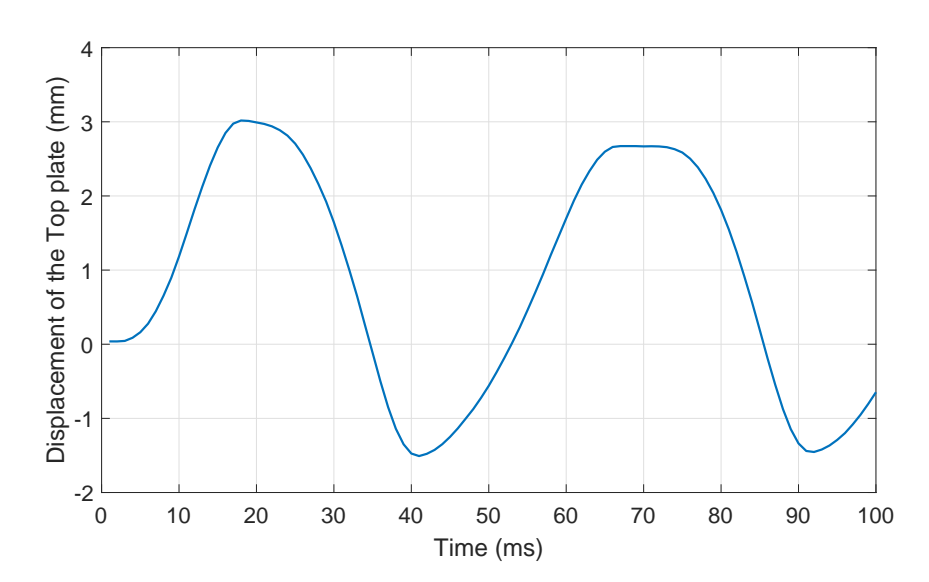


Figure 5.7: Measured top plate displacement for the first two loading cycles

It is evident that the strain profiles obtained from all three methods closely follow each other, showing consistent measurements. Thus, by only measuring the top plate's displacement, the average shear strain experienced by the specimen can be measured accurately. Hence, only the displacement data obtained from the displacement sensor was used to compute the shear strains for the later experiments.

The shear strain-rate profile was also computed from the shear strain profile. The com-

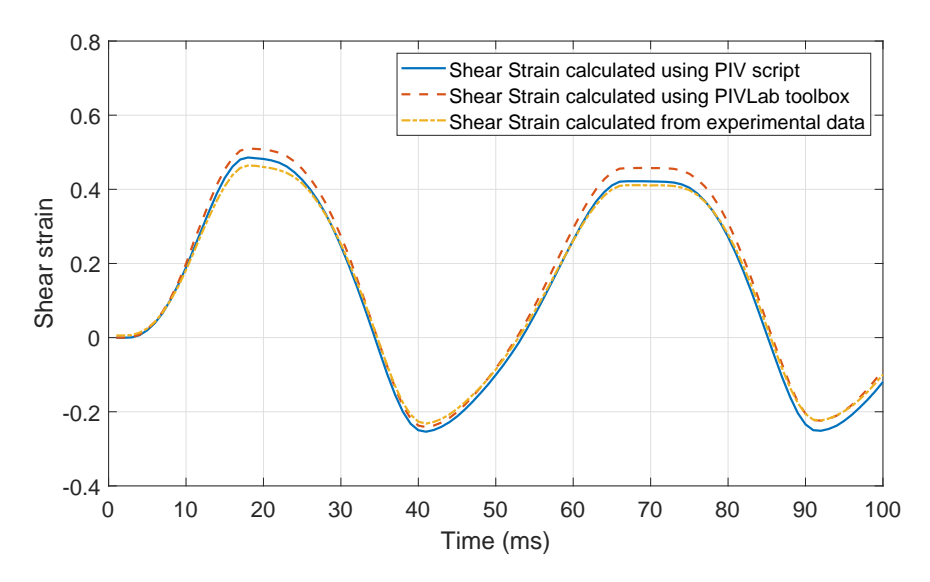


Figure 5.8: Comparison of the shear strain profiles computed using our in-house developed PIV script, the PIVLab toolbox, and the measured top plate displacement profile

puted shear strain-rate profile for the first two loading cycles is shown in figure 5.9. The apparatus was able to induce shear deformations of strains up to 50% at strain-rates up to $50\mathrm{\,s^{-1}}$ for $20\mathrm{\,Hz}$ operating frequency. Similar experiments were conducted at various frequencies, and the results are detailed in section 5.4.

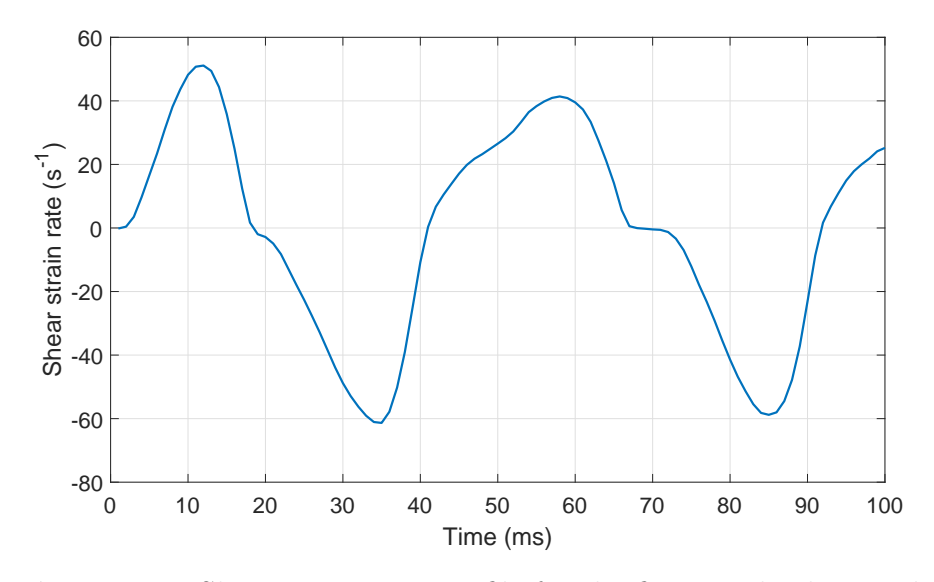


Figure 5.9: Shear strain-rate profile for the first two loading cycles

5.2.5 Control

5.2.5.1 System Identification

For system identification, the shear apparatus is considered as a single-input single-output (SISO) system. The input to the system is a -10 to $10 \,\mathrm{V}$ signal provided to the power amplifier. Based on the input voltage signal, the power amplifier generates a proportional -3 to 3 A current signal to drive the voice-coil actuator. Since the shear strain induced in a specimen depends on the displacement of the top plate (equation (5.1)), the resulting displacement generated by the voice-coil actuator is considered as the output of the system. The system identification for the shear apparatus was performed similar to the pressure apparatus (see section 3.3.1), i.e., by exciting the actuator with a chirp (sine-sweep) signal and evaluating the displacement generated by the actuator. The voice-coil actuator was excited with a sine-sweep signal having a 10 Hz start frequency, 200 Hz end frequency, and the total duration of 2 seconds. Also, the amplitude of the sine-sweep input was varied over the multiple tests. The input parameters for these sine-sweep experiments are given in table 5.1. The maximum displacement limit for the voice-coil actuator is 3 mm. When the actuator was excited with sine-sweep inputs of amplitude greater than 2.5 V, the displacement profile saturated at 3 mm for some of the frequencies. This output saturation could result in incorrect system identification. Thus, the sine-sweep amplitude for the system identification

Table 5.1: Input parameters of the sine-sweep system identification experiments conducted for the shear apparatus (Design iteration I)

Start Frequency (Hz)	End Frequency (Hz)	Duration (s)	Input Amplitude (V)	Number of experiments
10	200	2	1.5	5
10	200	2	2	5
10	200	2	2.5	5

experiments was restricted to 2.5 V.

As a representative result, the chirp input signal having 2 V amplitude is shown in figure 5.10a, and the corresponding output displacement generated by the voice-coil actuator is shown in figure 5.10b. These input and output profiles were analyzed in the frequency

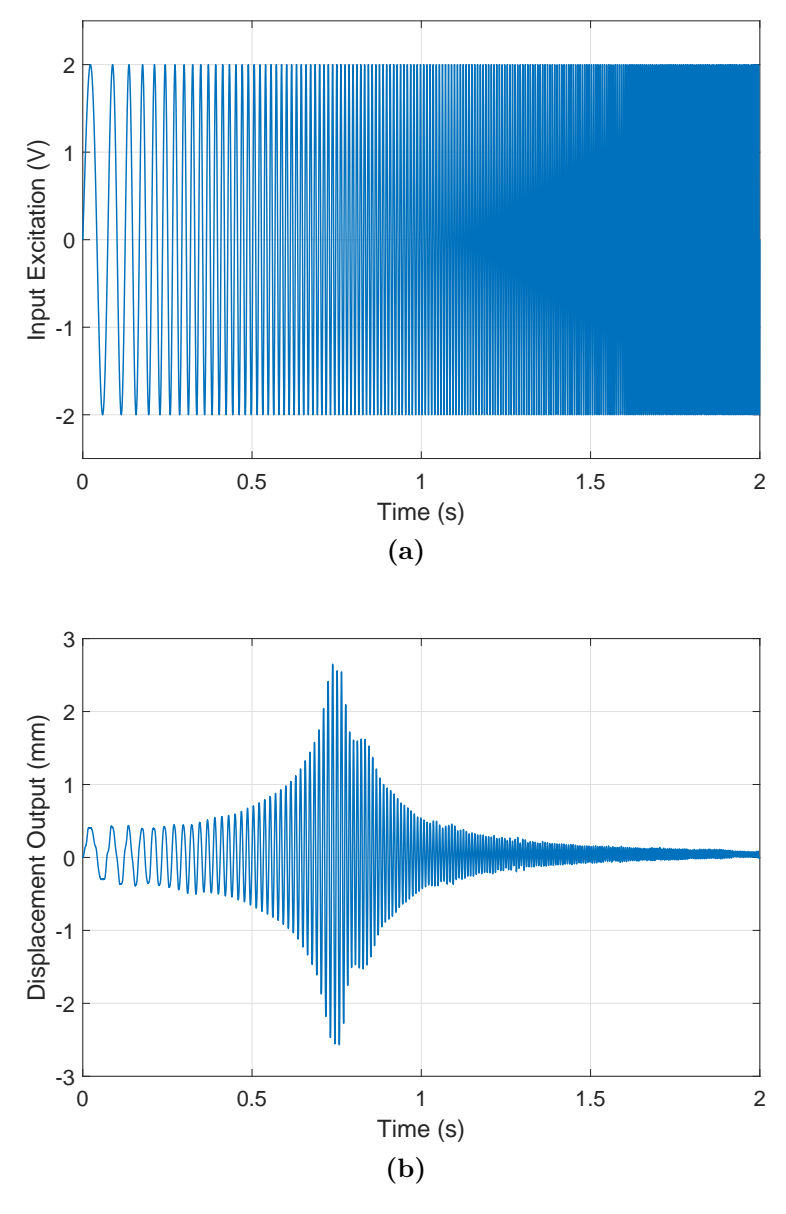


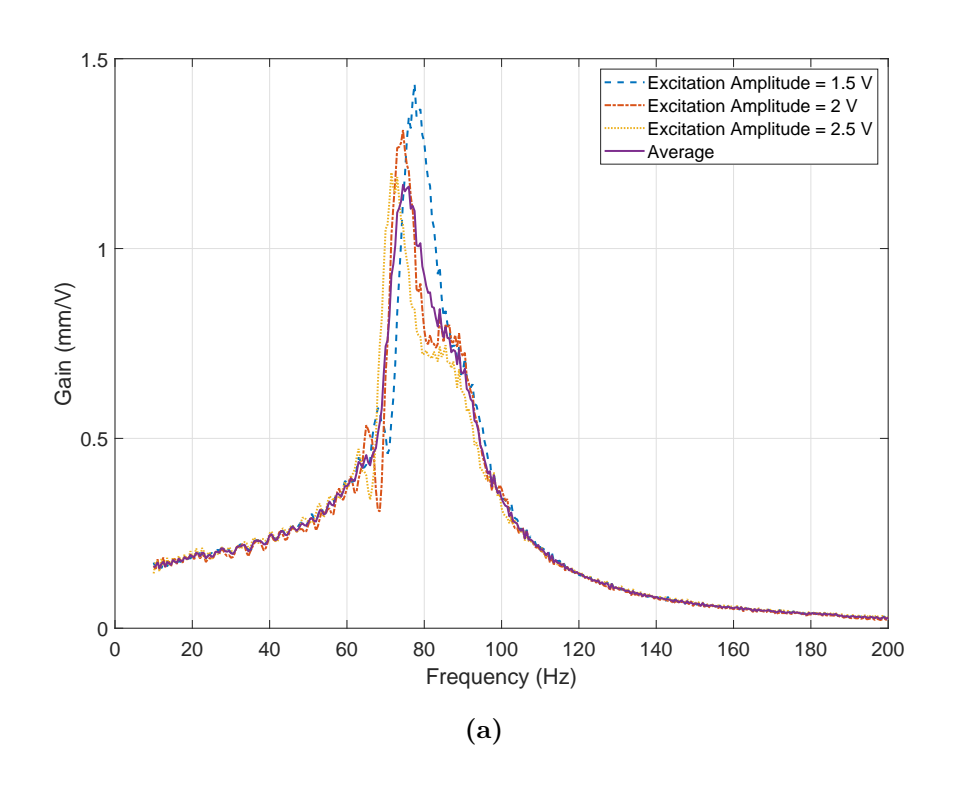
Figure 5.10: (a) Chirp voltage profile given as an input to the shear apparatus for a system identification experiment. (b) Output displacement profile generated as a response to the chirp excitation

domain to determine the gain curves and the phase difference curves. The methodology used for this analysis is the same as the one used for the system identification of the pressure apparatus (see section 3.3.1). The gain curve and the phase difference curve were determined for all of the 15 sine-sweep experiments. The average gain curves and the average phase difference curves were computed for the tests having the same input excitation amplitudes. These curves are shown in figure 5.11a and figure 5.11b along with the overall average gain curve and the overall average phase difference curve. These system identification curves, the overall average gain curve and the overall average phase difference curve, were used to design a feedforward controller for the output tracking problem.

5.2.5.2 Feedforward Control

The design and the implementation of the feedforward controller for the shear apparatus is the same as the feedforward controller for the pressure apparatus (see section 3.3.2). As a test case for the output tracking problem, a multi-modal displacement profile was constructed by adding three sine waves with frequencies of 20 Hz, 40 Hz, and 60 Hz, and amplitude of 0.75 mm. The constructed displacement profile is shown in figure 5.12.

The designed feedforward controller was used to determine the control input profile. The control input profile generated by the controller for this output tracking problem is shown in figure 5.13. It is evident that the control input profile exhibits the amplitude and phase modulation characteristics of the system. This control input profile was then fed to the power amplifier that powered the voice-coil actuator. The output displacement profile generated by the voice-coil actuator in response to the control input profile was recorded. This experiment was repeated twice, and the measured displacement profiles for both the experiments are shown in figure 5.14 along with the target displacement profile.



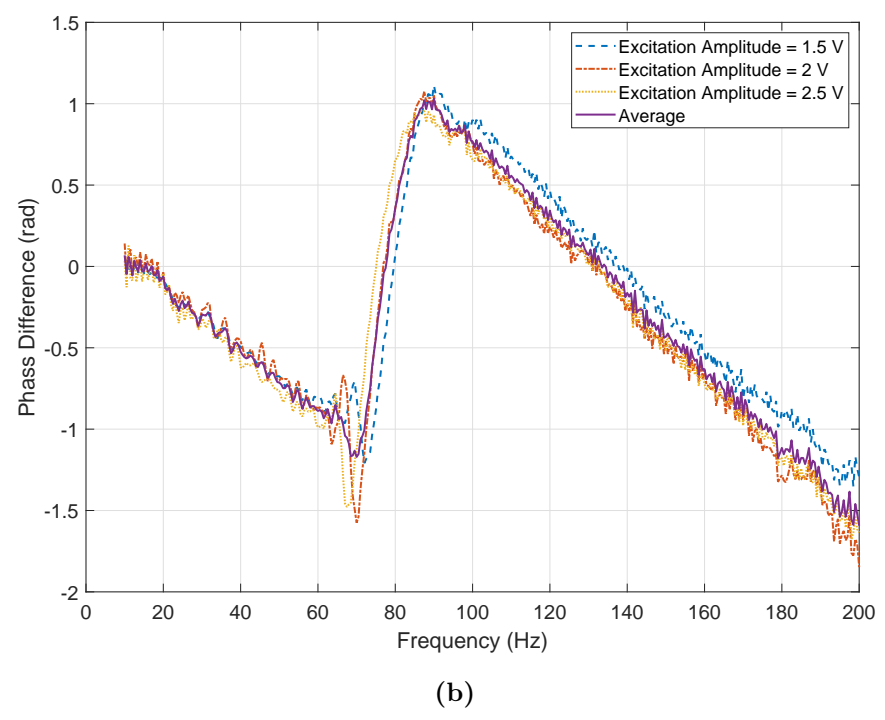


Figure 5.11: (a) Gain curves and (b) phase difference curves for the shear apparatus (Design iteration I) determined from system identification experiments

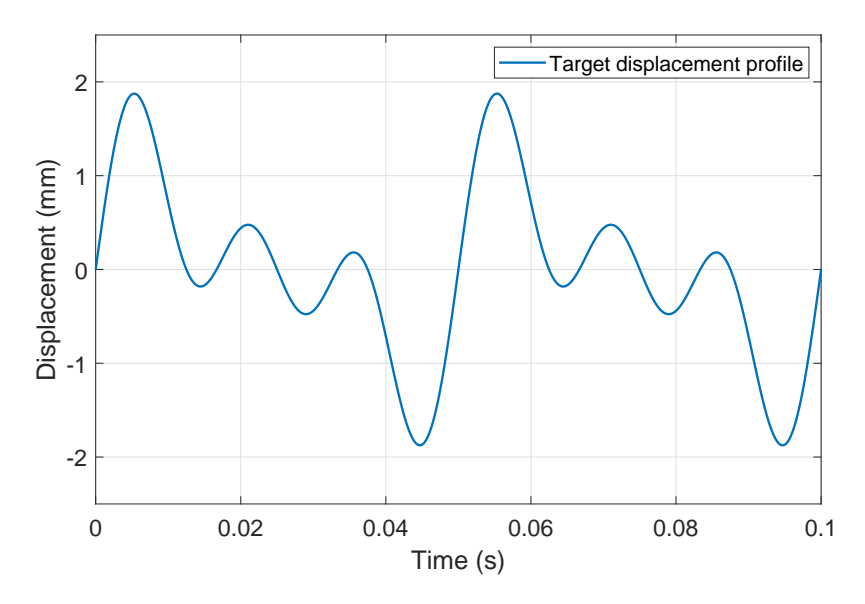


Figure 5.12: Multi-modal target displacement profile constructed for an output tracking problem

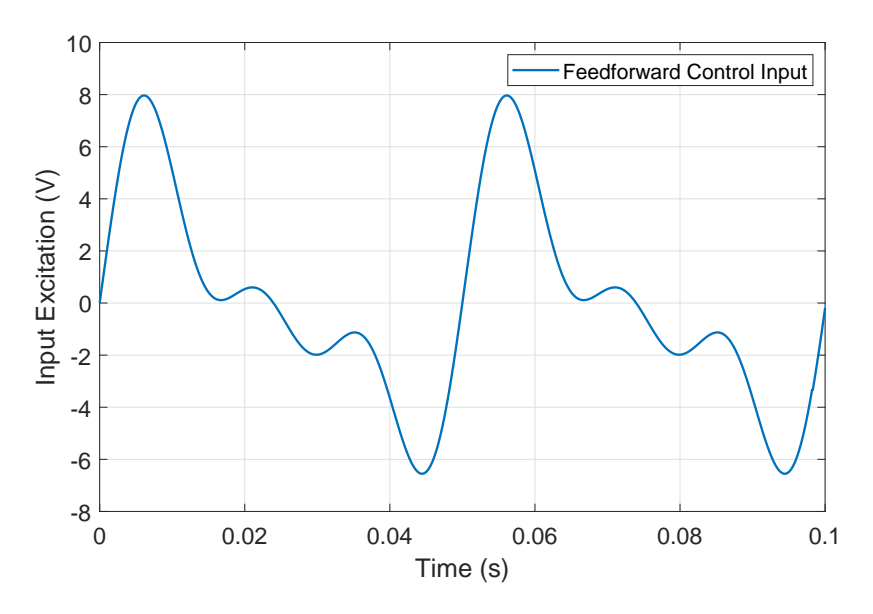


Figure 5.13: Control input profile determined by the feedforward controller

The displacement profiles generated by the actuator were in moderate agreement with the target displacement profile. The two experimental displacement profiles were in good agreement with each other, indicating the repeatability of the experimental results. The experimental displacement profiles provided over 89% fit to the target displacement profile

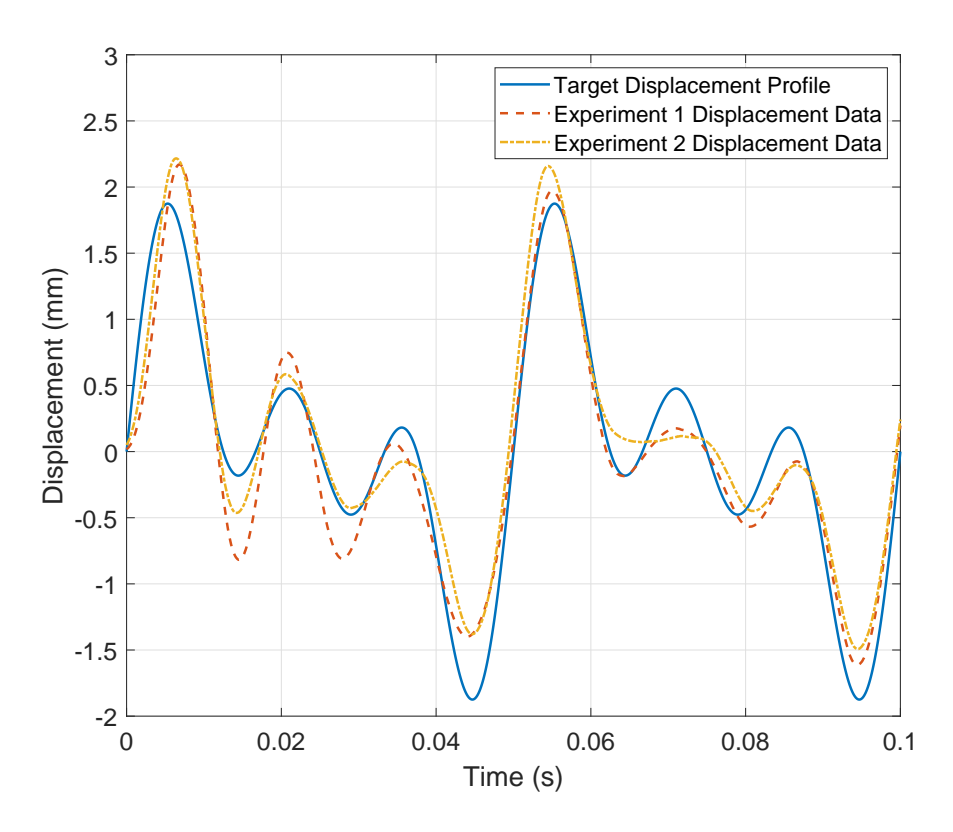


Figure 5.14: Comparison between the target displacement profile and the experimental displacement profiles obtained using the feedforward controller

based on the normalized mean squared error (NMSE) calculation. As seen in figure 5.11a, the gain curves vary with the input excitation amplitude. Using the average gain curve as a system identification curve does not capture the variation of the gain with the input amplitude. Thus, system identification misses some of the system characteristics and diminishes the performance of the feedforward controller.

5.2.6 Limitations

This fabricated design of the first-iteration shear apparatus was used to conduct preliminary experiments on PAA gelatin specimens. The details of these experiments are provided in section 5.4. This fabricated design was observed to have some design flaws that necessitated

a revision in the design. There is no provision to precisely control the gap between the two parallel plates or the specimen thickness in the current design. Moreover, the specimen cannot be precisely pre-compressed between the parallel plates. Consequently, pre-compression cannot be used to hold the specimen between the plates, requiring the specimen to be glued to both plates. The requirement of gluing the specimen to the plates reduces this apparatus's applicability in studies involving biological specimens.

In the current design, both of the parallel plates are supported at a single location; the top is connected to the shaft of the voice-coil actuator, and the bottom plate is connected to the load cell using threaded rods. This arrangement makes the plates susceptible to transverse vibrations like a cantilever beam. These transverse vibrations can induce tension or compression in the specimen and prevent loading it in a simple-shear state. These transverse vibrations were mainly observed when the PAA gelatin specimens were loaded at high shearing frequencies. Moreover, the voice-coil actuator's shaft can rotate along its axis, which makes the top plate susceptible to an out-of-plane motion, and again, can prevent loading specimen in a simple-shear state.

The designed feedforward controller for the apparatus relies on the average gain curve and the average phase difference curve for system characteristics. It was observed that the gain curve for the voice-coil actuator varies with the input amplitude. This variation was not fully captured in the average gain curve, leading to inaccurate system identification and limiting the feedforward controller's performance. Moreover, the feedforward controller does not account for the variability in specimen stiffness, which could further degrade its performance while generating user-specified shear strain profiles.

All of the aforementioned limitations of the shear apparatus design were addressed in the next design iteration. The details of the revised design are provided in the following section.

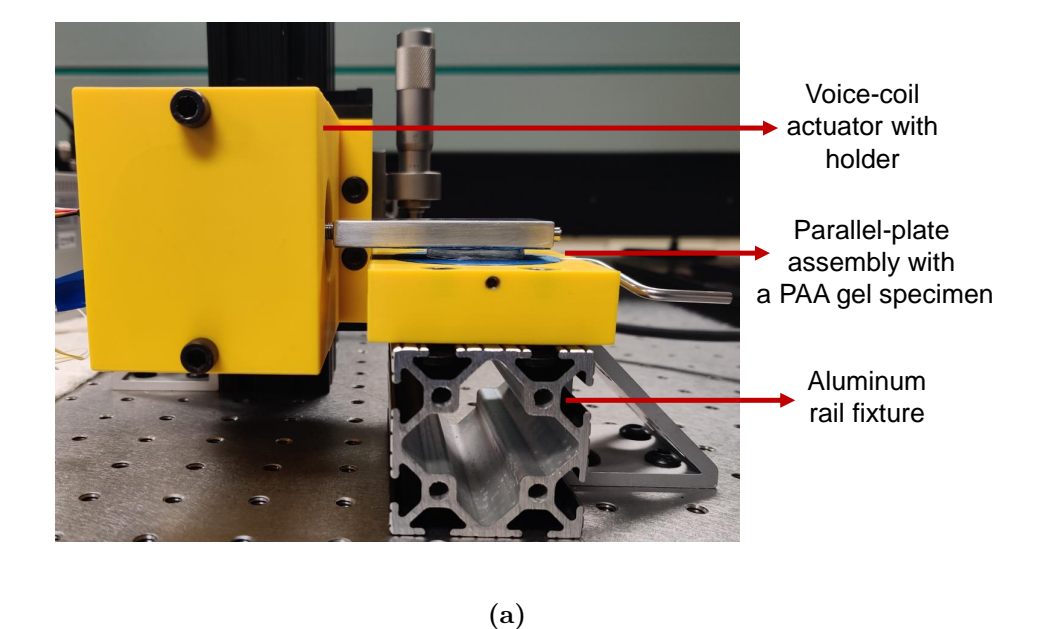
5.3 Design Iteration II

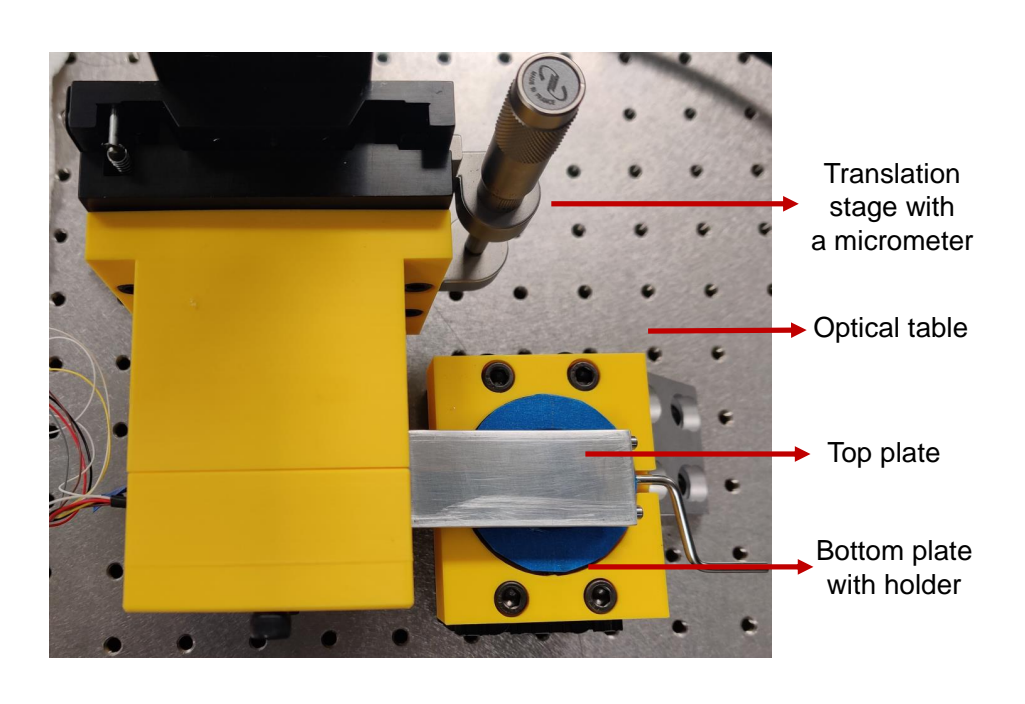
5.3.1 Working Principle

The second-iteration design of the shear apparatus has the same working principle as the previous design. It uses a parallel plate assembly to hold the specimen and a voice-coil actuator to displace the top plate while the bottom plate is held stationary. The major upgrade in the second iteration is the new voice-coil actuator (Model LAS16-23-000A-P01-4E, Sensata Technologies, Inc.) that has an integrated position sensor. Since the position feedback is available from the voice-coil actuator itself, there is no need for an additional displacement sensor like the one used in the previous design. Moreover, since the role of this apparatus is to load biological specimens under dynamic shear loadings and not to determine the mechanical properties on the specimen, the load cell is removed from the apparatus as shear stress measurement is not required. Rheometers are better suited and optimized for determining the mechanical properties of a specimen under dynamic shear loads [59]. Thus, they should be used instead of this apparatus for material characterization applications. A translation stage and a micrometer were included in the design, and the voice-coil actuator was mounted on the translation stage using appropriate fixtures. This arrangement enables to precisely control the gap between the parallel plates or the specimen thickness. Moreover, a specimen can be precisely pre-compressed and held between the plates without gluing it to both plates.

5.3.2 Device Fabrication

The fabricated second-iteration design of the shear apparatus is shown in figures 5.15a and 5.15b. The voice-coil actuator is mounted on the translation stage using custom fixtures





(b)

Figure 5.15: (a) Front-view and (b) top-view of the fabricated setup of the shear apparatus (Design iteration II)

3D printed out of PLA filament. The top plate is machined out of aluminum and coupled with the shaft of the voice-coil actuator. Two partially threaded studs are attached to the

voice-coil as a guide rail for the top plate. These support studs prevent the out-of-plane motion of the top plate and also minimize the transverse vibrations of the top plate. This arrangement ensures that the top plate is always parallel to the bottom plate, and the gap between the plates is constant throughout the actuation cycle. The bottom plate is held fixed using a custom 3D printed fixture. The voice-coil and the translation stage assembly is mounted on a T-slotted aluminum rail (80/20 Inc.), bolted to an optical table. Similarly, the bottom plate fixture is mounted on an aluminum rail (80/20 Inc.), which is again bolted to the optical table.

5.3.3 Instrumentation and Control

A servo drive (Pluto Servo Drive, Ingenia Motion Control) is used to power as well as control the voice-coil actuator. The servo drive uses position feedback from the integrated position sensor of the voice-coil actuator to control it a closed-loop. A proportional-integral-derivative (PID) controller is implemented using the servo drive to control the displacement of the voice-coil actuator. The gains of the PID controller were tuned for the optimal tracking of the user-defined displacement profiles. A 24 V power supply unit (Model MS2-H50, Keyence Corporation) is used to power the servo drive. The target displacement profile for the voice-coil actuator is provided in the form of a -10 V to 10 V signal, which corresponds to -3 mm to 3 mm displacement. A data acquisition device (Model cDAQ9178 with NI9215 and NI9263, National Instruments) was used to generate the target displacement voltage signal and acquire the actual displacement data measured by the integrated position sensor. A custom LabVIEW program was developed to perform and synchronize both the signal generation and the data acquisition tasks at the sampling frequency of 10 k samples per second. A high-speed camera (Model Phantom V2512) was also added to the system to

record the shear loading cycles at 10 k frames per second. Lastly, a 5 V transistor-transistor logic (TTL) trigger pulse was used to synchronize the actuation of the voice-coil actuator with the acquisition of displacement and high-speed imaging data.

The performance of the closed-loop PID controller was determined by conducting shear tests on a PAA gelatin specimen. For these tests, a PAA gelatin specimen of 10% concentration (weight/volume) and a disk shape with 25.4 mm diameter and 4 mm thickness was used. The specimen was loaded at three frequencies of 10 Hz, 50 Hz, and 100 Hz, for 10 loading cycles each. For all of these loading cycles, the shear strain amplitude was set to 10%. Based on the loading cycles, the target displacement profiles for the voice-coil actuator were determined and fed to the controller. These target displacement profiles are shown in figure 5.16 along with the actual displacement profiles generated by the actuator. It is evident that the PID controller could reasonably track the target displacement profile. There is a delay between the target profile and the measured displacement profile. The inertia of the system and the response time of the PID controller give rise to this delay. The delay between the profiles become prominent for the higher frequencies.

The shear strain profiles were determined for the experimental displacement profiles using the equation (5.1). Since the delay between the target and the measured displacement profiles does not affect the shear loading experienced by the specimen, the delay was removed while plotting the strain profiles by defining a new starting time for each test. The shear profiles are shown in figure 5.17. These profiles exhibit a sinusoidal form with a 10% shear strain amplitude. Based on the results, the PID controller's performance was considered reasonable for generating sinusoidal shear loading cycles. This second-iteration fabricated design of the shear apparatus was used to conduct preliminary experiments on mouse brain tissue specimens. These ex-vivo experiments are discussed in chapter 6 (section 6.1.2).

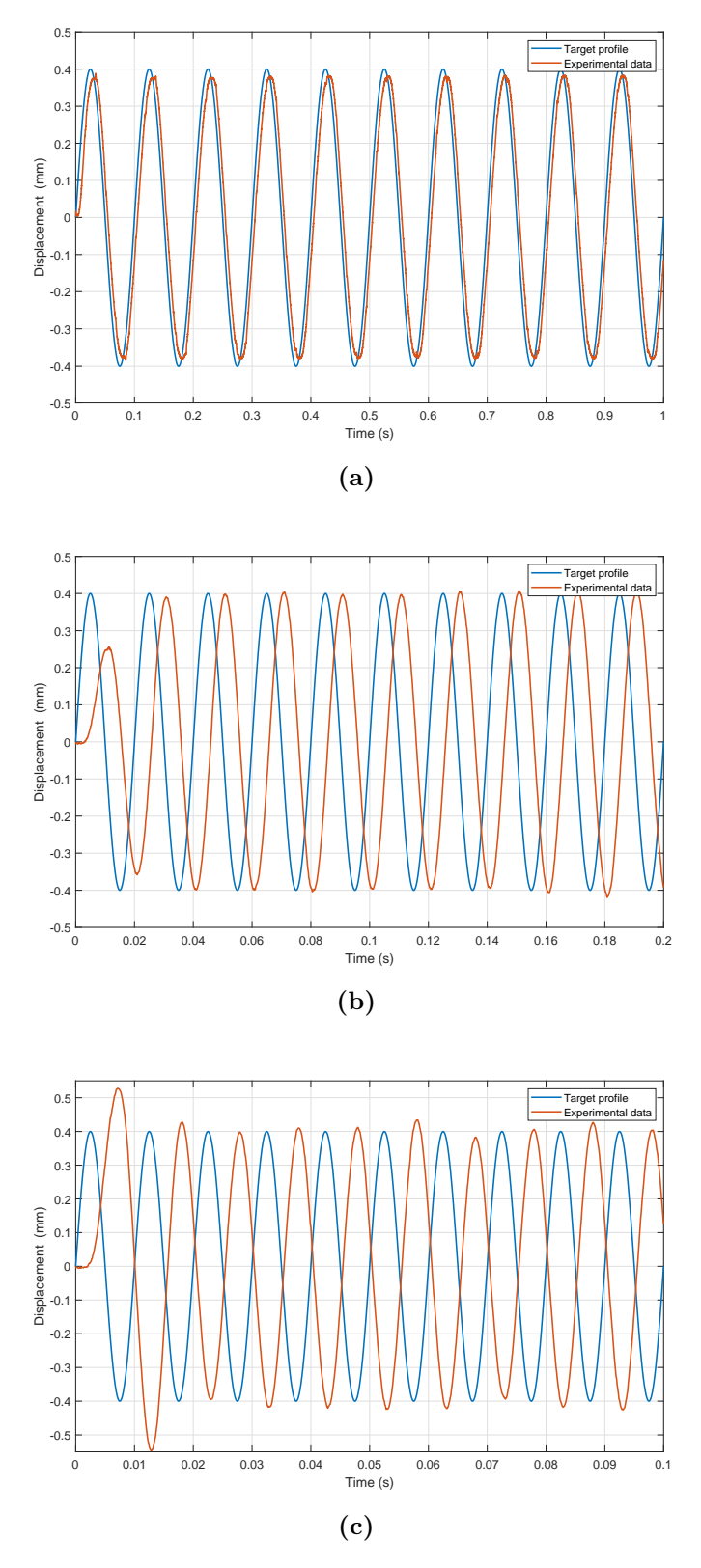


Figure 5.16: Comparison between the target displacement profiles and the experimental displacement profiles generated by the voice-coil actuator for a loading frequency of (a) $10\,\mathrm{Hz}$, (b) $50\,\mathrm{Hz}$, and (c) $100\,\mathrm{Hz}$

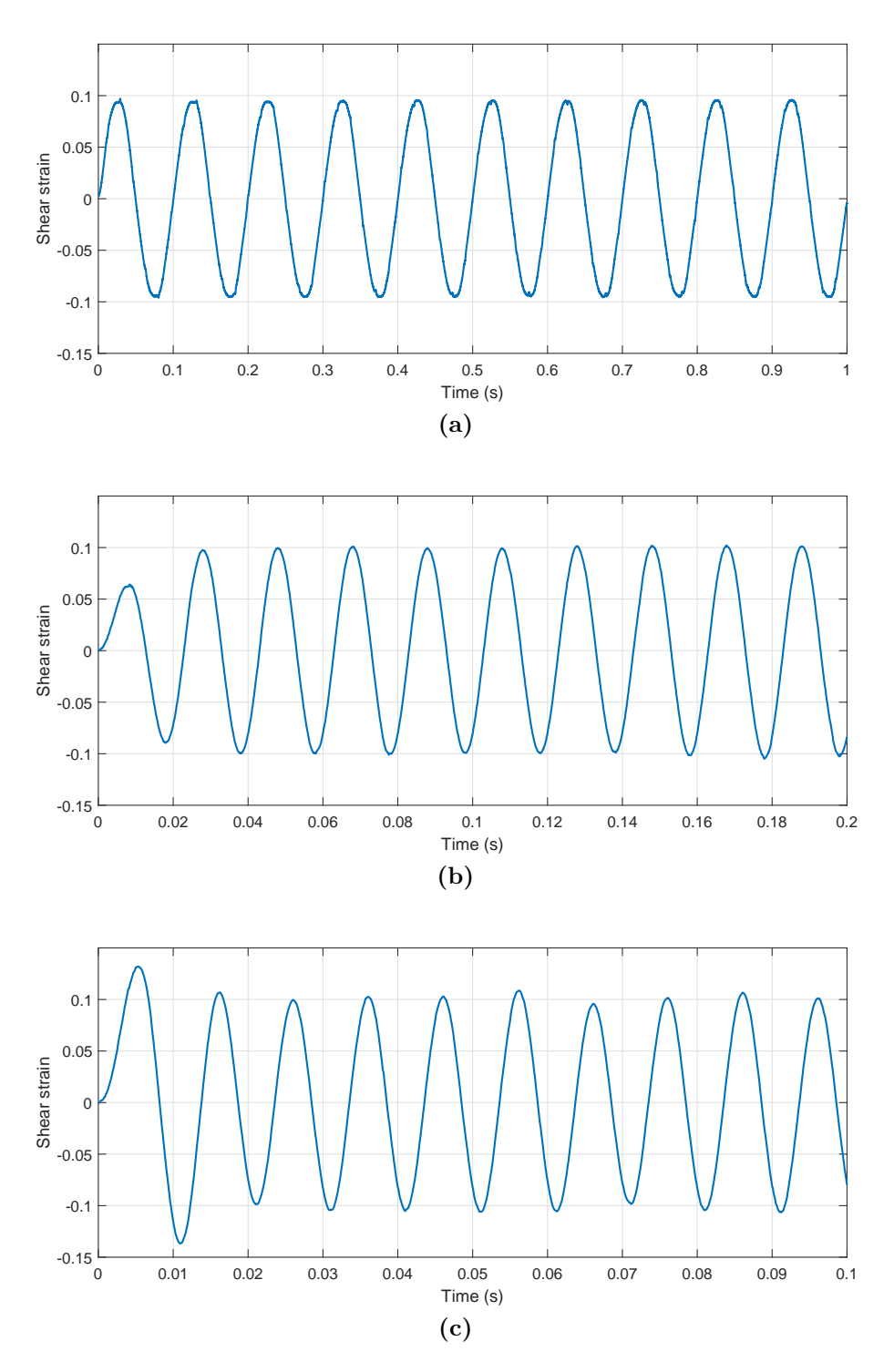


Figure 5.17: Sinusoidal shear strain profiles generated by the shear apparatus (Design iteration II) for a loading frequency of (a) $10\,\mathrm{Hz}$, (b) $50\,\mathrm{Hz}$, and (c) $100\,\mathrm{Hz}$

5.4 Results and Discussion

This section presents the results from the material characterization experiments performed on PAA gelatin specimens. The shear apparatus fabricated in the first design iteration was used for these shear experiments. In these tests, the PAA gelatin specimens of 10% weight by volume concentration were characterized under dynamic shear loading. Each of the loading cycles consisted of a sinusoidal shear loading of a particular frequency for 10 oscillations. The loading frequency was varied from 10 Hz to 100 Hz in steps of 10 Hz. The shear test at each frequency was repeated 4 times. Thus, 40 shear tests were performed to determine the shear properties of PAA gelatin specimens in total. For each test, the shear strain profile was obtained by measuring the top plate displacement, and the shear stress profile was computed from the force data measured with the load cell. The representative shear stress-strain profiles for 20 Hz and 50 Hz loading cycles are shown in figures 5.18a and 5.18b. The shear stress-strain profiles follow a similar temporal character. Also, the stress profile lags with respect to the strain profile.

For each of these experiments, the current profiles given as excitation inputs to the voice-coil actuator were sine waves of particular operating frequencies. However, the strain profiles generated by the apparatus are not perfectly sinusoidal. The system dynamics of the apparatus, which includes the response of voice-coil to input current, hysteresis, out of the plane motion or the transverse oscillations of the parallel plates, etc., is responsible for the non-sinusoidal strain profiles. These limitations of the apparatus were addressed in the second design iteration.

The shear stress-strain profiles for each experiment were correlated to evaluate the shear moduli. The amplitude of the shear strain profile (γ_a) and the amplitude of the shear stress

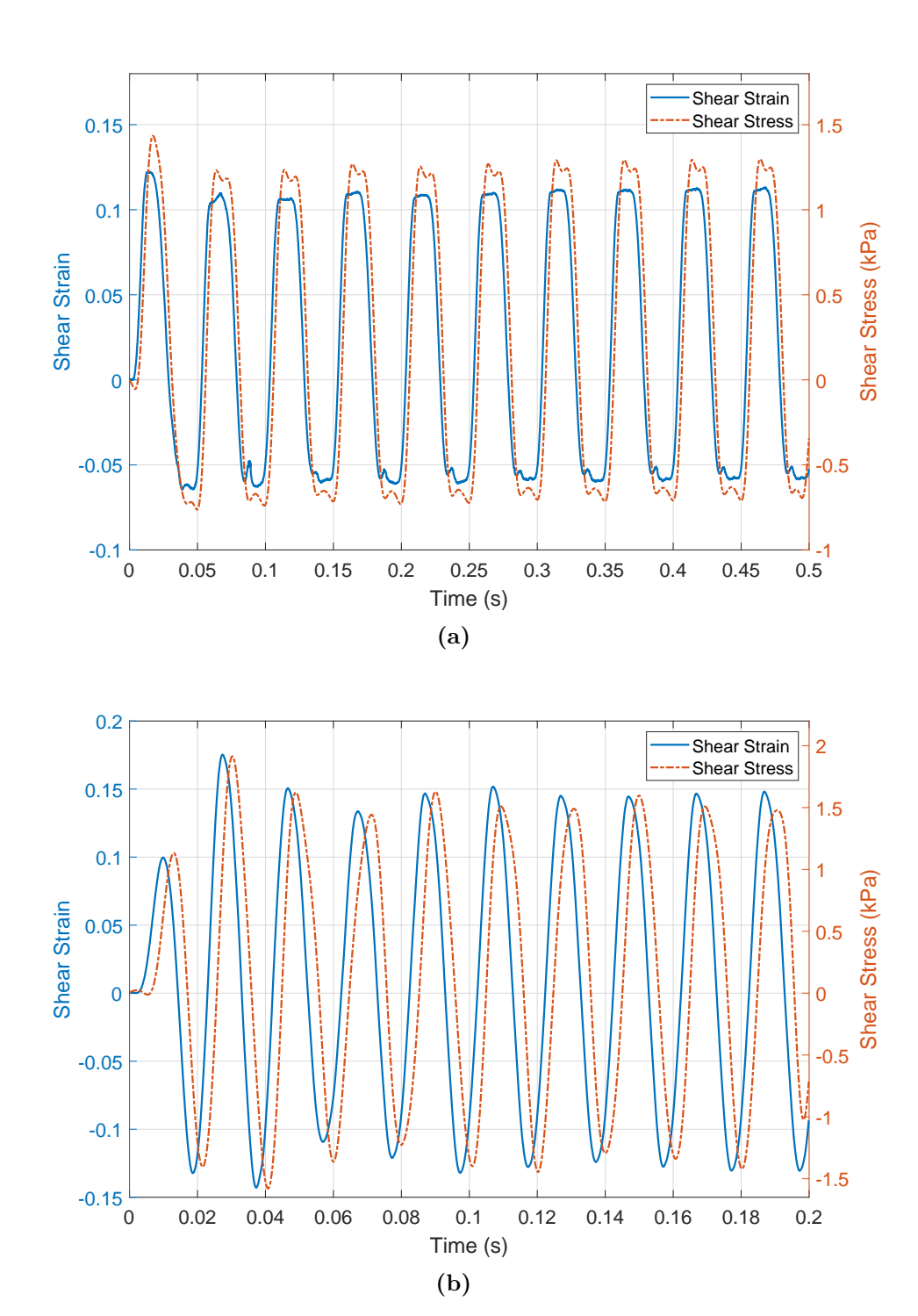


Figure 5.18: Shear strain (left y-axis) and shear stress (right y-axis) profiles for PAA gelatin shear tests at (a) 20 Hz and (b) 50 Hz loading frequency

profile (τ_a) for the actuation frequency were determined by transforming the profiles in the frequency domain using the Fast Fourier Transform (FFT). These amplitudes were then

used to determine the complex shear modulus (G^*) of the gelatin specimen [60] using the equation:

$$G^* = \frac{\tau_a}{\gamma_a}. (5.4)$$

The complex shear moduli were determined for all the operating frequencies, and the variation is shown in figure 5.19.

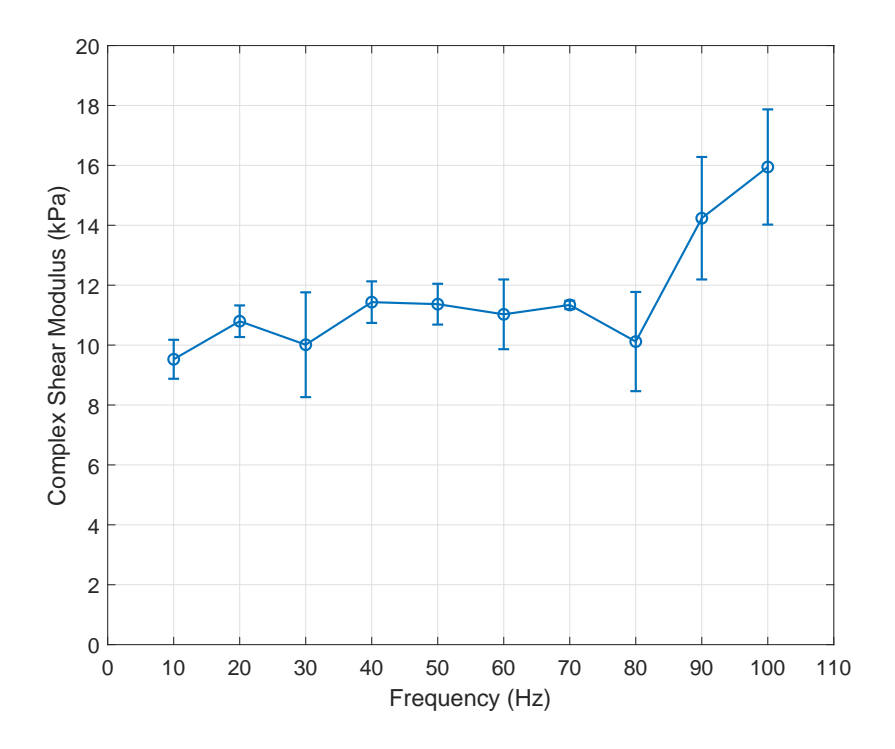


Figure 5.19: Variation of the complex shear modulus of PAA gelatin with loading frequency

The time delay (Δt_{total}) between the shear strain and stress profiles consists of two parts: the transport delay $(\Delta t_{transport})$ and the delay due to the viscoelastic nature of the PAA gel $(\Delta t_{viscoelastic})$. This gives:

$$\Delta t_{total} = \Delta t_{transport} + \Delta t_{viscoelastic} \tag{5.5}$$

Since the strain is measured at the top plate, and the stress is measure at the bottom plate,

there is a transport delay that corresponds to the time taken by the shear waves to travel across the specimen. This transport delay was estimated from the elastic shear wave speed (β) and the specimen thickness (d) using the equation,

$$\Delta t_{transport} = \frac{d}{\beta}. (5.6)$$

The elastic shear wave speed is given by the equation [60, 81],

$$\beta = \sqrt{\frac{G^* \cos(\delta)}{\rho_{gel}}},\tag{5.7}$$

where ρ_{gel} denotes the density of the gel specimen and δ is the phase difference between the shear stress-strain profiles arising from the viscoelastic nature of the specimen. The density was determined to be $1200 \,\mathrm{kg/m^3}$. Also, $\Delta t_{viscoelastic}$ is related to δ as given in the equation,

$$\Delta t_{viscoelastic} = \frac{\delta}{2\pi f_a},\tag{5.8}$$

where f_a is the voice-coil actuation frequency. Combining equations (5.5) to (5.8) gives:

$$\Delta t_{total} = d \times \sqrt{\frac{\rho_{gel}}{G^* \cos(\delta)}} + \frac{\delta}{2\pi f_a}.$$
 (5.9)

The time delay (Δt_{total}) between the shear strain and stress profiles was measured by cross-correlating them using finddelay function in MATLAB. Since all the entities in equation (5.9) except δ are predetermined, this non-linear equation was solved numerically using MATLAB to evaluate δ . Consequenctly, the loss factor for the gelatin specimen, i.e., $\tan(\delta)$, was determined [77]. The variation of the loss factor with frequency is shown in figure 5.20.

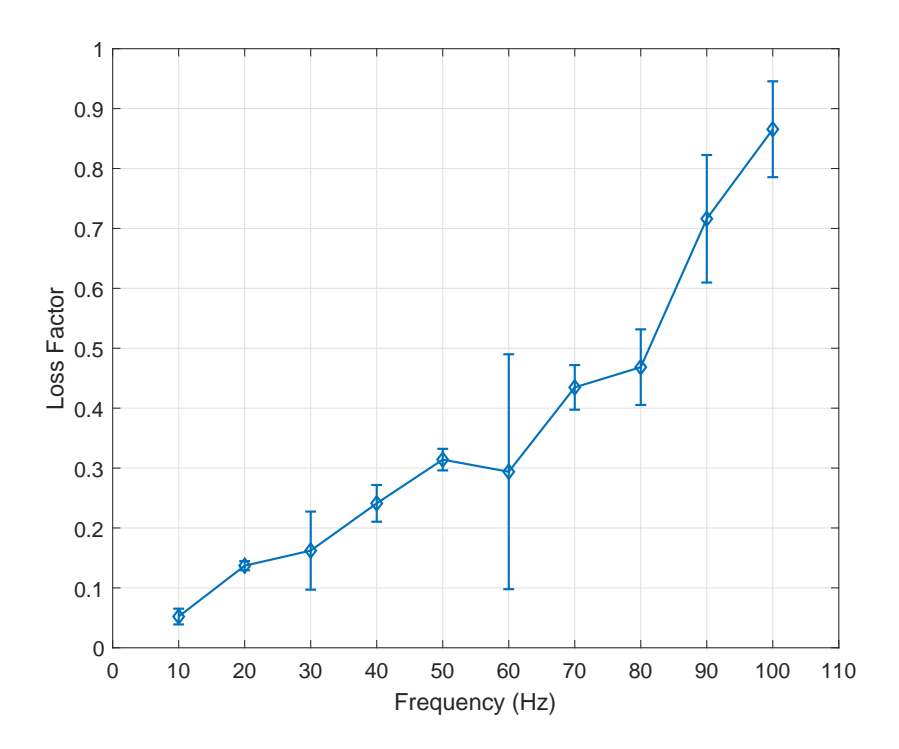


Figure 5.20: Variation of the loss factor of PAA gelatin with loading frequency

The loss factor was observed to increase with the increase in loading frequency. Theoretically, since the specimen is in a solid-state at resting condition, the loss factor should always lie between 0, and 1 [59]. The experimentally evaluated loss factor was consistent with the theoretical limits. The phase lag δ was further used to determine the storage modulus (G'), and the loss modulus (G'') based on the relations [60,77],

$$G' = G^* \cos(\delta)$$
 and $G'' = G^* \sin(\delta)$.

The loss factor represents the ratio of the loss modulus to the storage modulus. The variation of storage and loss moduli with the loading frequency is shown in figure 5.21.

For the range of loading frequencies analyzed, it can be observed that the loss modulus increased with the increase in loading frequency. This signifies that more energy is dissipated

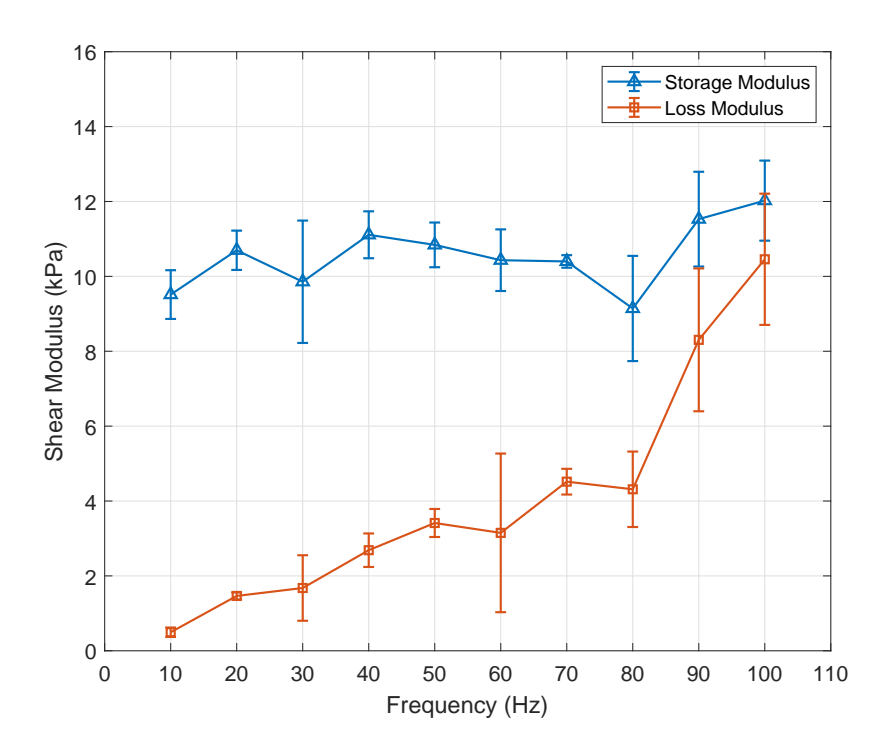


Figure 5.21: Variation of the storage and loss modulus of PAA gelatin with loading frequency

under dynamic shear loading at higher loading frequencies. However, this observation is limited to the range of frequencies analyzed in these experiments.

As the actuation frequency increases, the relative contribution of the specimen's inertia to the force measured at the bottom plate increases. These inertial effects lead to erroneous measurement of the shear force and, consequently, the shear moduli. Ideally, the contribution of the inertial effects to the shear force measurement may be neglected if the specimen thickness is small compared to the elastic shear wavelength (λ) in the specimen [60, 105]. The ratio of specimen thickness to the elastic shear wavelength is given by the equation,

$$\frac{d}{\lambda} = d \times f_a \times \sqrt{\frac{\rho_{gel}}{G'}}.$$
(5.10)

For the performed shear tests, the d/λ ratio was less than 0.1 for actuation frequency up to

50 Hz and increased steadily with the actuation frequency. The d/λ ratio was 0.17 for 100 Hz actuation frequency. Thus, at higher actuation frequencies, the inertial effects contributed to the erroneous determination of the shear moduli. The sudden rise in the complex shear modulus (seen in figure 5.19) at high actuation frequencies results from the overestimation of the modulus due to the inertial effects. The d/λ ratio can be reduced by decreasing the specimen thickness. Thus, to reduce any error associated with the inertial effects, the specimen thickness should be chosen appropriately.

5.5 Conclusion

We have developed an experimental apparatus that can induce shear loadings of various strain amplitudes and frequencies at the levels relevant to bTBI. This apparatus uses a voice-coil actuator and two parallel plates assembly to generate dynamic shear loadings. In this chapter, we have discussed the two design iterations of the shear apparatus. The first-iteration shear apparatus was used to conduct material characterization experiments for PAA gelatin specimens. These experiments also tested the implementation of the apparatus for loading samples of living tissue and three-dimensional cell cultures. The insights from these material characterization experiments inspired the design improvements implemented in the second iteration of the shear apparatus. Furthermore, the second-iteration shear apparatus was used to perform bTBI-related ex-vivo experiments on mouse brain tissue specimens.

Researchers have previously used a modified split Hopkinson pressure bar (SHPB) that includes a parallel plate fixture to shear the specimen at high strain-rates [57,58]. Usually, the high shear strain magnitudes generated by SHPB result in specimen tearing. These strain magnitudes are significantly higher than the ones associated with a primary bTBI event.

Moreover, the SHPB technique cannot generate oscillatory shear deformation associated with traveling shear waves. Rotation rheometers [59], and the other custom shear instruments developed by researchers [60–63] can generate either the shear strain amplitudes or loading frequencies typically associated with a bTBI event, but not both simultaneously. Our shear apparatus (second-iteration design) overcomes these limitations and can induce shear loads at the levels relevant to bTBI. Moreover, the designed apparatus is inexpensive, compact, portable, and highly controllable, making it well suited for biomedical applications.

Chapter 6

Preliminary Ex-vivo and In-vitro

Experiments

To explore the response of biological specimens to complex time-varying pressure cycles and dynamic shear loadings, we performed few preliminary ex-vivo and in-vitro experiments. These experiments served a dual purpose: (1) determining the pathophysiological response of the animal brain tissue specimens, cell cultures, and cerebral organoids to the blast-like intracranial effects and (2) testing the implementation of our experimental devices for bTBI-related studies.

In this chapter, section 6.1 discusses the preliminary *ex-vivo* experiments involving the mouse brain tissue specimens. The *in-vitro* experiments involving cell cultures and cerebral organoids are discussed in section 6.2.

6.1 Ex-vivo Experiments

This section discusses the preliminary ex-vivo experiments involving the mouse brain tissue specimens. The experiments were performed in collaboration with the Cox Lab in the Department of Physiology at Michigan State University. The Institutional Animal Care and Use Committee at Michigan State University approved all animal procedures performed here. The tests performed to evaluate the electrophysiological response of neurons to time-

varying pressure cycles and dynamic shear loadings are discussed in sections 6.1.1 and 6.1.2, respectively. The specimen preparation and post-exposure analysis for these tests were performed by Dr. Joseph Beatty at the Cox Lab.

6.1.1 Ex-vivo Experiments involving Time-varying Pressure Cycles

6.1.1.1 Experimental Procedure

Specimen Preparation: Mouse coronal brain slices containing the primary somatosensory cortex [106] were obtained by slicing the brain shortly after decapitation. The obtained slices were 300 μm thick. These brain slices were kept submerged in a cold, oxygenated (95% O₂ and 5% CO₂) artificial cerebrospinal fluid (aCSF) containing (in mM): 2.5 KCl, 26 NaHCO₃, 1.25 NaH₂PO₄, 10.0 MgCl₂, 2.0 CaCl₂, 234.0 sucrose, and 11.0 glucose. The brain slices submerged in aCSF are shown in figure 6.1.

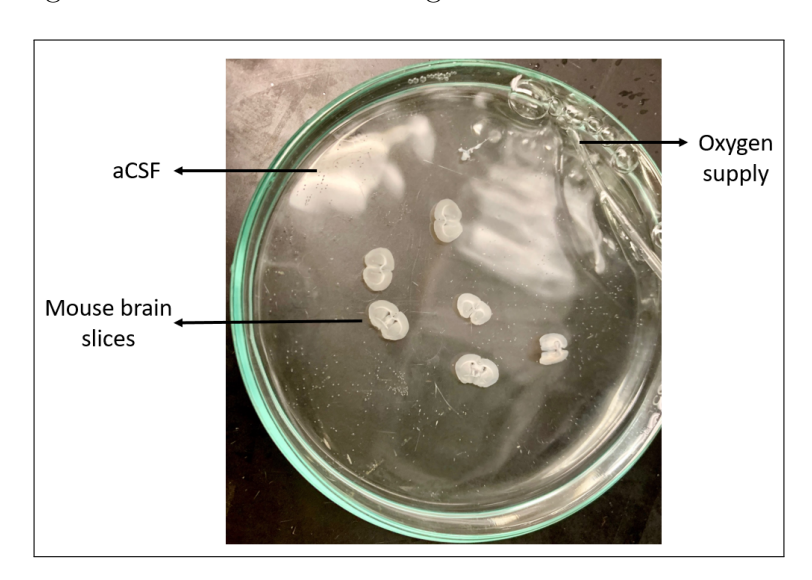


Figure 6.1: Mouse coronal brain slices in aCSF

Loading Protocol: In this study, our first-iteration prototype of the pressure apparatus (discussed in chapter 3) was used to expose the brain slices to a fast-varying pressure profile, similar to an intracranial pressure profile induced by a blast exposure [5, 6, 29, 107]. After obtaining all the brain slices, the slices were transferred to the pressure chamber of the apparatus (shown in figure 6.2).

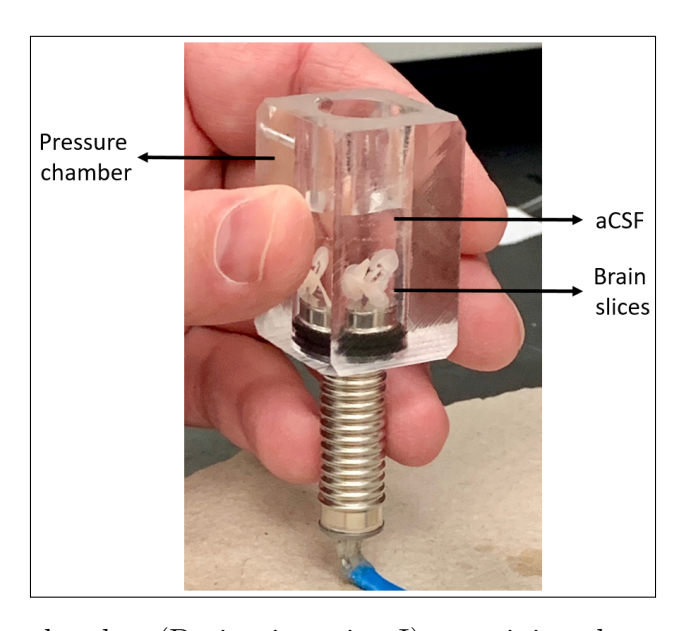


Figure 6.2: Pressure chamber (Design iteration I) containing the mouse brain slices in an aCSF environment

The same aCSF was also used as the pressure chamber fluid. The pressure chamber filled with the aCSF was then closed and sealed using the end-cap. The actuator and the pressure chamber assembly was then held together and pre-compressed using the fixture made of acrylic plates and threaded rods. The experimental apparatus containing the mouse brain slices is shown in figure 6.3. After pre-compression, the brain slices were exposed to sinusoidal pressure loading of 250 kPa amplitude and 3 kHz frequency for a 7 ms duration. The measured pressure loading profile is shown in figure 6.4. This pressure profile has a similar magnitude and dynamics compared to the intracranial pressure profiles observed during a bTBI event.

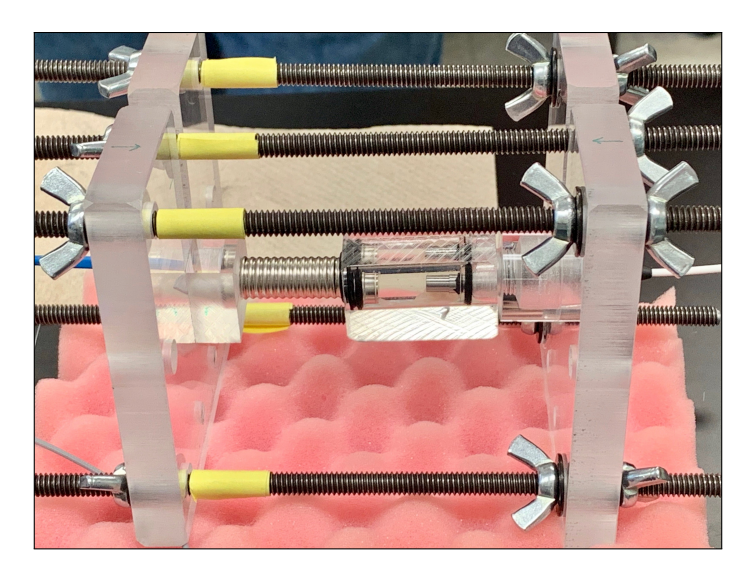


Figure 6.3: Pressure apparatus (Design iteration I) with the mouse brain slices placed inside the chamber

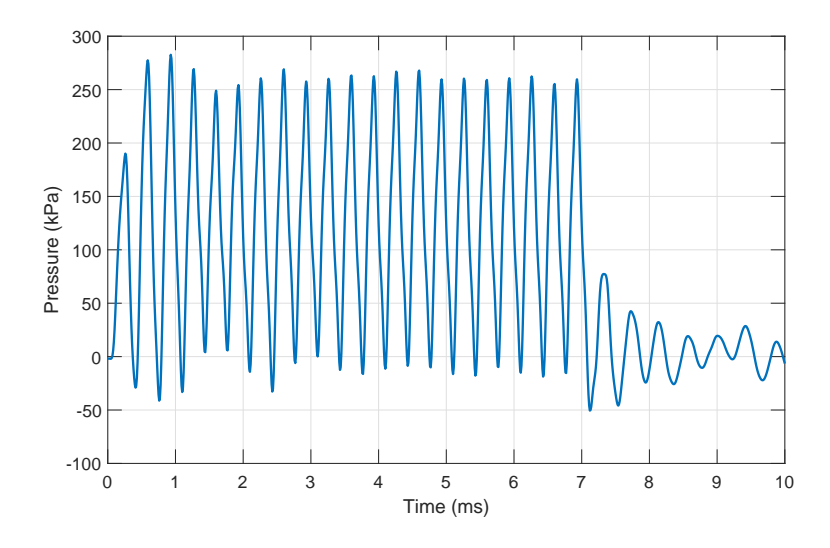


Figure 6.4: Pressure loading profile exerted onto the mouse brain slices

The brain slices were freely floating inside the pressure chamber. As the actuation speed of the piezoelectric actuator ($\approx 0.1 \text{ m/s}$) is several orders of magnitude smaller than the longitudinal wave speed in water ($\approx 1500 \text{ m/s}$), the transient wave propagation effects can be neglected. The pressure generated inside the chamber can be considered as hydrostatic pressure. Thus, irrespective of the location and the orientation of the brain slices, each brain slice was exposed to the same pressure loading.

The duration of each experiment was minimized as much as possible to reduce the stoppage of oxygen flow to the aCSF medium. The duration for each test was around 3 minutes. A total of 4 tests were performed, including a control trial where the brain slices were kept in the pressure chamber but not exposed to the pressure loading.

6.1.1.2 Results

Following the trauma, the slices were incubated for an hour prior to electrophysiological recordings. The procedures followed for the electrophysiological recordings are detailed in [108, 109]. In these recordings, the neurons were excited with current pulses and their response was recorded through the voltage measurements. A representative result obtained from these recordings is shown in figure 6.5.

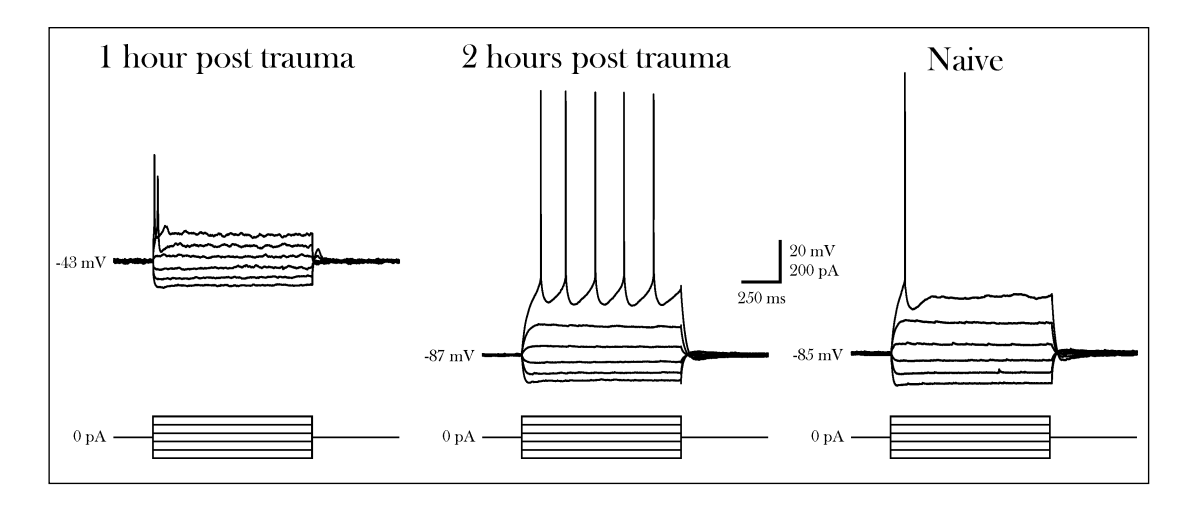


Figure 6.5: Electrophysiological recordings of the mouse brain slices

Initial electrophysiological recordings from layer 5 and layer 2-3 pyramidal neurons revealed depolarized resting membrane potentials (-43 mV compared to -85 mV for neurons from the control or naive slices), decreased input resistance (calculated from the linear slope of the voltage-current relationship), and short broad action potentials (extremely small pulsewidths associated with the neurons' firings). It was noted that recordings one to two hours

after the trauma event appeared to recover to "normal" conditions. These normal conditions were similar to those slices that were either from naive animals or brain slices placed in the pressure chamber but not exposed to the pressure wave (control slices). Our early findings suggest an early trauma to the excitability of the neurons; however, these changes do not appear to be long-lasting.

6.1.2 Ex-vivo Experiments involving Dynamic Shear Loadings

6.1.2.1 Experimental Procedure

Specimen Preparation: B6 mice of either sex were used in these experiments (postnatal age: 25 to 38 days). Animals were deeply anaesthetized with 3% isoflurane and decapitated. The brains were removed and placed into cold (<4°C), oxygenated (95% O₂ and 5% CO₂) aCSF physiological solution containing (in mM): 126.0 NaCl, 26.0 NaHCO₃, 2.5 KCl, 1.25 NaH₂PO₄, 2.0 MgCl₂, 2.0 CaCl₂, and 10.0 glucose. Brains were blocked coronally and glued caudal side down on the bottom plate of the shear apparatus (Design iteration II).

Loading Protocol: The second-iteration prototype of our shear apparatus (discussed in chapter 5) was used to exert dynamic shear loads on the brain tissue specimens. The specimens were glued to the bottom-plate of the shear apparatus. The top-plate was precisely lowered using the translation stage and the micrometer to apply a 10% uniaxial compression onto the specimens, which ensured the contact between the top-plate and the specimens throughout the shear loading cycles. The stickiness of the brain tissue specimens and the applied pre-compression were sufficient to prevent the slippage between the top-plate and the specimens, eliminating the need of gluing the specimen to both the plates, which significantly simplified the tissue handling process. After pre-compression, the specimens were

loaded with sinusoidal shear strain profile of 50 Hz frequency for a duration of 1s (total 50 loading cycles). The specimens were loaded at two amplitude levels: 10% and 20% shear strain. These dynamic shear loadings mimic the low strain amplitudes and high strain-rates shear deformation associated with traveling intracranial shear waves [10]. For the control tests (0% shear strain amplitude), the specimens were pre-compressed but not exposed to any shear loadings. The measured shear strain profiles for the 10% and 20% shear amplitude tests are shown in figure 6.6 (the first 10 out of the total 50 loading cycles are shown).

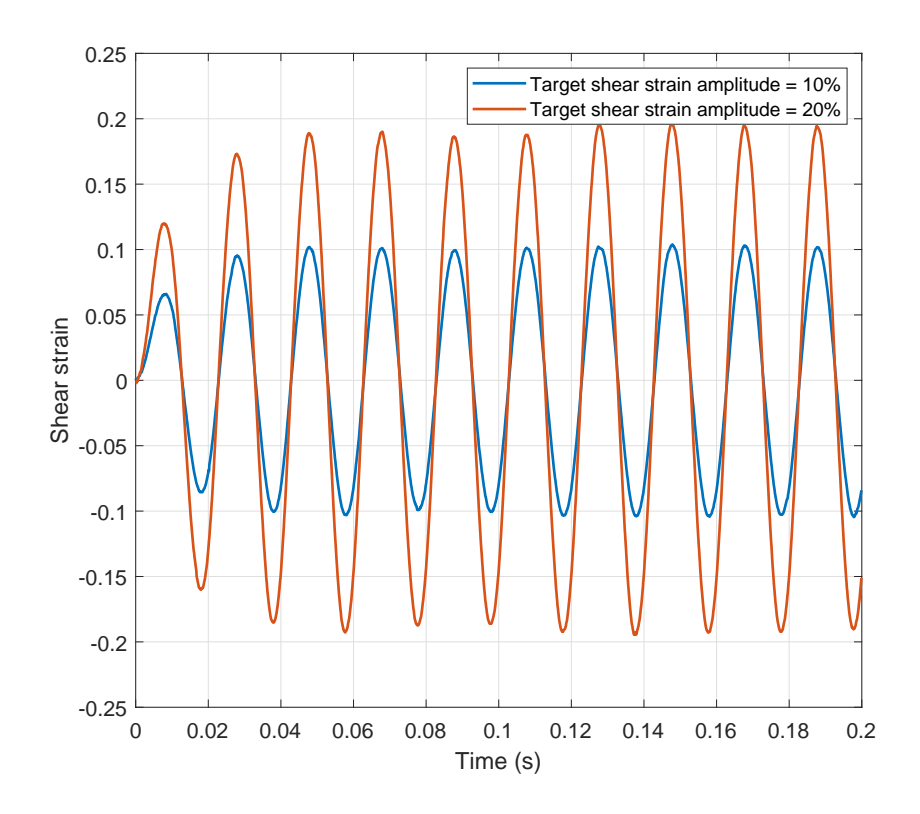


Figure 6.6: The shear strain profiles (loading frequency: $50 \,\mathrm{Hz}$; shear strain amplitudes: 10% and 20%) exerted onto the brain tissue specimens (the first 10 out of the total 50 loading cycles are shown)

A high-speed camera (Model Phantom V2512) was also used to capture brain specimens' deformation at 4000 frames per second. The high-speed images were used to visually verify the simple-shear deformation of the brain specimens and examine if there is any slippage

between the parallel plates and the brain tissue specimens. However, high-speed images were not used for any strain measurements as the top-plate displacement data was sufficient to determine the shear stains. As an illustration, the undeformed state (0% shear strain) of the brain tissue specimen and the deformed state with 20% shear strain are shown in figures 6.7a and 6.7b, respectively.

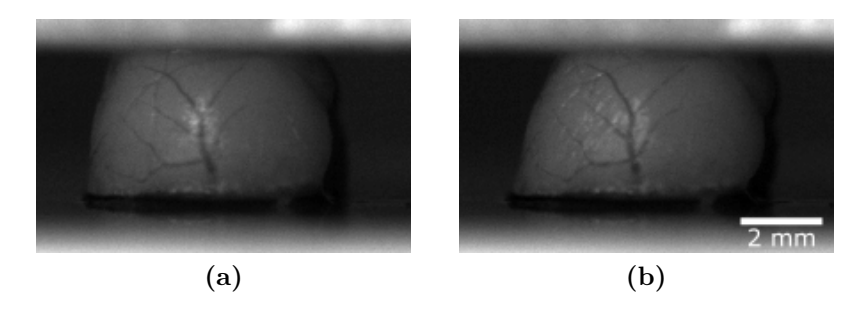


Figure 6.7: High-speed images of the brain tissue specimen under dynamic shear loads: (a) undeformed state (0% shear strain) and (b) deformed state (20% shear strain)

Brain Slice Preparation: Following the shear loads, the brains were placed in cold (<4°C), oxygenated (95% O₂ and 5% CO₂) slicing solution containing (in mM): 2.5 KCl, 26 NaHCO₃, 1.25 NaH₂PO₄, 10.0 MgCl₂, 2.0 CaCl₂, 234.0 sucrose, and 11.0 glucose. Coronal slices (300 μm thickness) at the level of the primary somatosensory cortex [106] were cut using a vibrating tissue slicer. The slices were incubated in oxygenated (95% O₂ and 5% CO₂) physiological solution containing (in mM): 126.0 NaCl, 26.0 NaHCO₃, 2.5 KCl, 1.25 NaH₂PO₄, 2.0 MgCl₂, 2.0 CaCl₂, and 10.0 glucose at 36 °C for at least 30 minutes, then kept at room temperature for the remainder of the experiment. Electrophysiological recordings were performed an hour following decapitation in a recording chamber that was maintained at 32 °C, and slices were continuously superfused (2.5 ml/min) with physiological solution.

Electrophysiology: Whole-cell intracellular recordings were obtained from layer 5 pyramidal neurons of the primary somatosensory cortex (barrel cortex). The procedures followed for the electrophysiological recordings are detailed in [108, 109]. Recordings pipettes were pulled from borosilicate glass and had tip resistances of 4-6 MΩ when filled with a solution containing (in mM) 117.0 K-gluconate, 13.0 KCl, 1.0 MgCl₂, 0.07 CaCl₂, 0.1 EGTA, 10.0 HEPES, 2.0 Na-ATP, and 0.4 Na-GTP. The pH and osmolarity of the internal solution were adjusted to 7.3 and 290 mOsm, respectively. Recordings were obtained using a Multiclamp 700B amplifier (Molecular Devices, Sunnyvale, CA). An 8 mV junction potential was corrected for in all voltage measurements. Signals were digitized at 10 kHz and stored for subsequent analyses using pCLAMP software (Molecular Devices).

Input resistances were calculated from the linear slope of the voltage-current relationship obtained by applying constant current pulses ranging from -40 to +40 pA (1 s duration). The time constant measurements were obtained from a small hyperpolarizing (-10 pA) short duration (100 ms) current pulse. Action potential output for a single neuron was obtained by applying constant current pulse ranging from 0 pA to 1600 pA by 40 or 80 pA intervals for 1 second. Action potential frequency versus intensity curves (F-I curves) were then generated from the collected data. Summarized data is expressed as mean \pm standard deviation. P-values less than 0.05 were considered statistically significant.

6.1.2.2 Results

Intrinsic Properties: Whole-cell current-clamp recordings were used to measure the three intrinsic neuronal properties: (1) resting membrane potential, (2) input resistance, and (3) time constant. These three intrinsic properties were used as indicators of cell health following the three different shear strain conditions: (a) 0% shear strain (control), (b) 10% shear strain,

and (c) 20% shear strain.

Resting membrane potential measurements give insight into the neurons' level of excitation. Resting membrane potential measurements were not significantly different between the shear strain conditions tested (one-way ANOVA, p>0.05). Neurons exposed to 0% shear strain possessed an average resting membrane potential of -75.5 ± 4.1 mV (5 cells from 1 animal, shown in figure 6.8 (Black)). While neurons exposed to 10% shear strain possessed an average resting membrane potential of -69.0 ± 11.1 mV (8 cells from 1 animal, shown in figure 6.8 (Blue)) and neurons exposed to 20% shear strain possessed an average resting membrane potential of -71.0 ± 12.5 mV (10 cells from 2 animals, shown in figure 6.8 (Red)).

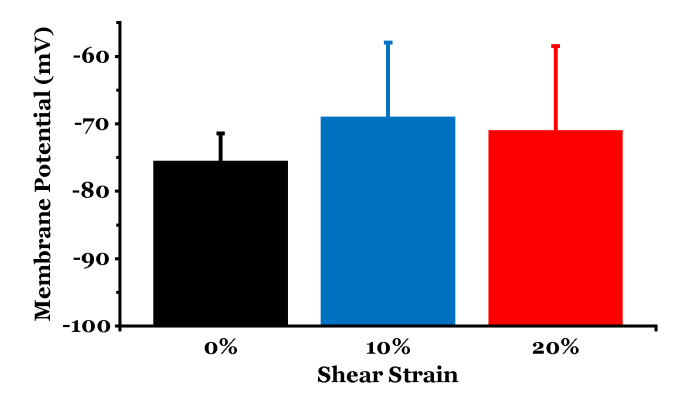


Figure 6.8: Change in electrophysiological resting membrane potential of neurons resulting from dynamic shear loadings of various strain amplitudes

Input resistance measurements reflect the neurons' sensitivity to incoming electrical signals. Input resistance measurements were not significantly different between the shear strain conditions tested (one-way ANOVA, p>0.05). Neurons exposed to 0% shear strain displayed an average input resistance of 64.1 \pm 39.1 M Ω (7 cells from 1 animal, shown in figure 6.9 (Black)). While neurons exposed to 10% shear strain displayed an average input resistance of 111.4 \pm 63.9 M Ω (8 cells from 1 animal, shown in figure 6.9 (Blue)) and neurons exposed to 20% shear strain possessed an average input resistance of 69.5 \pm 41.3 M Ω (10 cells from 2 animal, shown in figure 6.9 (Red)).

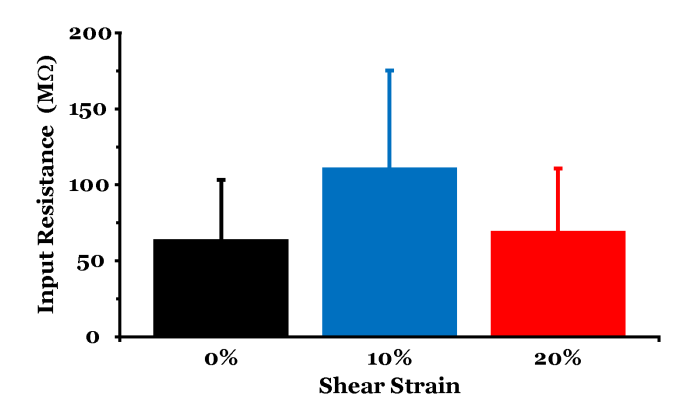


Figure 6.9: Change in electrophysiological input resistance of neurons resulting from dynamic shear loadings of various strain amplitudes

Time constant measurements provide insight into the neurons' membrane capacitance and membrane resistance. The time constant measurements were not significantly different between the shear strain conditions tested (one-way ANOVA, p>0.05). Neurons exposed to 0% shear strain had an average time constant of 13.0 ± 4.1 ms (7 cells from 1 animal, shown in figure 6.10 (Black)). While neurons exposed to 10% shear strain had an average time constant of 18.7 ± 11.1 ms (8 cells from 1 animal, shown in figure 6.10 (Blue)) and neurons exposed to 20% shear strain had an average time constant of 17.1 ± 5.2 ms (8 cells from 2 animal, shown in figure 6.10 (Red)).

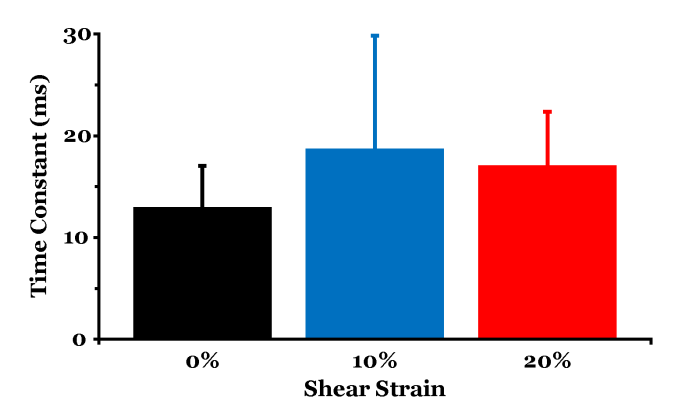


Figure 6.10: Change in electrophysiological time constant of neurons resulting from dynamic shear loadings of various strain amplitudes

Overall, none of the intrinsic properties measured showed any significant difference be-

tween the specimens exposed to dynamic shear loads of various strain amplitudes and the control specimens. These results suggest that these dynamic shear loadings do not produce an acute (< 12 hours) effect on the intrinsic cell health of layer 5 pyramidal neurons of the mouse barrel cortex.

Action Potential Output: Whole-cell current-clamp recordings were used to measure the action potential output of the neurons tested. Frequency of action potential firing versus current injected curves (F-I curves) were averaged for the three different shear strain conditions: 0% shear strain (control) n=4, 10% shear strain n=5, and 20% shear strain n=8. These curves are shown in figure 6.11.

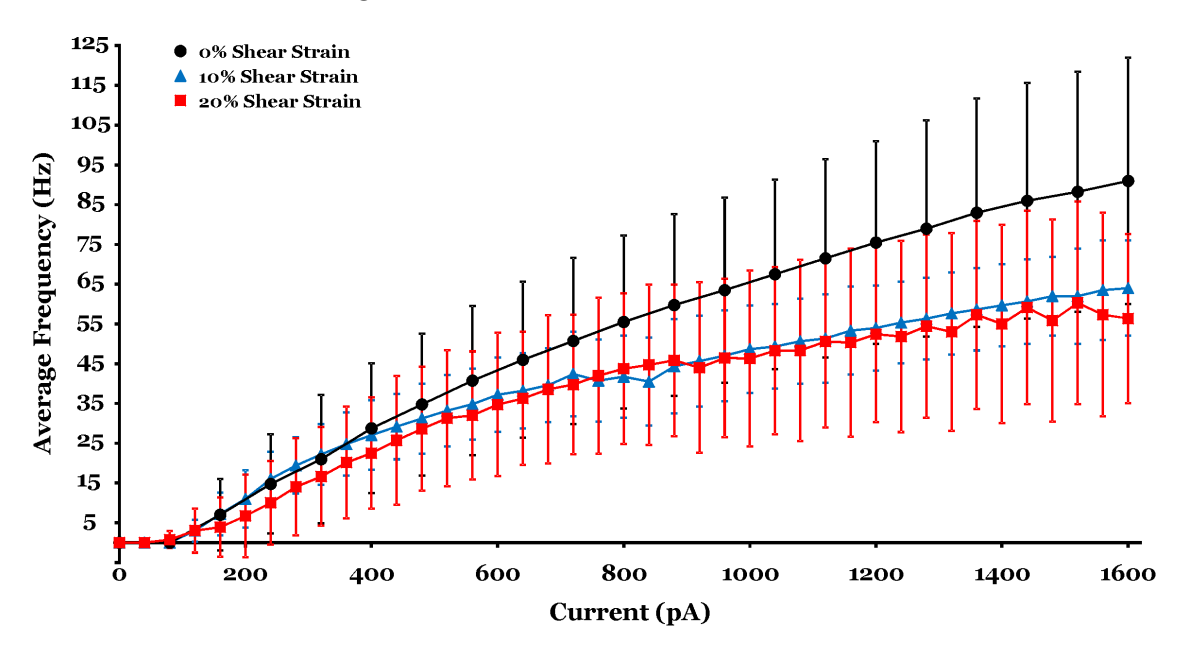


Figure 6.11: Frequency of neuronal action potential firing versus current injected curves (F-I curves) for three dynamic shear loading conditions

On average higher current injections in control (0% shear strain) neurons tended to result in higher firing rates than the two shear strain conditions (10% shear strain and 20% shear strain). 0% shear strain neurons had an average maximum frequency of 91 \pm 31 Hz, while 10% shear strain was 64 \pm 12 Hz and 20% shear strain was 60 \pm 25 Hz. These sample

sizes are relatively small, and more samples will be needed for statistical analysis. However, these results suggest there may be an acute reduction of action potential output of layer 5 pyramidal neurons of the mouse barrel cortex following dynamic shear loads.

6.2 *In-vitro* Experiments

This section discusses the preliminary *in-vitro* experiments involving HeLa (Henrietta Lacks) cell cultures and cerebral organoids. The HeLa cell culture experiments were performed in collaboration with the Center for Applied Genomics (CAG) at Children's Hospital of Philadelphia. The cell culture preparation and post-exposure analysis for the tests were performed by Dr. Michael March at CAG. These tests are discussed in section 6.2.1. The *in-vitro* experiments involving cerebral organoids were performed in collaboration with Dr. Zane Lybrand's group at Texas Woman's University. The cerebral organoids preparation and post-exposure analysis for the tests were performed by Dr. Zane Lybrand and Nikolas Merlock. The details of these tests are provided in section 6.2.2.

6.2.1 In-vitro Experiments involving HeLa cell cultures

6.2.1.1 Experimental Procedure

Specimen Preparation: In this study, our first-iteration prototype of the pressure apparatus (discussed in chapter 3) was used to expose HeLa cell cultures to fast-varying pressure profiles of various amplitudes and frequencies. HeLa cells (immortalized cervical carcinoma cell line) were grown on 12 mm #2 thickness glass coverslips. For easy handling of the glass coverslip in and out of the pressure chamber, a semi-circular cylindrical plug made of 2% weight/volume concentration agarose gel was used to support the glass coverslip. The glass

coverslip placed inside the pressure chamber (Design iteration I) with the agarose gel support is shown in figure 6.12. The pressure chamber was filled with the cell-culture media buffer solution.

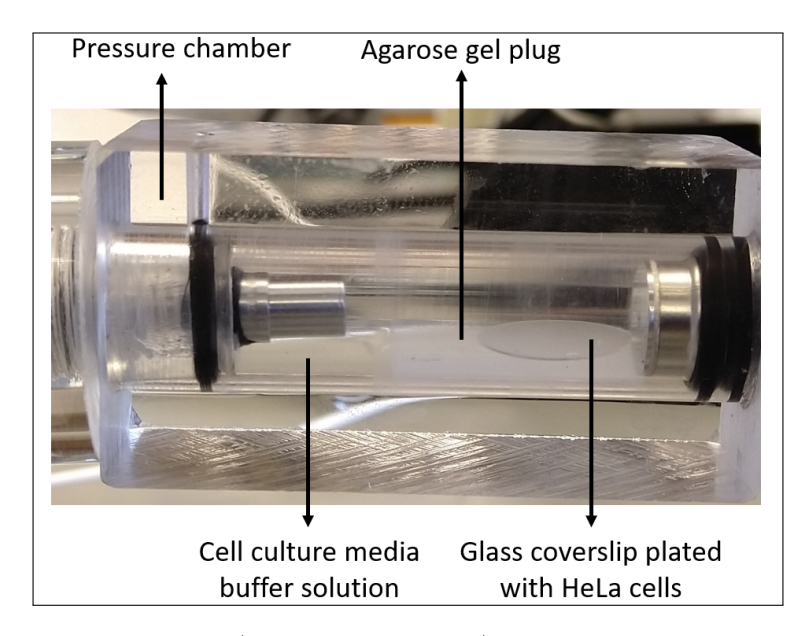


Figure 6.12: Pressure chamber (Design iteration I) containing a glass coverslip plated with HeLa cells

Loading Protocol: In order to test the response of living cells to various frequencies and pressure levels of a blast exposure, HeLa cells were exposed to high-frequency pressure waves having magnitudes of 120 kPa and 250 kPa and frequencies of 500 Hz, 1 kHz, and 3 kHz for a duration of 8 ms. The parametric details of all these loading cycles are given in table 6.1. A total of 4 sets of loading tests were performed, where each set included the 8 loading protocols. After loading the coverslips, they were incubated until further analysis.

6.2.1.2 Results

To quantify the cell death, lactate dehydrogenase (LDH) cytotoxicity assays (CyQUANT LDH Cytotoxicity Assay, Thermo Fisher Scientific) were performed on the coverslips. The

Table 6.1: Loading protocols for *in-vitro* experiments involving HeLa cell cultures

Loading Protocol	Pressure Amplitude (kPa)	$\begin{array}{c} {\rm Frequency} \\ {\rm (Hz)} \end{array}$	Loading Time (ms)
LP1	250	500	8
LP2	120	500	8
LP3	250	1000	8
LP4	120	1000	8
LP5	250	3000	8
LP6	120	3000	8
LP7	120	500, 1000, and 3000	10
Control	-	-	-

LDH cytotoxicity assay measures the release of a cytoplasmic enzyme into culture supernatant as a measure of cell death. These assays were performed on two different sets of coverslips after 6 hrs and 24 hrs from the exposure. The percent specific release obtained from the LDH cytotoxicity assays as a measure of cell death for all the loading protocols is shown in figure 6.13. It can be observed that the specific release measured after 6 hrs from the exposure is significantly higher than the one measured after 24 hrs. This result again suggests a time-dependent response of the cells to the pressure loadings.

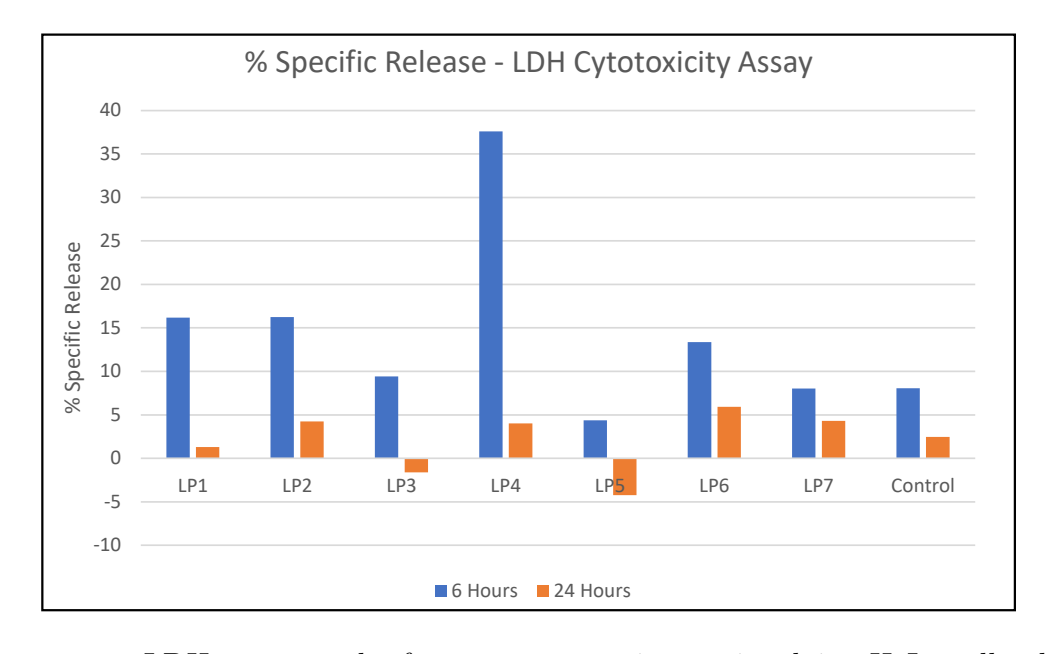


Figure 6.13: LDH assay results for *in-vitro* experiments involving HeLa cell cultures

Another method called "Dead-Green" staining (Image-IT DEAD Green Viability Stain, Thermo Fisher Scientific) was also used to quantify cell death. This staining method is detailed in [110]. The "Dead-Green" staining uses a cell-impermeable dye that cannot enter live cells but stains cells with damaged membranes green. Thus, by calculating the percentage of the green stained area, cell death can be quantified. The "Dead-Green" staining was performed on another set of coverslips 3 hours after the exposure, and results are shown in figure 6.14.

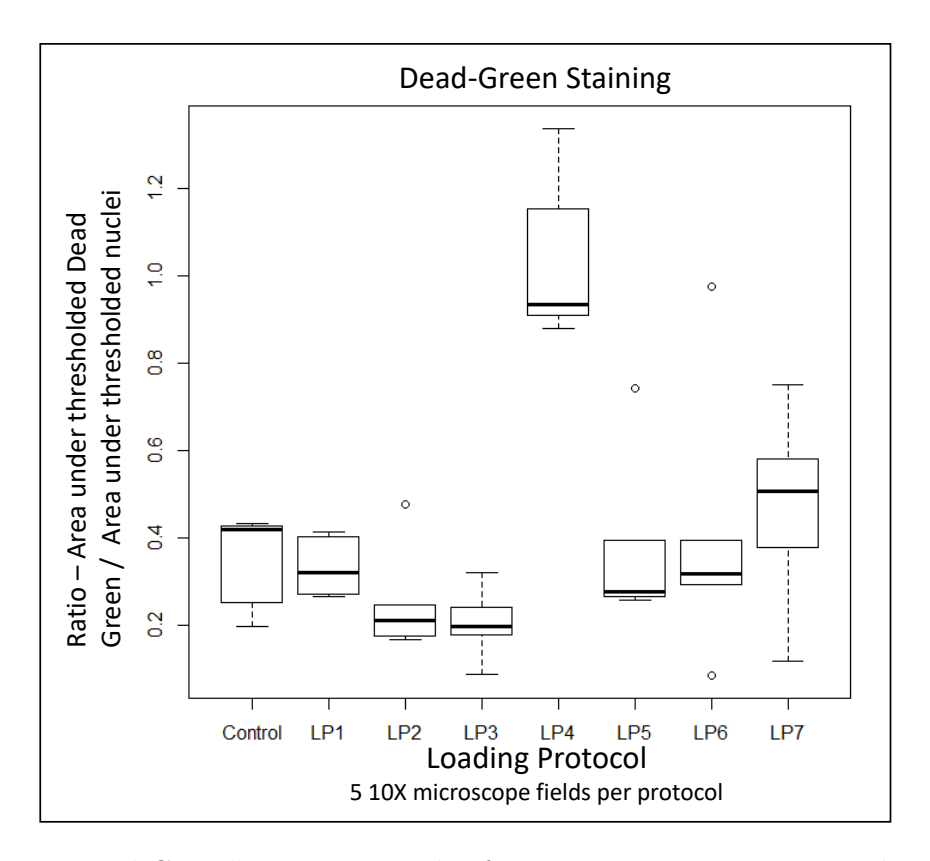


Figure 6.14: "Dead-Green" staining results for *in-vitro* experiments involving HeLa cell cultures

It was observed from both LDH cytotoxicity assay and the "Dead-Green" staining that LP4 induced maximum damage to cells compared to the other loading protocols. Even though LP3 loaded the cells with higher pressure amplitude than LP4 at the same loading frequency, LP4 induced greater damage to the cells than LP3. These results appeared to be

counter-intuitive. To gain confidence in these experimental findings, the same experiments were repeated. However, the results did not support the initial findings. One of the possible reasons for this discrepancy could be the robustness of the HeLa cells. HeLa cells, which is an immortalized cervical carcinoma cell line, are lab-grown and very robust compared to neuronal cell lines. Thus, there could be a very low signal to noise ratio when the mechanical damage was assessed on the HeLa cells. However, further experimentation is necessary to test this hypothesis.

6.2.2 In-vitro Experiments involving Cerebral Organoids

6.2.2.1 Introduction

Cerebral organoids are 3D structured cultures of human astrocytes and neurons which have a similar organization and physiology to human neuronal networks found in the cerebral cortex [111]. These organoids also exhibit the complex oscillatory electrical currents - analogous to brain waves [112]. Additionally, these organoids can survive for long durations of time to follow chronic changes (as well as acute) after a traumatic brain injury (TBI) event.

Cerebral organoids develop brain architecture found in the human cortex: Cerebral organoids are grown by dissociating into single cells and plating to form embryoid bodies (EB). Following a dual SMAD inhibition protocol [111,113] for neural induction, two types of spheroids are grown from EBs, cortical and subpallial spheroids. As represented in neural development, excitatory glutamatergic neurons are generated from the cortical plate, which is later infiltrated by migrating inhibitory interneurons from the medial ganglionic eminence of the subpallium. To replicate this process, both cortical and subpallial spheroids are generated using FGF2 and EGF to generate neural progenitors, followed by BDNF and NT3 to

promote neuronal differentiation. To pattern subpallial spheroids, WNT and SHH pathways are modulated using IWP-2 and SAG. Once cortical and subpallial spheroids are patterned, the two are fused to generate complete cortical grafts (shown in figure 6.15A). The human cortex is organized into identifiable layers based on cells found in each layer. The same organization and cell populations are identified in human cerebral organoids (shown in figure 6.15B). Early-stage cortical spheroids (30 DIV) express distinguishing laminar markers for deep and superficial cortical layers. In cortical spheroids, from 70-180 DIV, we observed TBR1 and CTIP2 expression in deep layer neurons, SATB2 and BRN2 in upper-layer neurons, and HOPX and FAM107, markers from outer radial glial cells (shown in figure 6.15C). Importantly, cerebral organoids also generate cells essential to maintain the health of the local brain environment. This includes the ventral zone (VZ) to form internal ventricles, glial cells like astrocytes, and oligodendrocytes (shown in figure 6.15D). Altogether, these cerebral organoids can be grown to generate the critical cells and organization found in the human cortex.

Cerebral organoids generate functional brain networks similar to the human cortex: Using multielectrode arrays (MEA), fused cerebral organoids that display complex neural networks (shown in figure 6.16a) are plated on top of a 12-electrode grid, and electrical neuronal activity can be measured (shown in figure 6.16b). From this MEA data, specific neuronal activity is recorded and measured (shown in figure 6.16c). These events represent extracellular action potentials, or spikes, that originate from neurons of the organoid located in proximity to an electrode (shown in figure 6.16c bottom). The electoral neuronal activity can further be filtered in the 9-14 Hz bandwidths to identify the network oscillations (seen in figure 6.16d) and measure the synchrony across multiple electrodes. These network oscil-

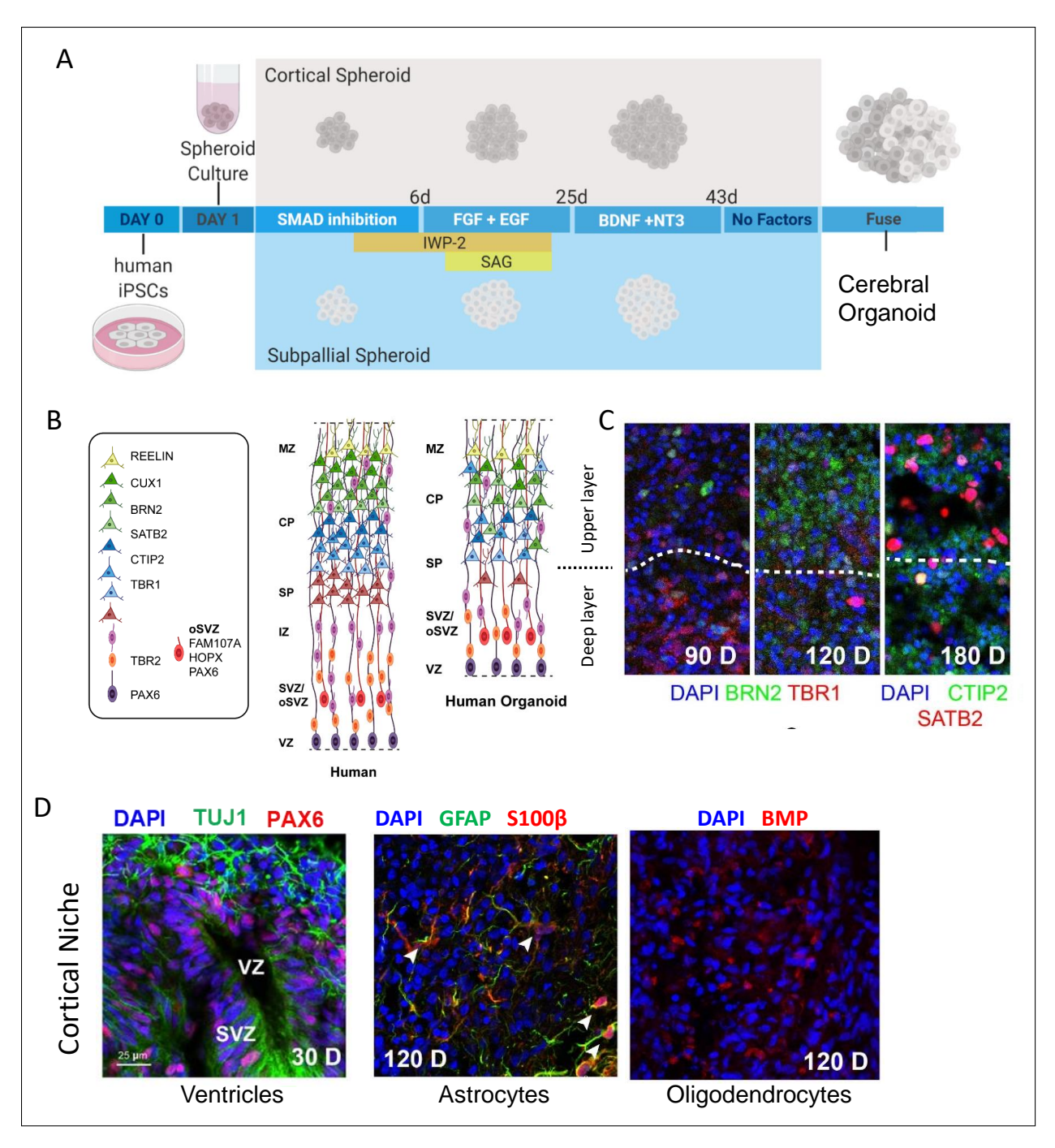


Figure 6.15: Cerebral organoids reproduce human cortical organization. (A) Timeline for stem cell protocol to grow cerebral organoid. (B) Compared to the human cortex, cerebral organoids contain most of the same layered organization and cells present. (C) Characterization of cortical structure from deep and upper-layer neurons in developing cortical spheroid (dotted line). (D) Image of the ventricular zone (VZ), astrocytes, and oligodendrocytes that form a support niche.

lations are reminiscent of cortical brain waves measured using electroencephalogram (EEG) in human patients (shown in figure 6.16d).

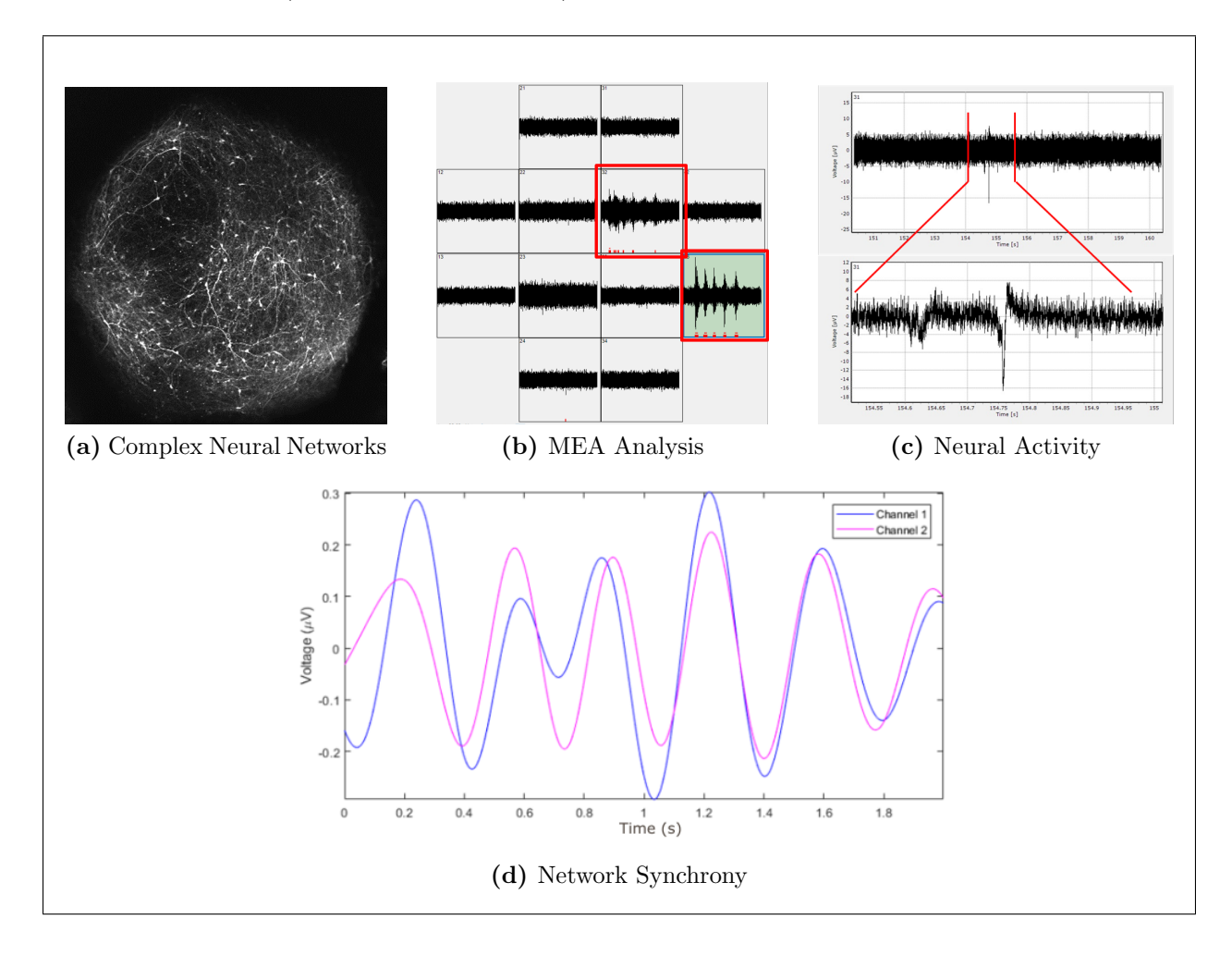


Figure 6.16: Neurophysiology of the cerebral organoids. (a) Cerebral organoid displaying a complex network of neurons. (b) Multielectrode array (MEA) measures 12 channels from each organoid. (c) Neural activity is measured from the MEA. The bottom image is a magnified time scale of the voltage signal recorded in the top image. (d) The raw signals can be filtered, and network oscillations are measured to determine the synchrony of activity recorded in cerebral organoids.

In this study, the second-iteration prototype of our pressure apparatus (discussed in chapter 3) was used to expose cerebral organoids to a fast-varying pressure profile, similar to an intracranial pressure profile induced by a blast exposure. The pressure chamber of the apparatus was filled with culture media along with the organoids, where a piezoelectric

actuator compressed the liquid rapidly, generating high-pressure fluctuations with controlled pressure amplitude and frequency. Following exposure, cerebral organoids were monitored for neurophysiological properties immediately after exposure (1 hour) and 24 hours later. We measured an increase in neuronal activity 1 hour after exposure and an increase in the synchronization of network function. These results demonstrate that in response to the specific pressure parameters, cerebral organoids' physiology changes.

6.2.2.2 Experimental Procedure

To determine if cerebral organoids respond to pressure forces similarly observed in a blast injury, 60 days old fused cerebral organoids were loaded into the pressure apparatus. The timeline for the tests is shown in figure 6.17a. Briefly, the blast chamber (shown in figure 6.17b) was filled with organoid growth media (orange), and organoids for each group were placed inside. Later the chamber was closed off without introducing any bubbles within the chamber. The pressure apparatus was then set and activated to deliver a 3 kHz frequency waveform that reached 250 kPa pressure (shown in figure 6.17c). Immediately following pressure exposure, cerebral organoids were removed and plated on a pre-warmed MEA plate (shown in figure 6.17d) where they were positioned on the electrode grid (shown in figures 6.17e and 6.17f). For control tests, cerebral organoids were placed inside the pressure chamber, but the piezoelectric actuator was not activated. Once all organoids were plated, the MEA plate was incubated until 1 hour after the blast exposure. At that time, an initial 2 minutes recording was acquired, and the MEA was returned to incubation over night at 37°C with 5% CO₂. The next day at 24 hours post-blast, the MEA plate was removed from the incubator, and another 2 minutes MEA recording was acquired.

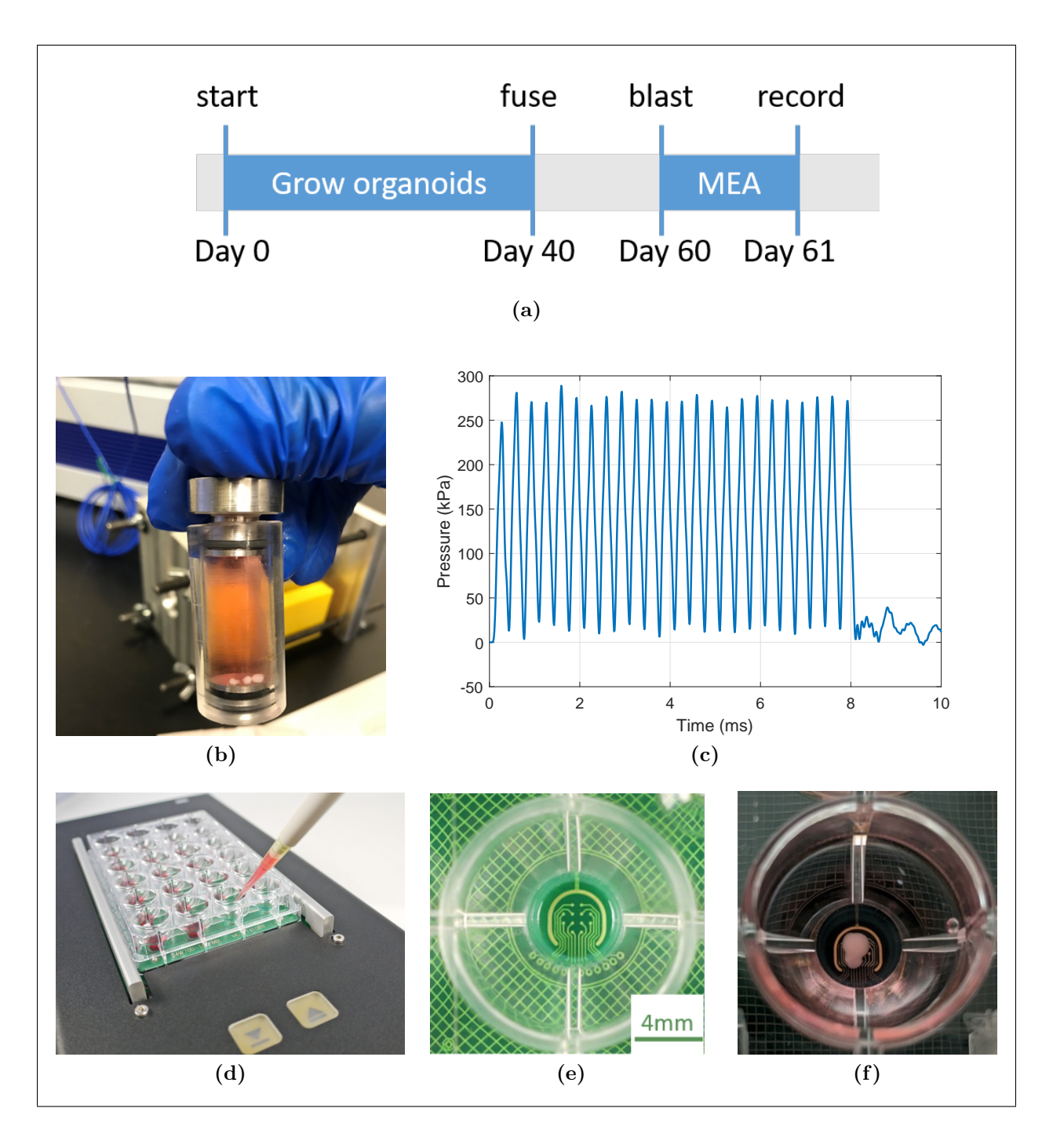


Figure 6.17: Blasting cerebral organoids. (a) Timeline of blast experiment (b) Image of 3 cerebral organoids inside of pressure chamber. (c) The pressure waveform recorded inside the chamber during the exposure (Amplitude = 250 kPa, Frequency = 3 kHz, and duration = 8 ms). (d) 24 well plate being loaded with organoids after being blasted. (e) Empty MEA well showing the layout of 12 electrodes. (f) MEA well filled with media and cerebral organoid on electrodes.

6.2.2.3 Results

Extra-cellular action potentials were quantified between no blast controls (n=3) and blast organoids (n=3) as shown in figures 6.18a and 6.18b. Over 120 seconds, the total number of spikes (shown in figure 6.16c bottom) were quantified. Raster plots in figures 6.18a and 6.18b show events over the 120s recording displayed for each of the 12 channels. One hour after the exposure, there was a modest increase in the amplitude of the spike (shown in figure 6.18c) and frequency (shown in figure 6.18d) compared to no blast controls. Interestingly, by 24 hours, this emerging difference was no longer present.

To determine if the increase in spike frequency measured at 1 hr post-blast resulted in a population-level change of neural network function, the phase synchrony was measured using a 5 Hz filter (shown in figure 6.19). In control organoids, spontaneous 5 Hz oscillations are unsynchronized (shown in figure 6.19a). This is seen by a low degree of phase angle difference measured between two channels of the MEA (shown in figure 6.19b). Following blast exposure, organoid networks were observed to become more synchronized (shown in figure 6.19c) as measured by the average length of phase synchronization (shown in figures 6.19d and 6.19e). In the phase synchronization chart shown in figure 6.19e, the phase synchronization length of 1 indicates a highly synchronous network, while the phase synchronization length of 0 indicates network without any synchrony. The typical phase synchronization length for a human EEG is between 0.2 and 0.5.

Together these results suggest that the blast parameters testing with the pressure apparatus is capable of acutely altering neuronal function and network synchrony. Further testing will expand parameter space and be used to investigate the cell and molecular biology of blast and blunt forces on complex neural networks.

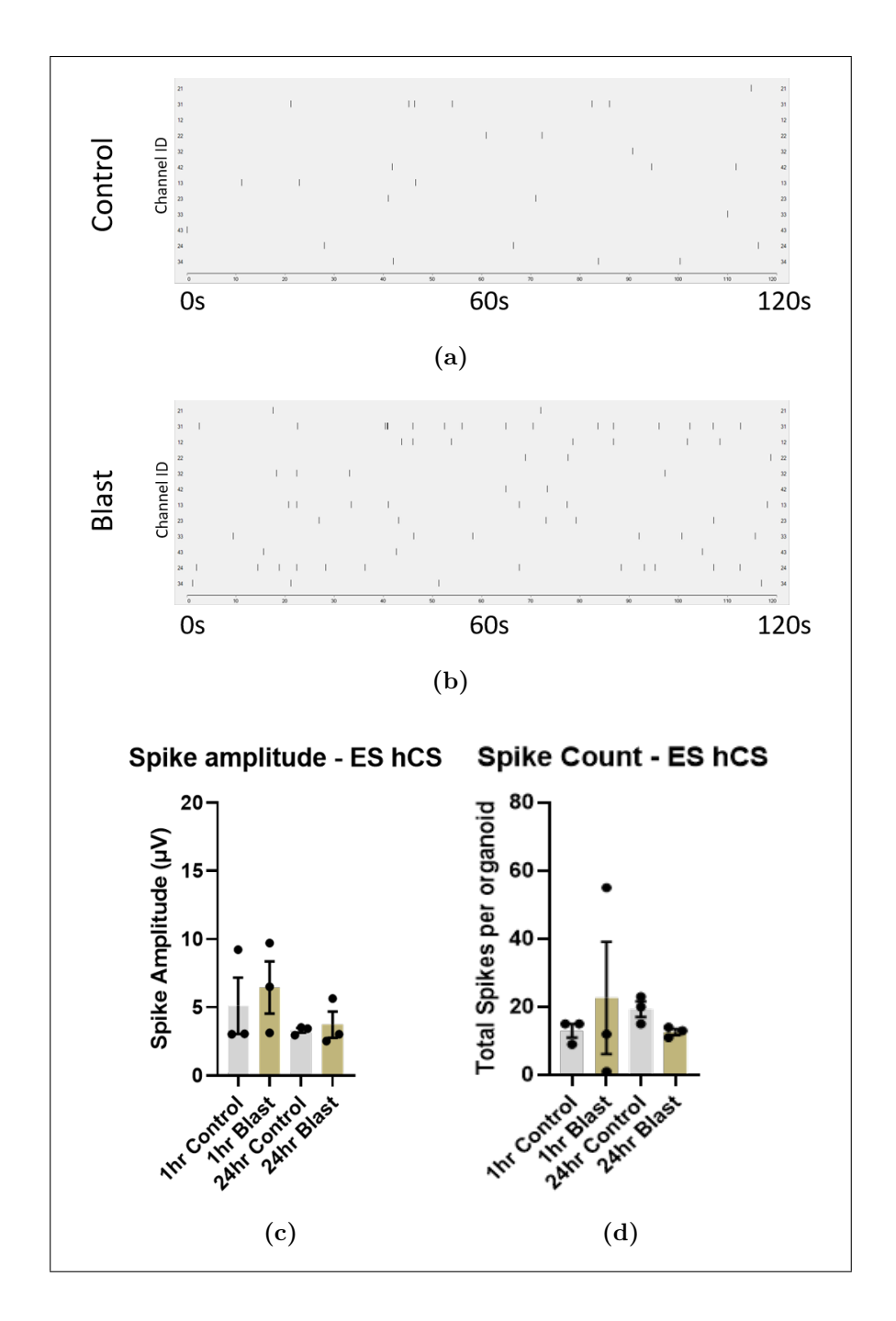


Figure 6.18: Blast acutely stimulates cerebral organoids. (a) Raster plot of spike events recorded from MEA in no blast control organoids. (b) Raster plot of spike events recorded from blast group at 1 hr post-blast. (c) Quantification of spike amplitudes in 1 hr and 24 hr post-blast organoids. (d) Quantification of spike number in cerebral organoids.

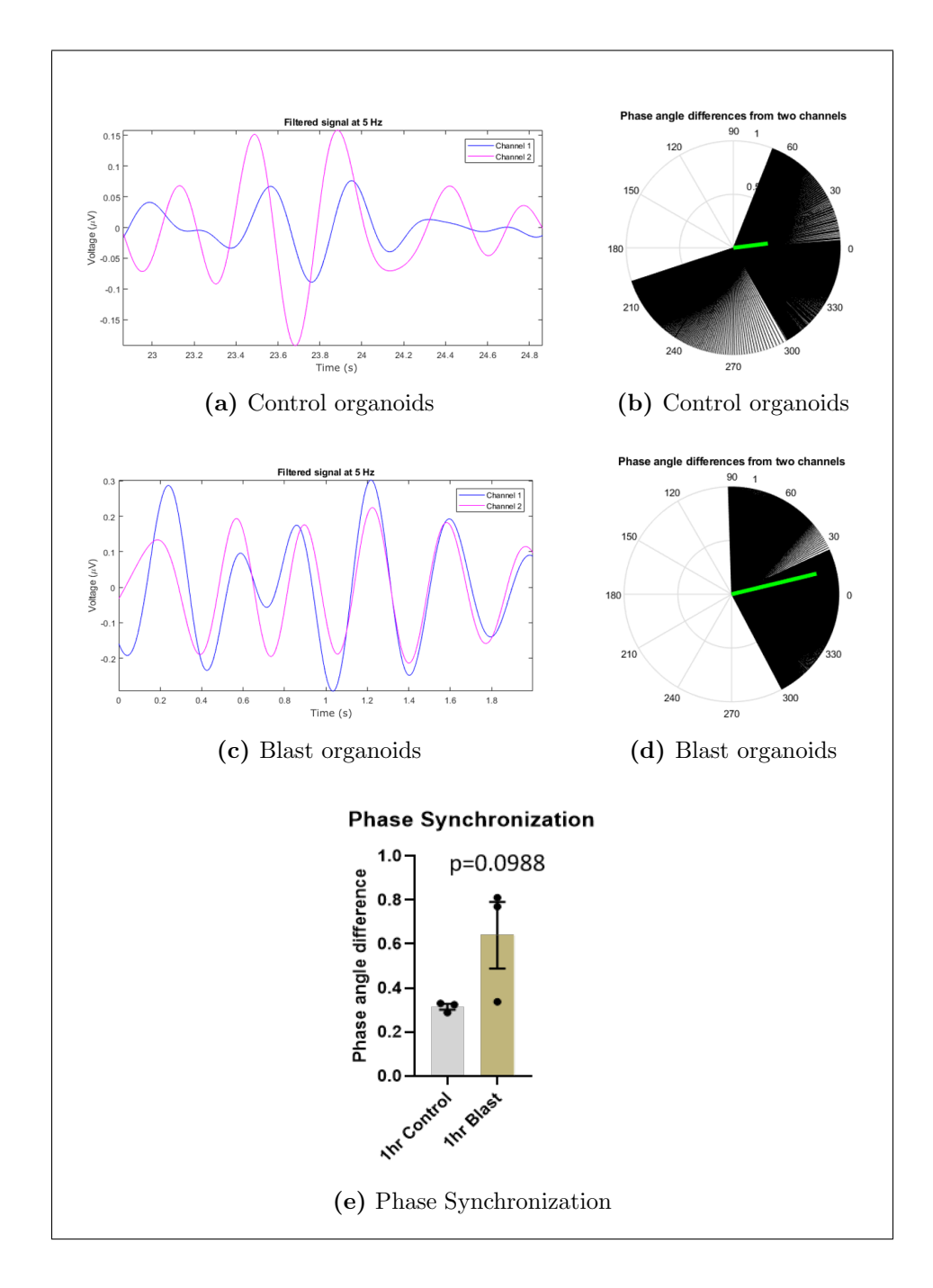


Figure 6.19: Blast acutely increases network synchrony. (A) Two channels with raw signal filtered using a 5 Hz Morlet Wavelet from control organoids. (B) The phase angle difference plotted for each time unit between two channels (black), and the average angle and phase synchronization plotted (green bar) from control organoids. (C) Filtered channels from blast organoids. (D) Plot of phase angle difference (black) and average phase synchronization (green) plotted from blast organoids. (E) Quantification of phase synchronization between the control and blast organoids at 1 hr post-blast. (n=3 organoids per group; p-values less than 0.05 is considered statistically significant)

Chapter 7

Future Directions

This chapter summarizes the development of the experimental systems designed for bTBIrelated *ex-vivo* and *in-vitro* studies, and also provides directions for future advancements.

7.1 Future Directions for the MMHB Actuator

The MMHB actuator discussed in Chapter 2 replaces the incident bar of a conventional split-Hopkinson pressure bar apparatus with a multi-material incident bar to transform the incident stress pulse into a complex loading profile. The design parameters for an MMHB actuator, such as the materials and lengths of bar components, are adjusted so as to closely replicate the user-defined target loading profile. This is achieved by coupling the numerical simulation of the MMHB actuator with an optimization algorithm. As proof of concept, the MMHB actuator was designed for generating various sinusoidal pressure profiles with multi-frequencies and decaying characteristics.

The designed MMHB actuator could reasonably replicate the dynamics of specified twofrequency target profiles. Increasing spectral complexity of the target pressure profiles resulted in a relatively higher deviation between the target and generated pressure profiles, pointing to the necessity of increasing the number of material bars in the design space. However, as the number of bar components used to construct the multi-material incident bar increases, the total length of the actuator will increase as well. This increased length of the actuator may limit its applicability because of the laboratory space or experimental constraints. A strategy to be considered in the future is to use a parallel combination of several multi-material bars to replicate a multi-frequency pressure profile better than a single multi-material bar. While a strategy like this could have more flexibility than single multi-material bars, its implementation will bring new challenges.

The numerical model of the MMHB actuator treats water as a nearly incompressible linear-elastic fluid. This model does not incorporate the compressibility of water and the cavitation phenomenon. Cavitation can saturate the negative pressure part of the pressure loadings generated by the MMHB actuator. Thus, a more specific equation of state for the water constituent that accounts for pressure-density variations and cavitation phenomenon [5] should be considered in the future.

7.2 Future Directions for the Pressure Apparatus

The generator of broadband pressure cycles discussed in Chapter 3 uses a water-filled piston-cylinder assembly driven by a piezoelectric actuator to generate complex and fast-varying pressure profiles. The apparatus employs a feedforward controller to track user-specified target pressure profiles. The versatility of this apparatus in producing complex pressure profiles was demonstrated by generating a single pressure pulse with various pulse-widths and magnitudes, an approximate Friedlander waveform, and a multi-modal waveform. The apparatus successfully generated pressures up to 450 kPa at frequencies up to 5 kHz. This apparatus was used perform the preliminary ex-vivo and in-vitro experiments discussed in Chapter 6 (sections 6.1.1, 6.2.1, and 6.2.2).

In the future, this pressure apparatus can be scaled to include multiple piezoelectric

actuators. Actuating multiple piezoelectric actuators synchronously to compress the water confined in the pressure chamber should increase the maximum achievable pressure. Moreover, the actuation of the various actuators can be precisely timed to generate even more intricate pressure profiles by leveraging the superposition of multiple pressure profiles. Incorporating multiple actuators can increase the capabilities of the apparatus, but it will further complicate the system and may reduce its usability.

7.3 Future Directions for the Cavitation Rig

The bench-top cavitation rig discussed in Chapter 4 uses a water-filled piston-cylinder assembly which is driven by a high-speed linear motor. The motor is used to retract the piston, increasing the pressure chamber's volume and, consequently, generating a tensile or negative pressure. This negative pressure gives rise to cavitation. The apparatus can generate cavitation events of various durations and intensities. The potential of this apparatus is demonstrated by producing a cavitation event in water.

For the cavitation experiment discussed in Chapter 4, a few micro-bubbles were already present in the pressure chamber before the piston was actuated. Thus, the negative pressures generated by the apparatus ended up expanding these existing micro-bubble rather than creating new cavitation bubbles. In the future, if the focus is to generate new cavitation bubbles in a liquid, deliberate efforts are needed to remove all the pre-existing bubbles from the liquid, which could be achieved using the methods reported in [25, 26, 30].

The curved surface of the pressure chamber cavity creates an optical distortion while imaging the cavitation bubbles due to refraction. This optical distortion creates challenges in analyzing the bubble dynamics based on high-speed images. One way to circumvent this challenge is to design a new pressure chamber with a flat optical window for high speedimaging, similar to the ones reported in [26, 50].

The shock-waves resulting from the collapse of the bubbles sharply increased the pressure inside the chamber. This pressure exceeded well beyond the pressure transducer's rated measurement range, which led to the saturation of the measured pressure profile. Thus, a pressure transducer with a significantly larger pressure range is required to appropriately measure the high pressure associated with the shock-waves.

7.4 Future Directions for the Shear Apparatus

The generator of dynamic shear cycles discussed in Chapter 5 uses a voice-coil actuator and two parallel plates assembly. This apparatus can generate oscillatory shear loadings of various strain amplitudes and frequencies at the levels relevant to bTBI. The first-iteration shear apparatus was used to conduct preliminary material characterization experiments for PAA gelatin specimens. These experiments also tested the implementation of the apparatus for loading samples of living tissue and three-dimensional cell cultures. The insights from these preliminary experiments led to the design improvements implemented in the second iteration of the shear apparatus. The second-iteration shear apparatus employs a PID controller to control the voice-coil actuator and replicates the user-specified shear strain profiles. It was also used to perform bTBI-related ex-vivo experiments on mouse brain tissue specimens (discussed in chapter 6, section 6.1.2).

In the future, this shear apparatus can be scaled to include two voice-coil actuators by replacing the stationary bottom plate with a movable plate actuated by the second voicecoil actuator. Actuating both the actuators synchronously to move the plates in opposite directions should increase the maximum achievable shear strain for a given loading frequency and specimen thickness. Moreover, by precisely timing the motion of the actuators, multi-frequency dynamic loading cycles can be generated through wave superposition. Again, incorporating multiple actuators can increase the capabilities of the apparatus, but it will further complicate the system and may reduce its usability.

As the shear loading frequency increases, the inertial effects inducing the unsteady shear deformation of the specimen increases. The inertial effects are significant when the specimen's thickness is comparable to the elastic shear wavelength in the specimen. In such cases, the specimen's deformation is no longer a simple-shear deformation as the shear strain field is inhomogeneous. Such an inhomogeneous strain field cannot be reliably estimated just from the top-plate displacement data. Furthermore, imaging-based techniques are required to quantify the inhomogeneous deformation of the specimen. Thus, reducing the specimen's thickness as much as possible is a definitive strategy to eliminate the undesired inertial effects.

BIBLIOGRAPHY

BIBLIOGRAPHY

- [1] L. Wang, K. Labibes, Z. Azari, and G. Pluvinage, "Generalization of split Hopkinson bar technique to use viscoelastic bars," *International Journal of Impact Engineering*, vol. 15, no. 5, pp. 669–686, 1994.
- [2] ANSYS, "Ansys academic research mechanical, release 18.1."
- [3] A. Yucesoy, "The role of morphology and residual stress on blast-induced traumatic brain injury," Master's thesis, Michigan State University, 2019.
- [4] R. K. Gupta and A. Przekwas, "Mathematical models of blast-induced thi: current status, challenges, and prospects," *Frontiers in neurology*, vol. 4, p. 59, 2013.
- [5] X. Tan, A. Przekwas, and R. Gupta, "Computational modeling of blast wave interaction with a human body and assessment of traumatic brain injury," *Shock Waves*, vol. 27, no. 6, pp. 889–904, 2017.
- [6] A. Przekwas, H. T. Garimella, X. G. Tan, Z. Chen, Y. Miao, V. Harrand, R. H. Kraft, and R. K. Gupta, "Biomechanics of blast this with time-resolved consecutive primary, secondary, and tertiary loads," *Military medicine*, vol. 184, no. Supplement_1, pp. 195–205, 2019.
- [7] E. Fievisohn, Z. Bailey, A. Guettler, and P. VandeVord, "Primary blast brain injury mechanisms: current knowledge, limitations, and future directions," *Journal of biomechanical engineering*, vol. 140, no. 2, p. 020806, 2018.
- [8] S. Canchi, M. Sarntinoranont, Y. Hong, J. J. Flint, G. Subhash, and M. A. King, "Simulated blast overpressure induces specific astrocyte injury in an ex vivo brain slice model," *PloS one*, vol. 12, no. 4, p. e0175396, 2017.
- [9] H. Fischer, "Us military casualty statistics: operation new dawn, operation iraqi freedom, and operation enduring freedom." Library of Congress Washington Dc Congressional Research service, 2013.
- [10] D. F. Meaney, B. Morrison, and C. D. Bass, "The mechanics of traumatic brain injury: a review of what we know and what we need to know for reducing its societal burden," *Journal of biomechanical engineering*, vol. 136, no. 2, p. 021008, 2014.
- [11] C. R. Bass, M. B. Panzer, K. A. Rafaels, G. Wood, J. Shridharani, and B. Capehart, "Brain injuries from blast," *Annals of biomedical engineering*, vol. 40, no. 1, pp. 185–202, 2012.

- [12] Y. C. Chen, D. H. Smith, and D. F. Meaney, "In-vitro approaches for studying blast-induced traumatic brain injury," *Journal of neurotrauma*, vol. 26, no. 6, pp. 861–876, 2009.
- [13] A. Nakagawa, G. T. Manley, A. D. Gean, K. Ohtani, R. Armonda, A. Tsukamoto, H. Yamamoto, K. Takayama, and T. Tominaga, "Mechanisms of primary blast-induced traumatic brain injury: insights from shock-wave research," *Journal of neurotrauma*, vol. 28, no. 6, pp. 1101–1119, 2011.
- [14] H. L. Lew, "Rehabilitation needs of an increasing population of patients: Traumatic brain injury, polytrauma, and blast-related injuries," *Journal of Rehabilitation Research and Development*, vol. 42, no. 4, p. xiii, 2005.
- [15] S. G. Scott, H. G. Belanger, R. D. Vanderploeg, J. Massengale, and J. Scholten, "Mechanism-of-injury approach to evaluating patients with blast-related polytrauma," *Journal of the American Osteopathic Association*, vol. 106, no. 5, p. 265, 2006.
- [16] J. M. Dewey, "The shape of the blast wave: studies of the friedlander equation," in *Proceeding of the 21st International Symposium on Military Aspects of Blast and Shock (MABS), Israel*, 2010, pp. 1–9.
- [17] N. Chandra, S. Ganpule, N. Kleinschmit, R. Feng, A. Holmberg, A. Sundaramurthy, V. Selvan, and A. Alai, "Evolution of blast wave profiles in simulated air blasts: experiment and computational modeling," *Shock Waves*, vol. 22, no. 5, pp. 403–415, 2012.
- [18] W. C. Moss, M. J. King, and E. G. Blackman, "Skull flexure from blast waves: a mechanism for brain injury with implications for helmet design," *Physical review letters*, vol. 103, no. 10, p. 108702, 2009.
- [19] R. Bolander, B. Mathie, C. Bir, D. Ritzel, and P. VandeVord, "Skull flexure as a contributing factor in the mechanism of injury in the rat when exposed to a shock wave," *Annals of biomedical engineering*, vol. 39, no. 10, p. 2550, 2011.
- [20] E. H. Clayton, G. M. Genin, and P. V. Bayly, "Transmission, attenuation and reflection of shear waves in the human brain," *Journal of The Royal Society Interface*, vol. 9, no. 76, pp. 2899–2910, 2012.
- [21] G. Nusholtz, P. Kaiker, and W. Gould, "Two factors critical in the pressure response of the impacted head." *Aviation, space, and environmental medicine*, vol. 58, no. 12, pp. 1157–1164, 1987.
- [22] J.-P. Franc and J.-M. Michel, Fundamentals of cavitation. Springer science & Business media, 2006, vol. 76.

- [23] C. E. Brennen, Cavitation and Bubble Dynamics. Cambridge University Press, 2013.
- [24] J. R. Blake and D. Gibson, "Cavitation bubbles near boundaries," *Annual review of fluid mechanics*, vol. 19, no. 1, pp. 99–123, 1987.
- [25] S. Canchi, K. Kelly, Y. Hong, M. A. King, G. Subhash, and M. Sarntinoranont, "Controlled single bubble cavitation collapse results in jet-induced injury in brain tissue," *Journal of the mechanical behavior of biomedical materials*, vol. 74, pp. 261–273, 2017.
- [26] Y. Hong, M. Sarntinoranont, G. Subhash, S. Canchi, and M. King, "Localized tissue surrogate deformation due to controlled single bubble cavitation," *Experimental Mechanics*, vol. 56, no. 1, pp. 97–109, 2016.
- [27] E.-A. Brujan, K. Nahen, P. Schmidt, and A. Vogel, "Dynamics of laser-induced cavitation bubbles near an elastic boundary," *Journal of Fluid Mechanics*, vol. 433, no. 1, pp. 251–281, 2001.
- [28] K. H. Taber, D. L. Warden, and R. A. Hurley, "Blast-related traumatic brain injury: what is known?" *The Journal of neuropsychiatry and clinical neurosciences*, vol. 18, no. 2, pp. 141–145, 2006.
- [29] P. A. Taylor, J. S. Ludwigsen, and C. C. Ford, "Investigation of blast-induced traumatic brain injury," *Brain injury*, vol. 28, no. 7, pp. 879–895, 2014.
- [30] M. Bustamante, D. Singh, and D. Cronin, "Polymeric hopkinson bar-confinement chamber apparatus to evaluate fluid cavitation," *Experimental Mechanics*, vol. 58, no. 1, pp. 55–74, 2018.
- [31] M. A. G. Sosa, R. De Gasperi, A. J. Paulino, P. E. Pricop, M. C. Shaughness, E. Maudlin-Jeronimo, A. A. Hall, W. G. Janssen, F. J. Yuk, N. P. Dorr *et al.*, "Blast overpressure induces shear-related injuries in the brain of rats exposed to a mild traumatic brain injury," *Acta neuropathologica communications*, vol. 1, no. 1, p. 51, 2013.
- [32] M. Sarntinoranont, S. J. Lee, Y. Hong, M. A. King, G. Subhash, J. Kwon, and D. F. Moore, "High-strain-rate brain injury model using submerged acute rat brain tissue slices," *Journal of neurotrauma*, vol. 29, no. 2, pp. 418–429, 2012.
- [33] J. V. Rosenfeld, A. C. McFarlane, P. Bragge, R. A. Armonda, J. B. Grimes, and G. S. Ling, "Blast-related traumatic brain injury," *The Lancet Neurology*, vol. 12, no. 9, pp. 882–893, 2013.
- [34] W. W. Chen and B. Song, Split Hopkinson (Kolsky) bar: design, testing and applications. Springer Science & Business Media, 2010.

- [35] M. Nienaber, J. S. Lee, R. Feng, and J. Y. Lim, "Impulsive pressurization of neuronal cells for traumatic brain injury study," *JoVE (Journal of Visualized Experiments)*, no. 56, p. e2723, 2011.
- [36] J. Goeller, A. Wardlaw, D. Treichler, J. O'Bruba, and G. Weiss, "Investigation of cavitation as a possible damage mechanism in blast-induced traumatic brain injury," *Journal of neurotrauma*, vol. 29, no. 10, pp. 1970–1981, 2012.
- [37] R. S. Salzar, D. Treichler, A. Wardlaw, G. Weiss, and J. Goeller, "Experimental investigation of cavitation as a possible damage mechanism in blast-induced traumatic brain injury in post-mortem human subject heads," *Journal of neurotrauma*, vol. 34, no. 8, pp. 1589–1602, 2017.
- [38] M. B. Panzer, K. A. Matthews, A. W. Yu, B. Morrison, D. F. Meaney, and C. R. Bass, "A multiscale approach to blast neurotrauma modeling: part i-development of novel test devices for in vivo and in vitro blast injury models," *Frontiers in neurology*, vol. 3, p. 46, 2012.
- [39] G. B. Effgen, C. D. Hue, E. Vogel III, M. B. Panzer, D. F. Meaney, C. Bass, and B. Morrison III, "A multiscale approach to blast neurotrauma modeling: part ii: methodology for inducing blast injury to in vitro models," *Frontiers in neurology*, vol. 3, p. 23, 2012.
- [40] C. E. Needham, D. Ritzel, G. T. Rule, S. Wiri, and L. Young, "Blast testing issues and thi: experimental models that lead to wrong conclusions," *Frontiers in neurology*, vol. 6, p. 72, 2015.
- [41] N. J. Logan, H. Arora, and C. A. Higgins, "Evaluating primary blast effects in vitro," JoVE (Journal of Visualized Experiments), no. 127, p. e55618, 2017.
- [42] R. Campos-Pires, A. Yonis, W. Macdonald, K. Harris, C. J. Edge, P. F. Mahoney, and R. Dickinson, "A novel in vitro model of blast traumatic brain injury," *JoVE (Journal of Visualized Experiments)*, no. 142, p. e58400, 2018.
- [43] R. A. Bauman, G. Ling, L. Tong, A. Januszkiewicz, D. Agoston, N. Delanerolle, Y. Kim, D. Ritzel, R. Bell, J. Ecklund *et al.*, "An introductory characterization of a combat-casualty-care relevant swine model of closed head injury resulting from exposure to explosive blast," *Journal of neurotrauma*, vol. 26, no. 6, pp. 841–860, 2009.
- [44] M. D. Alley, B. R. Schimizze, and S. F. Son, "Experimental modeling of explosive blast-related traumatic brain injuries," *Neuroimage*, vol. 54, pp. S45–S54, 2011.
- [45] N. C. De Lanerolle, F. Bandak, D. Kang, A. Y. Li, F. Du, P. Swauger, S. Parks, G. Ling, and J. H. Kim, "Characteristics of an explosive blast-induced brain injury in an experimental model," *Journal of Neuropathology & Experimental Neurology*, vol. 70, no. 11, pp. 1046–1057, 2011.

- [46] M. Risling, S. Plantman, M. Angeria, E. Rostami, B.-M. Bellander, M. Kirkegaard, U. Arborelius, and J. Davidsson, "Mechanisms of blast induced brain injuries, experimental studies in rats," *Neuroimage*, vol. 54, pp. S89–S97, 2011.
- [47] A. Nakagawa, M. Fujimura, K. Kato, H. Okuyama, T. Hashimoto, K. Takayama, and T. Tominaga, "Shock wave-induced brain injury in rat: novel traumatic brain injury animal model," in *Acta Neurochirurgica Supplements*. Springer, 2008, pp. 421–424.
- [48] N. E. Zander, T. Piehler, R. Banton, and R. Benjamin, "Bioeffects on an in vitro model by small-scale explosives and shock wave overpressure impacts," US Army Research Laboratory Aberdeen Proving Ground United States, Tech. Rep., 2017.
- [49] M. Bustamante and D. Cronin, "Cavitation threshold evaluation of porcine cerebrospinal fluid using a polymeric split hopkinson pressure bar-confinement chamber apparatus," *Journal of the mechanical behavior of biomedical materials*, vol. 100, p. 103400, 2019.
- [50] Y. Hong, S. Canchi, M. King, S. J. Lee, M. Sarntinoranont, and G. Subhash, "Development of a test system to study brain tissue damage due to cavitation," *Am. Soc. Biomech. Gainesville, Florida*, vol. 2, 2012.
- [51] W. Kang, Y. Chen, A. Bagchi, and T. J. OShaughnessy, "Characterization and detection of acceleration-induced cavitation in soft materials using a drop-tower-based integrated system," *Review of Scientific Instruments*, vol. 88, no. 12, p. 125113, 2017.
- [52] W. Kang and M. Raphael, "Acceleration-induced pressure gradients and cavitation in soft biomaterials," *Scientific reports*, vol. 8, no. 1, pp. 1–12, 2018.
- [53] J. Wu and W. L. Nyborg, "Ultrasound, cavitation bubbles and their interaction with cells," *Advanced drug delivery reviews*, vol. 60, no. 10, pp. 1103–1116, 2008.
- [54] W. Zhu, M. Alkhazal, M. Cho, and S. Xiao, "Microbubble generation by piezotrans-ducer for biological studies," *Review of Scientific Instruments*, vol. 86, no. 12, p. 124901, 2015.
- [55] J. B. Estrada, C. Barajas, D. L. Henann, E. Johnsen, and C. Franck, "High strain-rate soft material characterization via inertial cavitation," *Journal of the Mechanics and Physics of Solids*, vol. 112, pp. 291–317, 2018.
- [56] B. Gerold, S. Kotopoulis, C. McDougall, D. McGloin, M. Postema, and P. Prentice, "Laser-nucleated acoustic cavitation in focused ultrasound," *Review of Scientific Instruments*, vol. 82, no. 4, p. 044902, 2011.

- [57] K. Upadhyay, A. Bhattacharyya, G. Subhash, and D. Spearot, "Quasi-static and high strain rate simple shear characterization of soft polymers," *Experimental Mechanics*, pp. 1–15, 2019.
- [58] M. Trexler, A. Lennon, A. Wickwire, T. Harrigan, Q. Luong, J. Graham, A. Maisano, J. Roberts, and A. Merkle, "Verification and implementation of a modified split hop-kinson pressure bar technique for characterizing biological tissue and soft biosimulant materials under dynamic shear loading," Journal of the mechanical behavior of biomedical materials, vol. 4, no. 8, pp. 1920–1928, 2011.
- [59] T. Mezger, The rheology handbook: for users of rotational and oscillatory rheometers. European Coatings, 2020.
- [60] K. B. Arbogast, K. L. Thibault, B. S. Pinheiro, K. I. Winey, and S. S. Margulies, "A high-frequency shear device for testing soft biological tissues," *Journal of biomechanics*, vol. 30, no. 7, pp. 757–759, 1997.
- [61] R. J. Okamoto, E. H. Clayton, and P. V. Bayly, "Viscoelastic properties of soft gels: comparison of magnetic resonance elastography and dynamic shear testing in the shear wave regime," *Physics in Medicine & Biology*, vol. 56, no. 19, p. 6379, 2011.
- [62] B. Rashid, M. Destrade, and M. D. Gilchrist, "Mechanical characterization of brain tissue in simple shear at dynamic strain rates," *Journal of the mechanical behavior of biomedical materials*, vol. 28, pp. 71–85, 2013.
- [63] M. C. LaPlaca, D. K. Cullen, J. J. McLoughlin, and R. S. Cargill II, "High rate shear strain of three-dimensional neural cell cultures: a new in vitro traumatic brain injury model," *Journal of biomechanics*, vol. 38, no. 5, pp. 1093–1105, 2005.
- [64] F. Perez Jr and M. Al-Haik, "Analysis of elastic stress wave propagation through a complex composite structure," *International Journal of Theoretical and Applied Multiscale Mechanics*, vol. 1, no. 2, pp. 164–175, 2009.
- [65] T. Rahimzadeh, E. M. Arruda, and M. Thouless, "Design of armor for protection against blast and impact," *Journal of the Mechanics and Physics of Solids*, vol. 85, pp. 98–111, 2015.
- [66] C. Morganti-Kossmann, R. Raghupathi, and A. Maas, *Traumatic brain and spinal cord injury: challenges and developments*. Cambridge University Press, 2012.
- [67] M. Ghajari, P. J. Hellyer, and D. J. Sharp, "Computational modelling of traumatic brain injury predicts the location of chronic traumatic encephalopathy pathology," *Brain*, vol. 140, no. 2, pp. 333–343, 2017.

- [68] A. Jean, M. K. Nyein, J. Q. Zheng, D. F. Moore, J. D. Joannopoulos, and R. Radovitzky, "An animal-to-human scaling law for blast-induced traumatic brain injury risk assessment," *Proceedings of the National Academy of Sciences*, vol. 111, no. 43, pp. 15310–15315, 2014.
- [69] S. T. Ahlers, E. Vasserman-Stokes, M. C. Shaughness, A. A. Hall, D. A. Shear, M. Chavko, R. M. McCarron, and J. R. Stone, "Assessment of the effects of acute and repeated exposure to blast overpressure in rodents: toward a greater understanding of blast and the potential ramifications for injury in humans exposed to blast," Frontiers in neurology, vol. 3, p. 32, 2012.
- [70] M. Chavko, T. Watanabe, S. Adeeb, J. Lankasky, S. T. Ahlers, and R. M. McCarron, "Relationship between orientation to a blast and pressure wave propagation inside the rat brain," *Journal of neuroscience methods*, vol. 195, no. 1, pp. 61–66, 2011.
- [71] I. Cernak, "Blast-induced neurotrauma models and their requirements," Frontiers in neurology, vol. 5, p. 128, 2014.
- [72] B. Song and W. Chen, "Split hopkinson pressure bar techniques for characterizing soft materials," *Latin American Journal of Solids and Structures*, vol. 2, no. 2, pp. 113–152, 2005.
- [73] C. Bacon, "An experimental method for considering dispersion and attenuation in a viscoelastic hopkinson bar," *Experimental mechanics*, vol. 38, no. 4, pp. 242–249, 1998.
- [74] W. Chen, B. Zhang, and M. Forrestal, "A split hopkinson bar technique for low-impedance materials," *Experimental mechanics*, vol. 39, no. 2, pp. 81–85, 1999.
- [75] O. S. Lee, S. S. You, J. H. Chong, and H. S. Kang, "Dynamic deformation under a modified split hopkinson pressure bar experiment," *KSME International Journal*, vol. 12, no. 6, pp. 1143–1149, 1998.
- [76] Q. Liu and G. Subhash, "Characterization of viscoelastic properties of polymer bar using iterative deconvolution in the time domain," *Mechanics of Materials*, vol. 38, no. 12, pp. 1105–1117, 2006.
- [77] A. S. Wineman and K. R. Rajagopal, Mechanical response of polymers: an introduction. Cambridge university press, 2000.
- [78] H. Kolsky, *Stress Waves in Solids*, ser. Dover Books on Physics. Dover Publications, 1963.
- [79] K. F. Graff, Wave Motion in Elastic Solids, ser. Dover Books on Physics Series. Dover Publications, 1991.

- [80] M. A. Meyers, *Dynamic Behavior of Materials*, ser. Wiley-Interscience publication. Wiley, 1994.
- [81] A. Bedford and D. Drumheller, *Introduction to elastic wave propagation*. John Wiley & Sons Australia, Limited, 1994.
- [82] P. Williams, P. Williams, and S. Brown, "Cavitation phenomena in water involving the reflection of ultrasound pulses from a free surface, or from flexible membranes," *Physics in Medicine & Biology*, vol. 43, no. 10, p. 3101, 1998.
- [83] Engineering Toolbox, "Bulk Modulus and Fluid Elasticity," https://www.engineeringtoolbox.com/.
- [84] K. Deb, Multi-objective optimization using evolutionary algorithms. John Wiley & Sons, 2001, vol. 16.
- [85] K. Deb, A. Pratap, S. Agarwal, and T. Meyarivan, "A fast and elitist multiobjective genetic algorithm: Nsga-ii," *IEEE transactions on evolutionary computation*, vol. 6, no. 2, pp. 182–197, 2002.
- [86] K. Kido, Digital Fourier Analysis: Fundamentals. Springer, 2015.
- [87] Y. Hong, M. Sarntinoranont, G. Subhash, S. Canchi, and M. King, "Localized tissue surrogate deformation due to controlled single bubble cavitation," *Experimental Mechanics*, vol. 56, no. 1, pp. 97–109, 2016.
- [88] M. H. Sadd, Elasticity: theory, applications, and numerics. Academic Press, 2009.
- [89] H. K. Khalil, "Nonlinear systems," Upper Saddle River, 2002.
- [90] P. J. Antsaklis and A. N. Michel, *Linear systems*. Springer Science & Business Media, 2006.
- [91] R. Kfoury, B. Marzban, E. Makki, M. L. Greenfield, and H. Yuan, "Effect of pressure profile of shock waves on lipid membrane deformation," *PloS one*, vol. 14, no. 2, p. e0212566, 2019.
- [92] B. Koo, B. Choi, H. Park, and K.-J. Yoon, "Past, Present, and Future of Brain Organoid Technology," *Molecules and cells*, vol. 42, no. 9, p. 617, 2019.
- [93] D. Stålhammar, "Experimental brain damage from fluid pressures due to impact acceleration. 1. design of experimental procedure," *Acta Neurologica Scandinavica*, vol. 52, no. 1, pp. 7–26, 1975.

- [94] J. J. Crisco, B. J. Wilcox, J. T. Machan, T. W. McAllister, A.-C. Duhaime, S. M. Duma, S. Rowson, J. G. Beckwith, J. J. Chu, and R. M. Greenwald, "Magnitude of head impact exposures in individual collegiate football players," *Journal of applied biomechanics*, vol. 28, no. 2, pp. 174–183, 2012.
- [95] A. Visioli, Practical PID control. Springer Science & Business Media, 2006.
- [96] D. R. Lide, CRC handbook of chemistry and physics. CRC press, 2004, vol. 85.
- [97] X. Feng, Z. Duan, Y. Fu, A. Sun, and D. Zhang, "The technology and application of voice coil actuator," in 2011 Second International Conference on Mechanic Automation and Control Engineering. IEEE, 2011, pp. 892–895.
- [98] R. Cao, Z. Huang, T. Varghese, and G. Nabi, "Tissue mimicking materials for the detection of prostate cancer using shear wave elastography: A validation study," *Medical physics*, vol. 40, no. 2, 2013.
- [99] M.-K. Sun, J. Shieh, C.-W. Lo, C.-S. Chen, B.-T. Chen, C.-W. Huang, and W.-S. Chen, "Reusable tissue-mimicking hydrogel phantoms for focused ultrasound ablation," *Ultrasonics sonochemistry*, vol. 23, pp. 399–405, 2015.
- [100] J. Kerwin, S. Vidhate, F. Masoomi, M. Tartis, A. M. Willis, and R. Mejia-Alvarez, "Experimental study of the mechanics of blast-induced traumatic brain injury," in *Mechanics of Biological Systems & Micro-and Nanomechanics, Volume 4.* Springer, 2019, pp. 71–74.
- [101] A. Wermer, J. Kerwin, K. Welsh, R. Mejia-Alvarez, M. Tartis, and A. Willis, "Materials characterization of cranial simulants for blast-induced traumatic brain injury," *Military medicine*, vol. 185, no. Supplement_1, pp. 205–213, 2020.
- [102] L. Adrian, R. J. Adrian, and J. Westerweel, *Particle image velocimetry*. Cambridge University Press, 2011, no. 30.
- [103] R. Gonzalez and R. Woods, Digital Image Processing. Pearson, 2018.
- [104] W. Thielicke and E. J. Stamhuis, "PIVlab towards user-friendly, affordable and accurate digital particle image velocimetry in MATLAB," *Journal of Open Research Software*, vol. 2, oct 2014.
- [105] J. D. Ferry, Viscoelastic properties of polymers. John Wiley & Sons, 1980.
- [106] E. S. Lein, M. J. Hawrylycz, N. Ao, M. Ayres, A. Bensinger, A. Bernard, A. F. Boe, M. S. Boguski, K. S. Brockway, E. J. Byrnes *et al.*, "Genome-wide atlas of gene expression in the adult mouse brain," *Nature*, vol. 445, no. 7124, pp. 168–176, 2007.

- [107] P. A. Taylor and C. C. Ford, "Simulation of blast-induced early-time intracranial wave physics leading to traumatic brain injury," *Journal of biomechanical engineering*, vol. 131, no. 6, 2009.
- [108] S.-H. Lee, G. Govindaiah, and C. L. Cox, "Heterogeneity of firing properties among rat thalamic reticular nucleus neurons," *The Journal of physiology*, vol. 582, no. 1, pp. 195–208, 2007.
- [109] J. A. Beatty, E. L. Sylwestrak, and C. L. Cox, "Two distinct populations of projection neurons in the rat lateral parafascicular thalamic nucleus and their cholinergic responsiveness," *Neuroscience*, vol. 162, no. 1, pp. 155–173, 2009.
- [110] T. Delgado, P. A. Carroll, A. S. Punjabi, D. Margineantu, D. M. Hockenbery, and M. Lagunoff, "Induction of the warburg effect by kaposi's sarcoma herpesvirus is required for the maintenance of latently infected endothelial cells," *Proceedings of the* National Academy of Sciences, vol. 107, no. 23, pp. 10696–10701, 2010.
- [111] F. Birey, J. Andersen, C. D. Makinson, S. Islam, W. Wei, N. Huber, H. C. Fan, K. R. C. Metzler, G. Panagiotakos, N. Thom et al., "Assembly of functionally integrated human forebrain spheroids," *Nature*, vol. 545, no. 7652, pp. 54–59, 2017.
- [112] C. A. Trujillo, R. Gao, P. D. Negraes, J. Gu, J. Buchanan, S. Preissl, A. Wang, W. Wu, G. G. Haddad, I. A. Chaim *et al.*, "Complex oscillatory waves emerging from cortical organoids model early human brain network development," *Cell stem cell*, vol. 25, no. 4, pp. 558–569, 2019.
- [113] S. P. Paca, "The rise of three-dimensional human brain cultures," *Nature*, vol. 553, no. 7689, pp. 437–445, 2018.